Experimental studies and asymptotic scaling for the development of engineering tools to predict coupled heat transfer and plastic deformation in Friction Stir Welding (FSW)

by

Jordan Tsui

A thesis submitted in partial fulfillment of the requirements for the degree of

Master of Science

in

Materials Engineering

Department of Chemical and Materials Engineering

University of Alberta

Abstract

A study of temperature, force, and torque was performed using a set of ten different friction stir welding (FSW) tools. It was observed that pin diameter had the most significant effect on steady state welding temperature followed by shoulder diameter having a smaller but measureable effect. Pin threading caused the smallest change, increasing welding temperature only a few degrees higher than a smooth surface pin. Comparisons between temperatures measured from the FSW tool and the base material showed that material deformation during welding often causes thermocouple position in the substrate to move which can result in inaccurate readings. Additionally, thermocouples located in the substrate failed to fully capture temperature changes caused by increases in the tool shoulder diameter.

Forces measured along the x, y, and z axis were all directly related to the size of the pin and shoulder diameter with the pin having a greater influence. As pin or shoulder diameter were increased, forces along the three axes increased and vice versa. However, once pin diameter became large enough the addition of pin threading caused measured force to decrease due to increased welding temperature which softened the base material. Torque was also directly related to the size of the pin and shoulder diameter (i.e. as pin/shoulder diameter increased, measured torque increased). The one exception was for tools with small pin diameter which experienced high torque due to their inability to generate enough frictional heating which led to low welding temperature.

Experimental results of welding temperature and torque were compared to an existing model of coupled heat transfer and plastic deformation. Analyzing a single material with the model yielded the best results, and the accuracy of theoretical welding temperature and torque for aluminum alloy 5059 was 94% and 85%, respectively. Accounting for the size of the tool shoulder in a correction function for the model improved predicted values of temperature and torque by 5% over previous results that did not account for shoulder diameter.

Preface

The materials presented in the current thesis are part of the research project under supervision of Dr. Patricio Mendez and Dr. Adrian Gerlich, which has been funded by AUTO21 and the Natural Sciences and Engineering Research Council (NSERC) of Canada.

Dr. Patricio Mendez and Dr. Adrian Gerlich provided the advice for conducting all the experimental setups, supervised the data collection, analysis and interpretation.

To Yvonne and my family, for their love, encouragement and continuous support.

Acknowledgements

I would like to thank my adviser, Dr. Patricio Mendez, for his support, patience, and encouragement starting from undergraduate to the end of my MSc studies. His guidance and advice have helped me overcome many hurdles and to develop into a better engineer. I am very thankful to have been able to work alongside him.

I would also like to acknowledge and thank my co-advisor, Dr. Adrian Gerlich, for his continued assistance all the way from Waterloo.

Dr. Leijun Li, Dr. Barry Wiskel, and Dr. Arvind Rajendran for being members of my thesis committee.

I would extend my gratitude to my friends and colleagues at the Canadian Centre for Welding and Joining (CCWJ) for their support and help. A special thanks to Dr. Hossein Izadi, (future Dr.) Gentry Wood, (future Dr.) Nairn Barnes, Dr. Goetz Dapp, and Dr. Ata Kamyabi for their help and advice.

My research has been made possible thanks to the support of AUTO21 and the Natural Sciences and Engineering Research Council of Canada.

Finally, I would like to express my gratitude to Yvonne and my parents for their endless love and always being there for me.

Contents

List of Tables

x

List of Figures

Chapter 1

Introduction

Friction stir welding (FSW) is a solid-state joining process invented at The Welding Institute (TWI) in 1991 (Thomas et al., 1991). It was initially designed for use with aluminum alloys, but has since been extended to be used on magnesium alloys, mild steel, stainless steel, and titanium alloy (TWI The Welding Institute). Some examples of how FSW has been applied can be seen in NASA's space shuttle external tanks, super liners such as the Ogasawara, Shinkansen bullet trains, and Ford's magnesium prototype spare wheel.

Friction stir welding is classified as solid-state because the base plate material does not exceed its melting point throughout the process. Friction stir welding uses a non-consumable tool composed of a pin and shoulder. The tool's purpose is to generate sufficient heat such that the base material will soften. Heat is generated through means of friction, pressure, and localized plastic deformation of the substrate. As the tool travels through the softened base plate it will also serve to mix the material near the pin and shoulder to create a joint. A common configuration of FSW is a butt weld where the FSW tool is inserted in between the edges of two sheets and traverses along the joint Figure 1.1.

Mishra and Ma (Mishra and Ma, 2005) have summarized FSW as an environmentally green process due to its energy efficiency. Friction stir welding uses significantly less
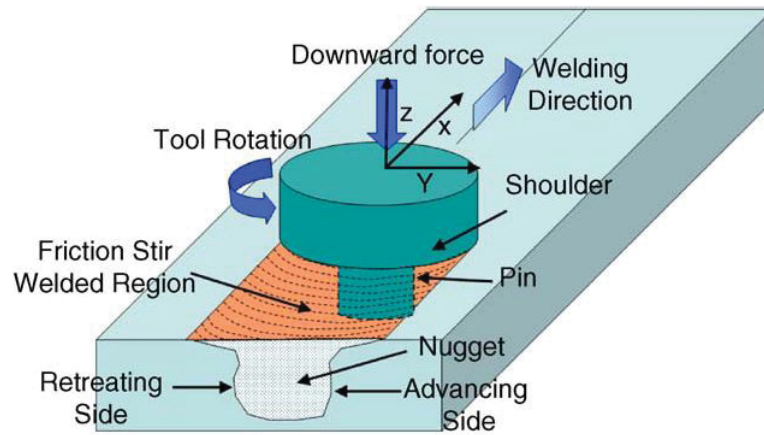
Figure 1.1: Schematic diagram of friction stir welding (Mishra and Ma, 2005)

energy than traditional arc welding processes, requires no filler metal, and does not need shielding gas. Its versatility is demonstrated in the ability to join dissimilar aluminum alloys, magnesium to aluminum (Mohammadi et al., 2015; Zhao et al., 2015), copper to aluminum (Mehta and Badheka, 2015), and steel to aluminum (Liu et al., 2014). Some other advantages of friction stir welding include fine microstructure, absence of cracking, low distortion of workpiece, and no loss of alloying elements (Mishra and Ma, 2005).

Chapter 2

Background

2.1 Friction stir welding models

Friction stir welding (FSW) has been modeled using numerical and analytical models. The main objective of both methods is to produce a simple, practical way to understand and predict phenomenon observed during friction stir welding. The key aspects to these models has been how the tool contributes to heat generation through friction and plastic deformation, heat transfer, and contact conditions between the tool and the substrate. Models analyzing temperature field also try to consider whether the location of greatest heat generation occurs at the tool shoulder, the tool pin, or a combination of both.

The contact conditions of friction stir welding relate to heat generation and can be broken down into two conditions: sticking and sliding. The sticking condition states that material will adhere to the moving tool, due to the contact shear stress being greater than the yield shear stress of the material. For the sliding condition, the contact shear stress is less than the yield shear stress of the material, and the substrate material will only be elastically deformed as the tool moves through it (Schmidt et al., 2004). The sticking condition implies heat generation through plastic deformation, whereas a sliding condition will produce heat through frictional mechanisms. Seidel and Reynolds,

Ulysse, Colegrove and Shercliff, and Dong et al. (Seidel and Reynolds, 2003; Ulysse, 2002; Colegrove and Shercliff, 2004a; Dong et al., 2001) developed models only considering a sticking condition. Models attributing heat generation to plastic deformation have been developed by Frigaard et al. (Frigaard et al., 2001) and Nandan et al. (Nandan et al., 2007). Work performed by Schmidt et al. found that a sticking condition was dominant by using tracers to study material flow (Schmidt et al., 2004). Chao et al., McClure et al., and Xu et al. (Chao et al., 2003; McClure et al., 1998; Xu et al., 2001) developed models assuming a sliding condition. A stick-slip model factoring in a combination of both conditions has been developed by Buck and Langerman, Schmidt and Hattel, and Schneider et al. (Buck and Langerman, 2004; Schmidt and Hattel, 2005b; Schneider et al., 2006).

Utilizing Finite Element Methods (FEM), Khandkar et al. (Khandkar et al., 2003) derived an uncoupled thermal model where temperature was correlated with machine power input. Zhu and Chao (Zhu and Chao, 2004) used FEM to develop an uncouple model where transient temperature is used for thermomechanical simulation. Chen and Kovacevic (Chen and Kovacevic, 2003) have also used FEM to develop a 3D model incorporating mechanical reaction of the tool and the thermomechanical process of the substrate. Uncoupled thermal and thermomechanical models have also been worked on by Colegrove and Shercliff (Colegrove and Shercliff, 2004b), Siedel and Reynolds (Seidel and Reynolds, 2003), and Heurtier et al (Heurtier et al., 2006).

Studies looking at the temperature fields of FSW often model the tool as a point heat source based on Rosenthal's equations (Rosenthal, 1946). McClure et al. (McClure et al., 1998), and Shercliff et al. (Shercliff and Colegrove, 2002) based their models on a moving line heat source. Temperature models often propose different assumption, whether the

heat generation is dominated by the shoulder (McClure et al., 1998; Chao et al., 2003) or involves a combination of the shoulder and pin (Schmidt et al., 2004; Khandkar et al., 2003; Chen and Kovacevic, 2003; Schmidt and Hattel, 2005b). Schmidt et al. (Schmidt et al., 2004) worked on models of heat transfer by conduction and found that the shoulder is the main contributor to heat generation. Chao et al. (Chao et al., 2003) also focused on heat transfer by conduction and observed that 5% of the heat generated was lost back into the tool. Fully coupled numerical models which predict temperature and shear rates have been proposed by Khandkar et al. (Khandkar et al., 2003), Ulysse (Ulysse, 2002), Colegrove and Shercliff (Colegrove and Shercliff, 2004a,b), Dong et al. (Dong et al., 2001), Nandan et al. (Nandan et al., 2006a,b, 2007), and Cho et al. (Cho et al., 2005).

Scaling analysis of FSW has been used to develop prediction models as well. Scaling analysis is described as a systematic method for nondimensionalizing independent and dependent variables, and their derivatives, in a set of governing equations for describing a physical problem (Krantz, 2007). Dong et al. (Dong et al., 2001) determined that rotational velocity must be proportional to the translation velocity to achieve good weld quality in FSW. Colegrove and Shercliff (Colegrove and Shercliff, 2003) used scaling analysis to show that power is proportional to the tool surface area and travel speed. Reynolds et al. (Reynolds et al., 2005) developed a scaling law relating to weld pitch. Roy et al. (Roy et al., 2006) were able to come up with equations to estimate the peak temperature for friction stir welding. Buck and Langerman (Buck and Langerman, 2004) were able to characterize flow around the tool using asymptotic analysis. Mendez, Tello, and Lienert (Mendez et al., 2010) developed a coupled heat transfer and plastic deformation model which provides expressions to predict maximum temperature, torque, and shear layer thickness.

2.2 Coupled model for friction stir welding

The scaling laws developed by Mendez et al. (Mendez et al., 2010) used an approach based on the Order of Magnitude Scaling technique (Mendez, 2006). The system of equations used for analysis follow four simplifications which are later used to calibrate the final scaling laws. The simplifications are as follows:

1. The travelling pin can be considered a steady state, slow moving heat source. The slow moving heat source condition can be described as a function of the Peclet number given by:

$$\text{Pe} = \frac{Va}{2\alpha} \ll 1 \qquad (2.1)$$

   where V is the pin advance velocity, a is the pin radius, and α is the thermal diffusivity of the base plate material at a critical temperature T_o which will be defined later.

2. There is small advance per revolution. The amount of incoming mass ($\approx Va$) is much smaller than the amount of mass moved in the shear layer ($\approx \omega a \delta$) and can be described with the following expression:

$$Va \ll \omega a \delta \qquad (2.2)$$

   where ω is the angular velocity of rotation of the pin and δ is the thickness of the shear layer.

3. The shear layer is thin and can be expressed as:

$$\delta \ll a \qquad (2.3)$$

4. The thickness of the shear layer is larger than the difference in radius between the shoulder and the pin. This condition can be expressed as:

$$b - a \ll \delta \tag{2.4}$$

where b is the shoulder radius.

The results of scaling analysis provide the following estimations for shear layer thickness $(\widehat{\delta})$, temperature difference within the shear layer $(\widehat{\Delta T_s})$, and torque of the FSW tool pin $(\widehat{M})$. A table of the variables and their meaning are in Table 2.1.

$$\widehat{\delta} = a \left[\frac{8}{3} \frac{\Delta T_m}{\eta_s AB} \left(\frac{\tau_R a^2}{k_o} \right)^n \left(\frac{\eta K_o \omega}{\Delta T_o} \right)^{n+1} \right]^{\frac{1}{2}} \tag{2.5}$$

$$\widehat{T_s} = \Delta T_m \left[\frac{3}{2} \frac{\eta_s}{AB\Delta T_m} \left(\frac{\eta K_o}{\Delta T_o} \right)^{n-1} \left(\frac{a^2 \tau_R}{k_o} \right)^n \omega^{n+1} \right]^{\frac{1}{2}} + T_o \tag{2.6}$$

$$\widehat{M} = 2\pi \widehat{\tau_c} a^2 t \tag{2.7}$$

$$\tau_R = \frac{\sigma_R}{\sqrt{3}} \tag{2.8}$$

$$\widehat{\tau_c} = \frac{k_o \Delta T_o}{\eta \omega a^2 K_o} \tag{2.9}$$

A correction function was developed by Tello et al. (Tello, 2008) to improve the estimations of $\widehat{\delta}$, $\widehat{\Delta T_s}$, and $\widehat{M}$ by accounting for forces neglected in the formulation of the scaling law (i.e. the four simplifications, Equation 2.1, Equation 2.2, Equation 2.3, and Equation 2.4). The function allows the estimations to become closer to the experimental

Table 2.1: Scaling law variables

ω	rotational speed of the pin (s^{-1})
η	total heat efficiency of the process
η_s	efficiency that accounts for the fraction of the mechanical energy converted into heat
σ_R	normal stress of refrence (Pa)
τ_R	reference shear stress (Pa)
$\widehat{\tau_c}$	estimation of the shear stress within the shear layer (Pa)
a	pin radius (m)
K_o	modified Bessel function of a second kind and order 0
k_o	thermal conductivity of the base plate at T_o(W/m K)
A	constant of the Zener-Hollomom law (s^{-1})
n	constant of the Zener-Hollomom law
B	material constant. $B = exp(-Q/RT_m)$
Q	activation energy (J/mol). Note that this term appears in the constant, B.
R	gas constant (J/mol K). Note that this term appears in the constant, B.
t	thickness of the plate (m)
T_m	melting temperature of the base plate, in this case the solidus temperature (K)
T_o	temperature at the shear layer/base plate interface (K)
ΔT_m	temperature difference $T_m - T_o$ (K)
ΔT_o	temperature difference $T_o - T_\infty$ (K)

measurements and numerical results and is given by Equation 2.10

$$f\left(Pe, \frac{\hat{\delta}}{a}, \frac{V}{\omega\hat{\delta}}, \frac{b-a}{\hat{\delta}}\right) = C_1\left(1+C_2Pe\right)^{C_3}\left(1+C_4\frac{\hat{\delta}}{a}\right)^{C_5}\left(1+C_6\frac{V}{\omega\hat{\delta}}\right)^{C_7}\left(1+C_8\frac{b-a}{\hat{\delta}}\right)^{C_9}$$

(2.10)

where C_i $(i = 1, 2, ..., 9)$ are constants fitted using a minimum least squares regression given by Equation 2.11.

$$\phi = Min \sum_i^n \left(\log\left(\frac{X}{\widehat{X}}\right)_i - \log(f_i)\right)^2$$

(2.11)

where n is the total number of data considered, X is an experimentally measured value, and $\widehat{X}$ is the theoretical estimation of the experimental value. When all the simplification are neglected, C_1 accounts for mathematical errors induced by the scaling model. However, if the simplifications become dominant, the other coefficients rather than C_1 capture a power law behavior. The improved estimations are defined by Equation 2.12.

$$\widehat{X}^+ = \widehat{X} \cdot f\left(Pe, \frac{\hat{\delta}}{a}, \frac{V}{\omega\hat{\delta}}, \frac{b-a}{\hat{\delta}}\right)$$

(2.12)

It was observed by Tello that of the four simplifications the only one affecting temperature, $\widehat{T}_s$, was Equation 2.3. Thus, the improved estimation for shear layer temperature was reduced to Equation 2.13.

$$\widehat{T}_s^+ = \widehat{T}_s \cdot f\left(\frac{\hat{\delta}}{a}\right) = \widehat{T}_s \cdot C_1\left(1+C_2\frac{\hat{\delta}}{a}\right)^{C_3}$$

(2.13)

Tello also found that the estimation of torque, $\widehat{M}$, had no dependence on the four simplifications reducing the correction function to a single coefficient, C_1. The value of C_1 was calculated to be 1.57. The improved estimation of torque is given by Equation 2.14.

$$\widehat{M}^+ = \widehat{M} \cdot 1.57 \tag{2.14}$$

2.3   Temperature and force measurements

Numerous methods for capturing the temperature experimentally during friction stir welding have been proposed. The majority of researchers use thermocouples embedded throughout the substrate at strategic locations to capture the temperature field and maximum welding temperature. For the substrate-thermocouple method, there have been published measurements for aluminum 6061 (Khandkar et al., 2003; Chen and Kovacevic, 2003; Nandan et al., 2006a; Roy et al., 2006; Guerra et al., 2003), aluminum 2024 (Schmidt et al., 2004; Schmidt and Hattel, 2005b; Schmidt et al., 2006; Schneider et al., 2006; Yang et al., 2004; Schmidt and Hattel, 2005a; Fonda and Bingert, 2007), aluminum 7075 (Colegrove and Shercliff, 2003, 2004b), aluminium 7050 (Reynolds et al., 2003, 2005), aluminum 5083 (Colligan, 2007; Chen et al., 2008), mild steel Roy et al. (2006); Nandan et al. (2007), and stainless steel Roy et al. (2006); Zhu and Chao (2004). These measurements are listed in the appendix. Other methods for measuring temperature have been used such as infrared camera (Lienert et al., 2003) and thermoelectric method (De Backer and Bolmsjö, 2013). An alternative to the substrate-thermocouple method has been used where the FSW tool is modified to accept thermocouples instead (Lienert et al., 2003; Gerlich et al., 2005).

Lateral forces have been recorded experimentally using strain gauges (Melendez et al., 2005; Lienert et al., 2003; Milan Vukčević, Sreten Savićević, Mileta Janjić, 2011) and dynometers (Amini and Amiri, 2015; Astarita et al., 2014; Hussein et al., 2015; Trimble et al., 2012). Torque and force have been measured simultaneously using load cells (Balasubramanian et al., 2009; Bahemmat et al., 2015). There have been published values of torque for aluminum 6061 (Khandkar et al., 2003; Lienert et al., 2000), aluminum 2024 (Schmidt et al., 2004; Guerra et al., 2003), aluminum 5083 (Long et al., 2007; Lienert et al., 2000), aluminum 7050 (Long et al., 2007; Reynolds et al., 2003), aluminum 7075 (Lienert et al., 2000), 1018 steel (Lienert et al., 2000), and 304 stainless steel (Zhu and Chao, 2004). These measurements are listed in the appendix.

Chapter 3

Experimental Procedure and Set-up

The following chapter will describe and outline how temperature, force, and torque were measured during friction stir welding. This will cover:

- Friction stir welding tool design

- Temperature measurements and analysis at the tool pin, tool shoulder, and welded substrate

- Force and torque measurements during friction stir welding

- Welding temperature and torque predicted from the coupled model for friction stir welding

3.1 FSW Tool Design

To study the effects of friction stir welding tool geometry on steady state welding temperature a tool matrix was designed with ten separate tools. The ten tools were split into two categories, smooth cylindrical pins and cylindrical threaded pins. Within each category, the tools were grouped such that the effects of pin diameter and shoulder diameter could be isolated and analyzed. The dimensions of the FSW tool are listed in Table 3.1. A

cylindrical shaped pin was chosen because it is the simplest geometry available for FSW tools, and it is the simplification made for the welding temperature prediction model developed by Dr. Mendez (Mendez et al., 2010) for which the experimental results will be compared to.

Table 3.1: Friction stir welding tool dimensions

Tool i.d.	Pin Surface	Pin Length (mm)	Pin Diameter (mm)	Shoulder Diameter (mm)
A	smooth	4	3	9
B	smooth	5.3	4	12
C	smooth	6.7	5	15
D	smooth	5.3	4	9
E	smooth	5.3	4	15
F	threaded	4	3	9
G	threaded	5.3	4	12
H	threaded	6.7	5	15
I	threaded	5.3	4	9
J	threaded	5.3	4	15

Table 3.2: Friction stir welding tool geometry matrix

Pin\Shoulder	9 mm	12 mm	15 mm
3 mm	A, F		
4 mm	D, I	B, G	E, J
5 mm			C, H

The tools can be analyzed by how they are grouped through size and pin surface (Table 3.2). Tools A, B and C (ABC) were grouped such that each consecutive tool increased in overall size. From tools A through C, the pin increased 1 mm in diameter at a time, the shoulder increased by 3 mm at a time, and the pin length increased by 1.35 mm at a time. Multiple welds were performed with each tool, and the temperature and force data was collected. Comparing the results between tools ABC will provided

information on how overall tool size affected steady state welding temperature, forces in the x-y-z directions, and torque experienced by the tool. Tools F, G and H (FGH) are the threaded counterpart to tools ABC. The data collected for tools FGH provided additional information on how pin threading affected welding temperature, force, and torque.

The next tool group is tools D, B, and E (DBE). Tools DBE all share the same pin geometry (5.3 mm pin length and 4 mm pin diameter), but the shoulder diameter changes between each tool. The shoulder diameter from tools D to B to E increased by 3 mm each time. Multiple welds were performed with each tool, and temperature and force data was collected. Since tools DBE share the same pin size, comparing the results between the tools will gave direct information on how the shoulder diameter affected steady state welding temperature and torque experienced by the tool. Tools I, G, and J (IGJ) are the threaded versions of tools DBE. The data collected from tools IGJ gave additional information on how pin threading affected welding temperature, force, and torque.

All ten FSW tools were machined to allow k-type thermocouples to be fed through the side to reach the surface of the pin and shoulder. This was done to be able to take temperature measurements directly at the interface where the FSW tool (pin and shoulder) contacted the welded substrate. Two holes were drilled into each tool, one for the pin and one for the shoulder. A drawing of tool G showing where each hole was drilled is shown in Figure 3.1. The rest of the engineering drawings are listed in the appendix (section 6).
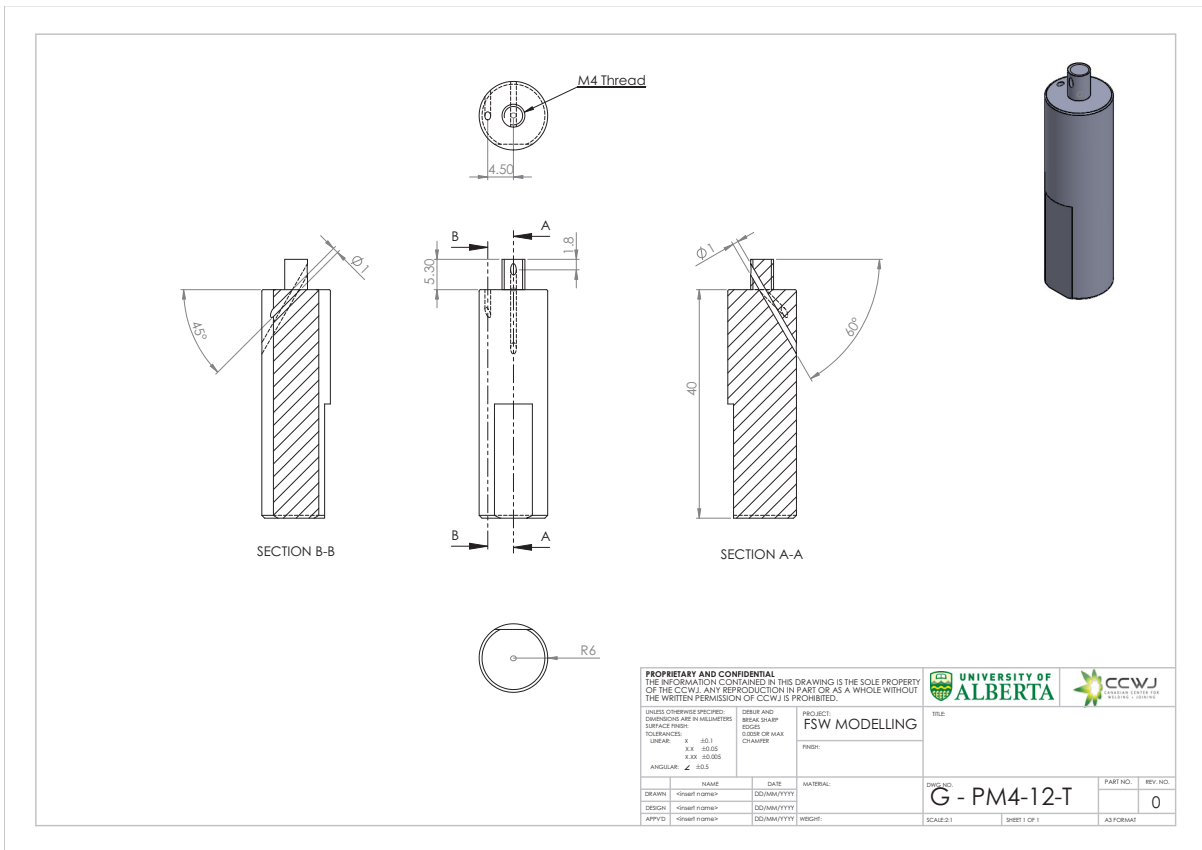
Figure 3.1: Tool G engineering drawing

3.2 Temperature measurements during friction stir welding

3.2.1 FSW pin and shoulder measurements

All experiments were performed using an INDUMA milling machine (model #756012) which was converted into a friction stir welder by tilting the spindle 3° to accommodate for tool tilt, and adding an adapter to hold FSW tools. To measure and record the temperatures at the surfaces of the FSW tool pin and shoulder an MSR 145B data acquisition (DAQ) system was used. The FSW tools designed for experiments had two holed drilled through them leading from the side of the tool to the surface of the pin and shoulder. Two K-type thermocouples (model #5TC-GG-K-36-36) were inserted into these holes with the exposed thermocouple junction at the pin and shoulder surface, and held in place using OMEGABOND 600 cement (Figure 3.2). The OMEGABOND cement was also used to fill in small gaps between the hose clamps to protect the thermocouple wire from aluminum flashing during welding. The MSR 145B data acquisition system and excess thermocouple wire were secured to the INDUMA spindle using hose clamps and zip ties (Figure 3.3).

Welding parameters were chosen such that they could be held constant for all experiments for all of the different FSW tool geometries. This was done to minimize variables so that the effects of tool geometry could be studied more easily. The welding parameters also had to take into accommodation the structural integrity of the tools after drilling holes through them for the thermocouples so that they would not break during welding. The chosen welding parameters were a rotation speed of 1225 RPM and a travel speed of 15 mm/min. The only exception where welding parameters were changed was for tools
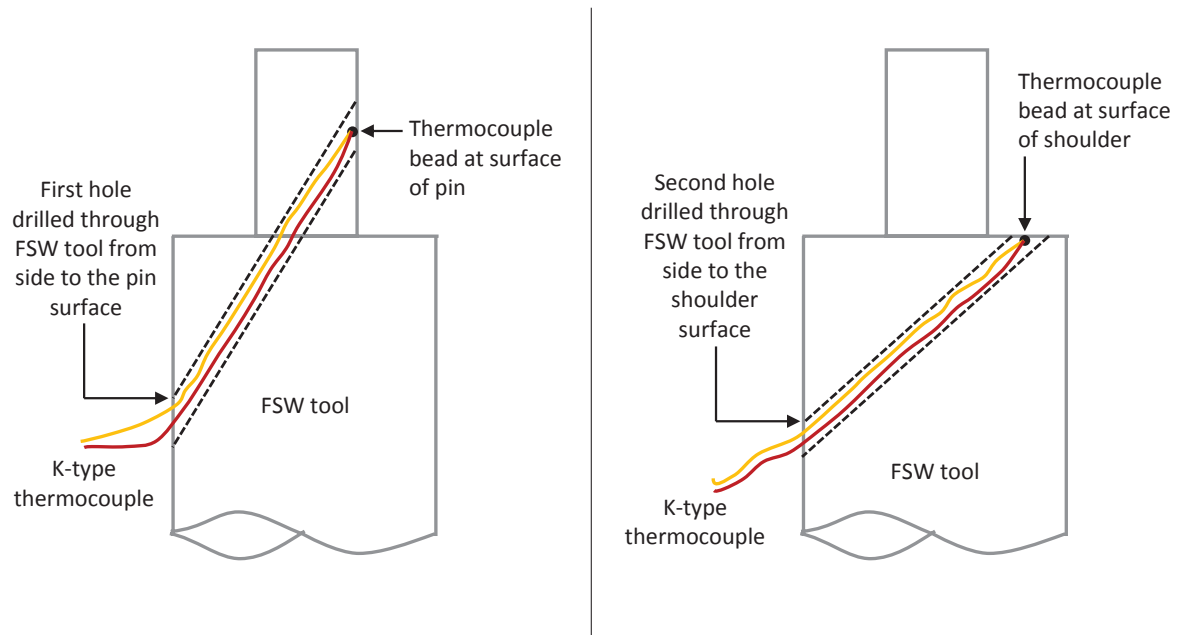
Figure 3.2: Schematic of thermocouples embedded into the FSW tool

Figure 3.3: Experimental set-up to measure FSW tool pin and shoulder temperature

A and F where a rotational speed of 1723 RPM was used instead of 1225 RPM. This was done because the small 3 mm pin on tools A and F were breaking when tool rotation speed was too low.

The substrate used for experiments was a 5000 series aluminum, Al5059. Aluminum 5059 was used because the alloy cannot be heat treated, so heat generated during welding would not alter the strength of the material (AZO, 2013). Hence, multiple welds can be performed on the same plate without affecting each other. Aluminum 5059 alloy may be strengthened by cold mechanical work or strain hardening, but each experiment was performed on an unwelded section of the substrate. Welds were spaced approximately 1 cm apart from each other.

The MSR 145B data acquisition has onboard memory and records temperature readings at a rate of 1 Hz. Temperature measurements taken from the MSR 145B data acquisition system are exported as .msr files which can be viewed by using the provided software (MSR 5.24.00). The collected thermocouple data is represented via graph from the MSR software, but can be exported into a Microsoft Excel file for additional analysis. During friction stir welding, the temperature of the pin and shoulder are expected to reach steady state temperature. Steady state is shown by a plateau in the temperature and can be measured at the relevant portion of the graph and reading along the y-axis. Although multiple plateaus can be identified in the graph, measurements were only taken at the plateau right before the tool was extracted. This location on the graph was chosen to allow the maximum amount of time to have passed to reach a steady-state welding temperature. An example of temperature measurement by reading the MSR graph is shown in Figure 3.4. Multiple experiments were performed for each FSW tool. The average of the recorded steady state temperatures values was calculated so comparisons

between tools could be made. Standard deviation was also calculated to generate error bars using t-test distribution (discussed later).

In circumstances where noise is visible in the plateau region, the portion of the data near the end of the weld before tool extraction can be averaged in Excel to record a single measurement. The temperature measurements recorded using an average used at least 30 points (ie. 30 seconds) of data. For example, in Figure 3.5 the temperature measurements for thermocouple 1 (T1) had a variance of ± 5 °Cbased off the graph readings so an average was used to measure the steady state temperature.

3.2.2   Substrate measurements

In addition to measuring the temperature from the FSW tool, the temperature of the weld from the perspective of the welded plate was also measured. The material of the substrate was Al5059. The data acquisition system used to record welding temperature was a National Instrument USB-6351 unit, NIDAQ 955-1 software, and a custom program written in LabVIEW. Results from LabVIEW were exported to Microsoft Excel and plotted. Two to three holes were drilled halfway into the substrate and K-type thermocouples (model #5TC-GG-K-36-36) were inserted into these holes and held in place using OMEGABOND 600 cement (Figure 3.6). The substrate thermocouple would make contact on the FSW tool at approximately the mid point of the length of the pin. The base plate with the embedded thermocouples was secured on top of the load cell, and welds were made on top of the thermocouple locations (Figure 3.7).

As a friction stir weld was performed, the FSW tool would run over the thermo-
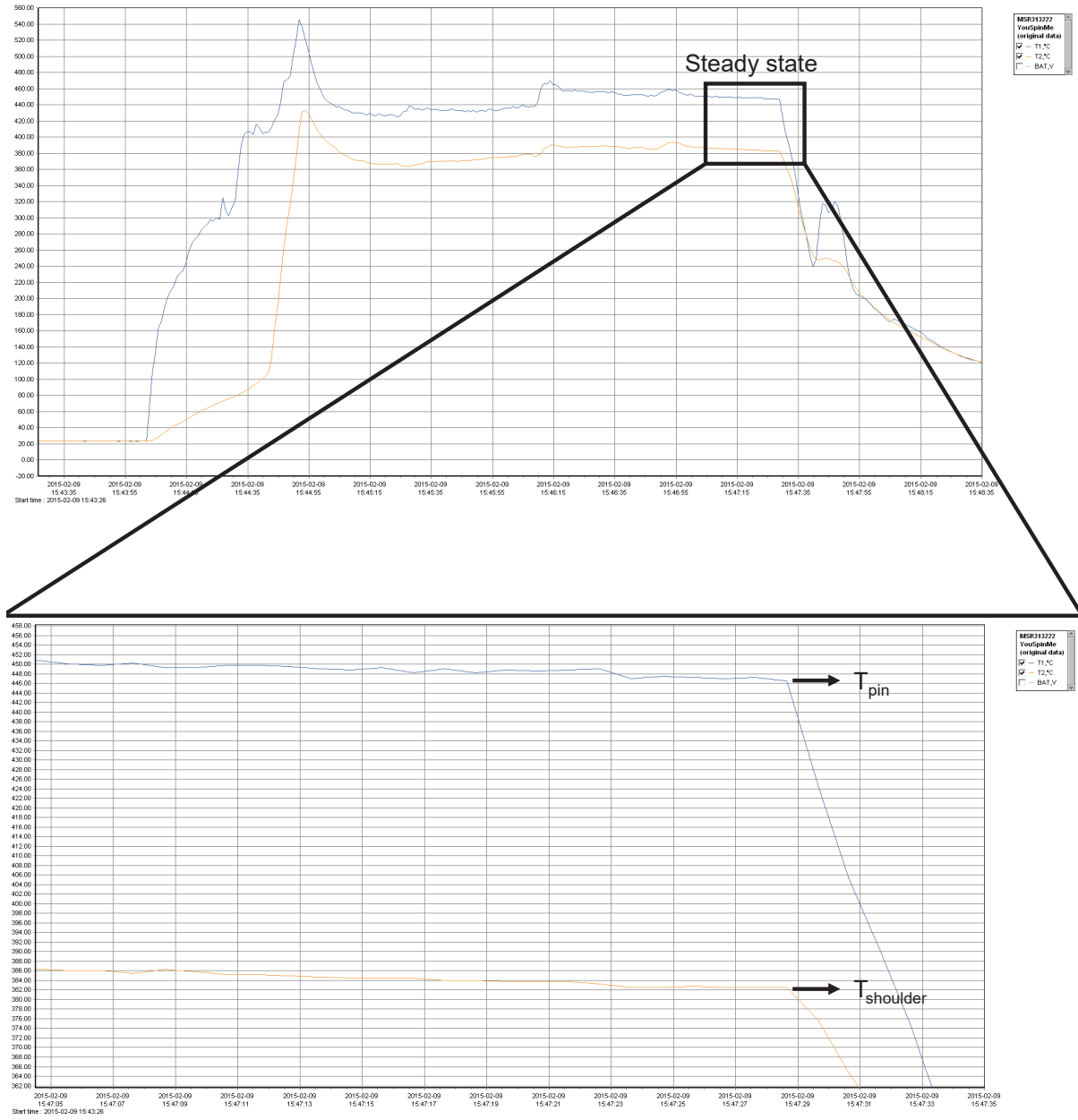
Figure 3.4: Temperature data output from the MSR 145B data aquisition for tool G (pin and shoulder temperature)
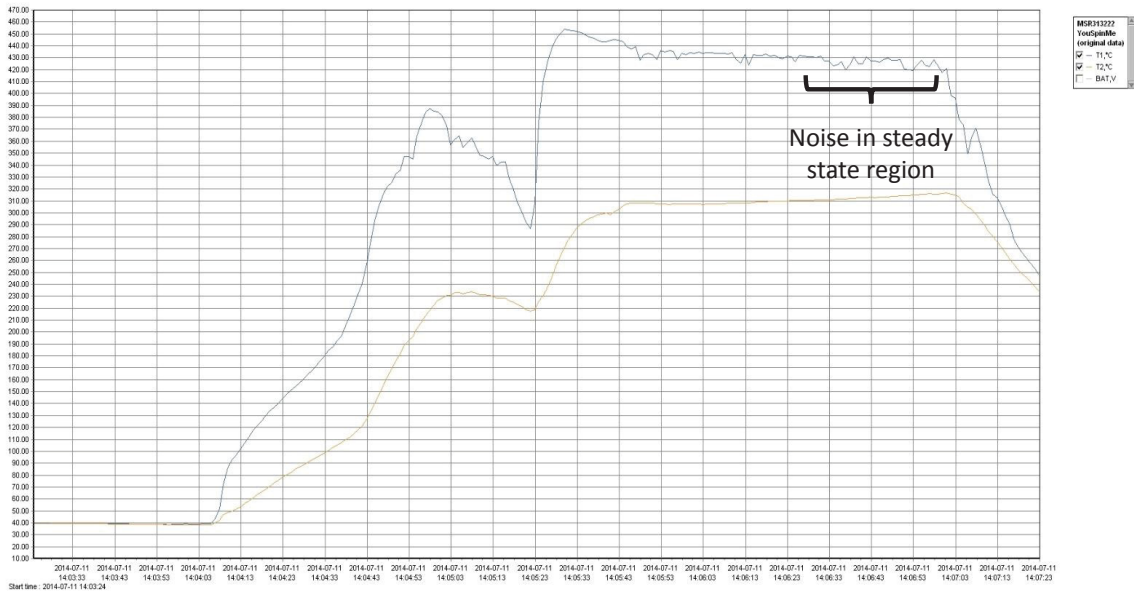
Figure 3.5: Temperature data output from the MSR 145B data aquisition for tool B (pin and shoulder temperature)
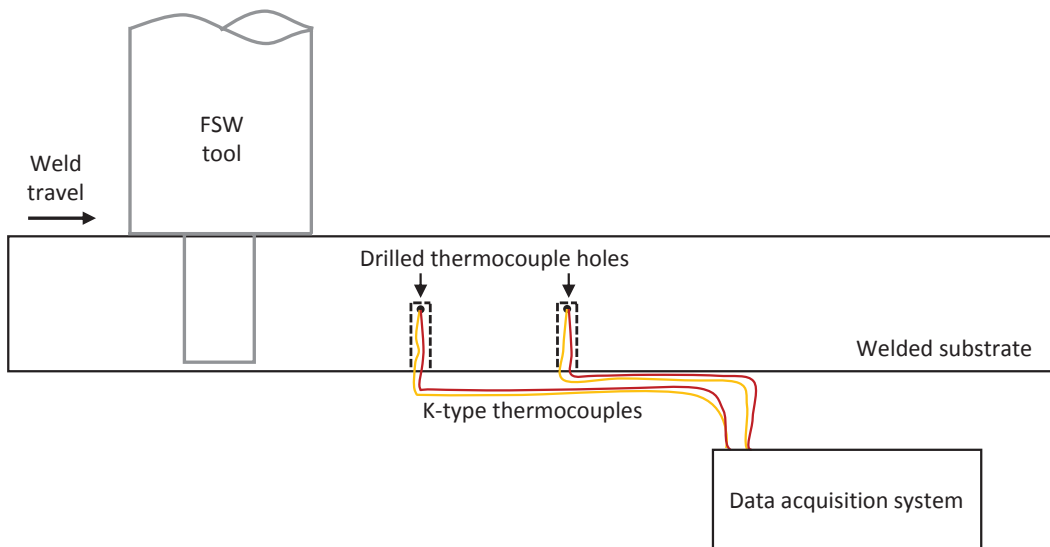
Figure 3.6: Schematic of thermocouples embedded into the welded substrate
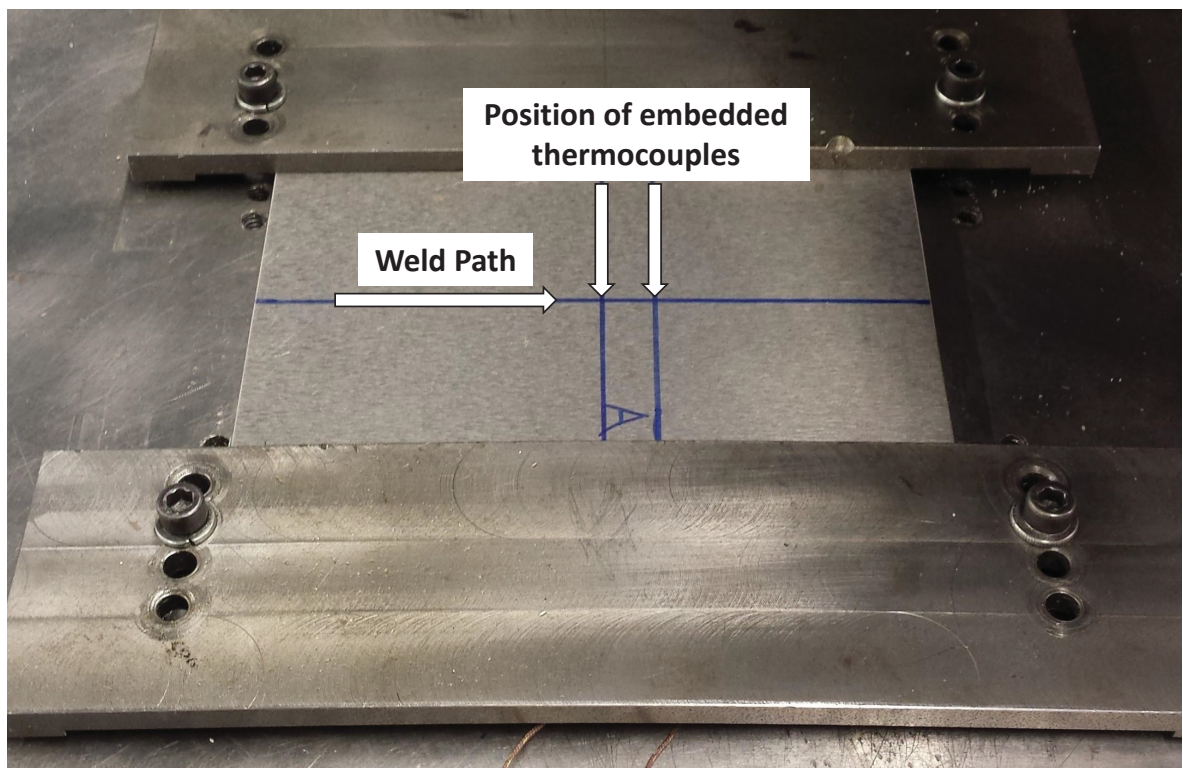
Figure 3.7: Al5059 substrate with two embedded thermocouples mounted on top JR3 load cell

couples embedded into the base plate and a peak temperature would be recorded by the NI USB-6351 system. Unlike the thermocouple located on the FSW tool, the static thermocouples in the plate would not be in contact with the FSW tool long enough to reach steady state temperature. Instead, a peak temperature would be measured by the substrate thermocouples when the FSW tool pin made contact. The rate of measurement for the NI USB-6351 was set to 1000 Hz.

Moving averages are typically used to smooth out data readings by filtering out noise caused by random fluctuations (Investopedia, 2005). Due to the temperature measurements being quite erratic, a simple moving average with low time period was used to determine a more conservative peak welding temperature (as shown by the trend line) instead of choosing the maximum temperature measured by the data acquisition system. Results were magnified in Microsoft Excel to record measurements. Figure 3.8 is an example of what the temperature recordings appear as and how the temperature peaks are identified.

3.2.3 Comparison of pin measurements and substrate measurements

In order to directly compare temperature measurements between the tool pin and substrate, the MSR 145B data acquisition was used simultaneously with the NI USB-6351 data acquisition. For experiments where the two data acquisition system were not used simultaneously there was no comparison made between the pin and substrate temperature. Figure 3.9 is an example of the temperature profiles recorded at the pin surface along with three embedded thermocouples in the substrate plate for tool G. The entire
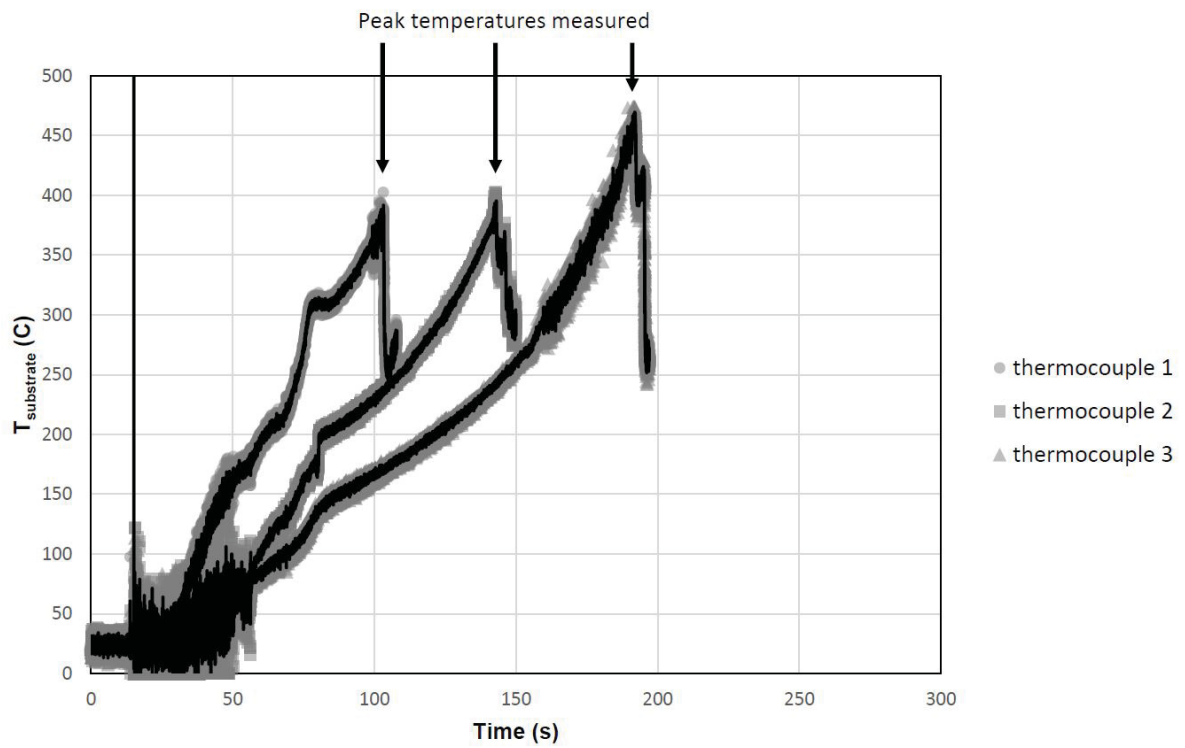
Figure 3.8: Peak welding temperature measured from the Al5059 substrate (tool G)

process of selecting the appropriate part of the graphs to measure has been explained in previous sections.
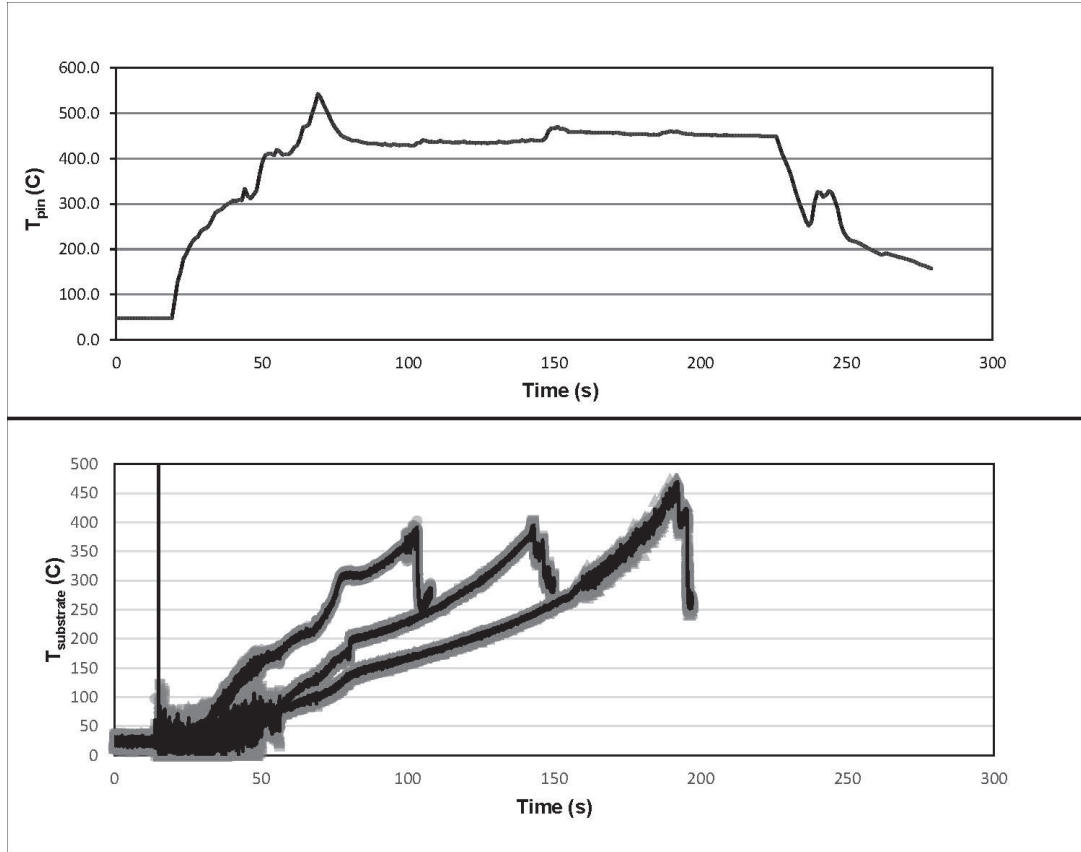
Figure 3.9: Comparison of pin and substrate temperature (tool G)

A regression analysis was performed with Microsoft Excel to determine how much influence the pin/shoulder diameter has on temperatures measured from the pin versus the substrate. To calculate this the following equation was set up:

$$\Delta T_{experimental} = X_1 + X_2 \cdot 2(a - a_{centre}) + X_3 \cdot 2[(b - a) - (b - a)_{centre}] \tag{3.1}$$

where $\Delta T_{experimental} = T_{pin} - T_{substrate}$, $X_\#$ is the constant determined from regression analysis and represents the approximate weight of the variable it is multiplied against,

a is tool pin radius, a_{centre} is the median pin radius from Table 3.2, b is tool shoulder radius, and b_{centre} is the median shoulder radius from Table 3.2. The values of X_1, X_2, and X_3 are listed in Table 4.12.

3.2.4 Post-weld thermocouple calibration

A Carbolite furnace (type 12/23) was used to recalibrate all thermocouple readings collected during friction stir welding experiments. The FSW tools and welded plates were placed in the furnace along with an undamaged control thermocouple. The furnace temperature was raised to 100°Cand held for 3 hours before temperature readings were measured from the tool, plate, and control thermocouple using the MSR 145B data acquisition system. The furnace temperature was raised another 100 degrees, held for 3 hours, and this process was repeated until 500°C.

Calibration curves were generated from the data to correct initial experimental temperature measurements. An example of a calibration curve is shown below in Figure 3.10. Thermocouple calibration was performed if the thermocouple was not severed after welding. For tools and welded plates whose thermocouples were broken off during welding, calibration curve equations from different tools and plates were applied (e.g. tool A's calibration equation was applied to tool D's measurements).

3.2.5 Confidence interval of temperature measurements

Due to the limited number of experiments that could be performed, the Students t-distribution was used to determine the 95% confidence interval of the recorded average welding temperature for both FSW tools and substrate. The confidence interval was used as a visual representation of error on graphs comparing the temperature data. To find
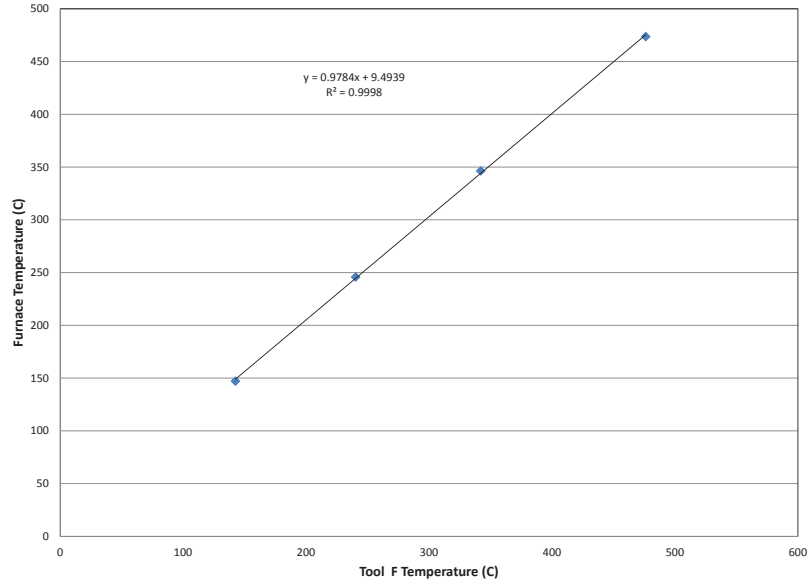
Figure 3.10: Temperature calibration curve for tool F

the confidence interval the following formula was used:

$$CI = \left(\overline{T} - t_{\alpha/2}\frac{S}{\sqrt{n}}, \overline{T} + t_{\alpha/2}\frac{S}{\sqrt{n}}\right) \tag{3.2}$$

where CI is the confidence interval, $\overline{T}$ is the average measured temperature, α is the probability value (5%), S is the calculated standard deviation, n is the number of experiments, and t is the t-distribution value.

3.3 Force and torque measurements during welding

3.3.1 Load cell set-up

All welding force experiments were performed using an INDUMA milling machine which was converted into a friction stir welder. To measure and record the force during friction stir welding a JR3 6-axis load cell (model #75E20S4-M125A-AF) data acquisition system was used in combination with an NI SCC-68 unit, NI USB-6251 unit, and Lab-VIEW SignalExpress software (v. 2.5.1). The JR3 load cell was bolted to the table of the milling machine, and a steel backing plate (320 x 320 x 24 mm) was placed on top of the load cell. The substrate to be welded on was secured to the top of the steel backing plate using screws. With the substrate fastened down, the data acquisition software was turned on and a weld was performed on top of the substrate. The JR3 load cell was used simultaneously with the MSR 145B (tool temperature) and NI USB-6351 (substrate temperature) data acquisition systems. The different data acquisition systems were synchronized based off their graphical output by lining up identified regions of tool plunge and tool extraction. Force data was recorded at a frequency of 100 Hz and exported into a Microsoft Excel format for graphical display and further analysis. The complete set of force data recorded for each experiment contains six sets of measurements, torque in the x-y-z direction and force in the x-y-z direction. A picture of the experimental set up is shown in Figure 3.11, and x-y-z orientation relative to the load cell are shown in Figure 3.12.

Substrate

Backing plate
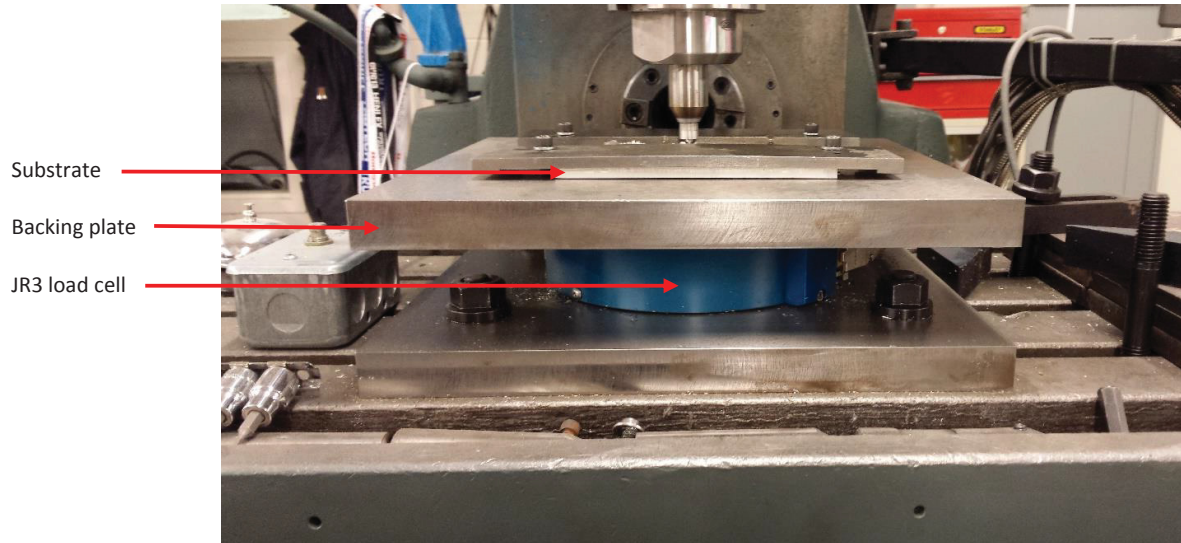
JR3 load cell

Figure 3.11: JR3 force load cell set-up

3.3.2 Force measurements

Force in the x-y-z directions were read similarly to tool pin and shoulder temperatures. The steady state portion of the data was measured from the graph near the end of the weld before tool extraction. Although multiple steady state regions along the force graph may be identified, the portion near the end of the weld was taken to be consistent with where temperature measurements were recorded from. A moving average trend line was used to reduce the wide spread of data into a more easily measured value. An example of a force graph and how the value was measured from the trend line is shown in Figure 3.13.
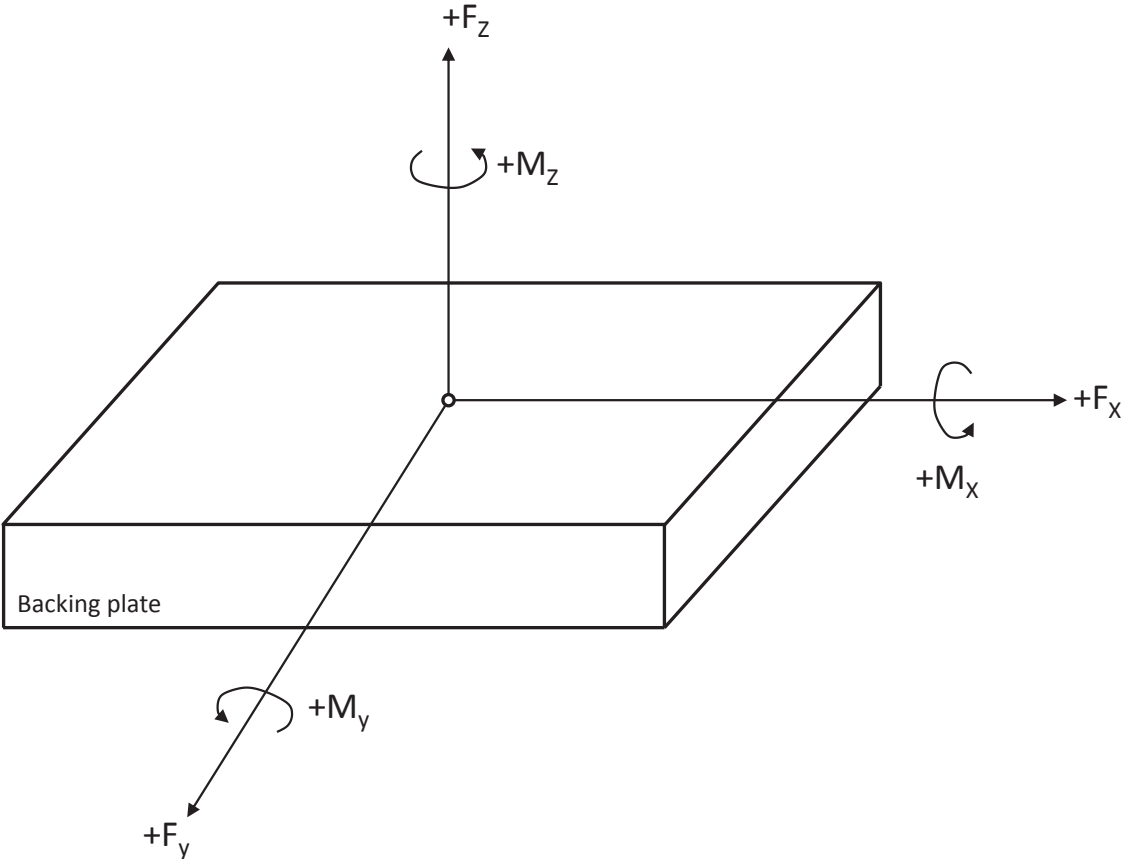
Figure 3.12: Force orientation of the JR3 load cell
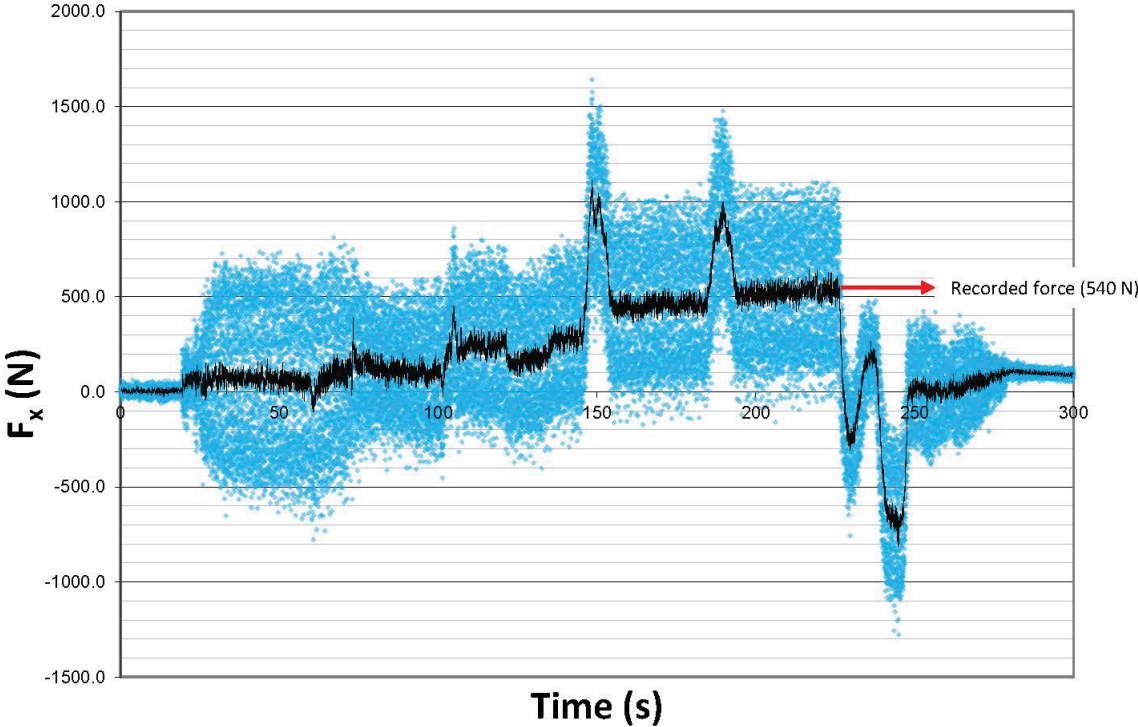
Figure 3.13: Tool G x-axis force measurement from graph

3.3.3 Torque measurements

Since torque measurements are taken relative to what the load cell experiences, corre-lating torque readings from the JR3 load cell to the FSW tool requires knowing where the FSW tool was during recording. Raw torque measurements from the JR3 load cell are only valid (i.e. load cell torque is equal to FSW tool torque) when the FSW tool is positioned exactly over the center of the load cell (position along the x-axis and y-axis is zero relative to the load cell). Since all welds involved traveling along the surface of the substrate, it was difficult to determine the exact moment when the FSW tool was positioned correctly along the x-axis to take a reading off of the output graph. Human error could also cause torque measurements to be inaccurate in the case that the FSW tool was positioned incorrectly along the y-axis prior to welding. Reading torque directly from the output graphs was not viable. Therefore, the FSW tool torque was calculated from the load cell torque readings.

The JR3 load cell was broken down into a free body diagram (Figure 3.14 and Fig-ure 3.15). The variables $\overline{F}_o$ and $\overline{M}_o$ are the force and torque, respectively, reported by the load cell. The variables $\overline{F}$ and $\overline{M}$ are the force and torque, respectively, experienced by the FSW tool. Distance from the center of the load cell to the FSW tool is labeled as $\overline{r}$, and d_o is the length of the backing plate and substrate thickness combined. The position where the FSW tool plunges into the substrate and begins welding relative to the zero point on the load cell are x_o and y_o.

The tool torque readings in the x-y-z direction are calculated as follows. Static bal-

LEGEND:
A. Tool plunge point
B. Tool position at time, t
C. Weld travel path
D. Backing plate
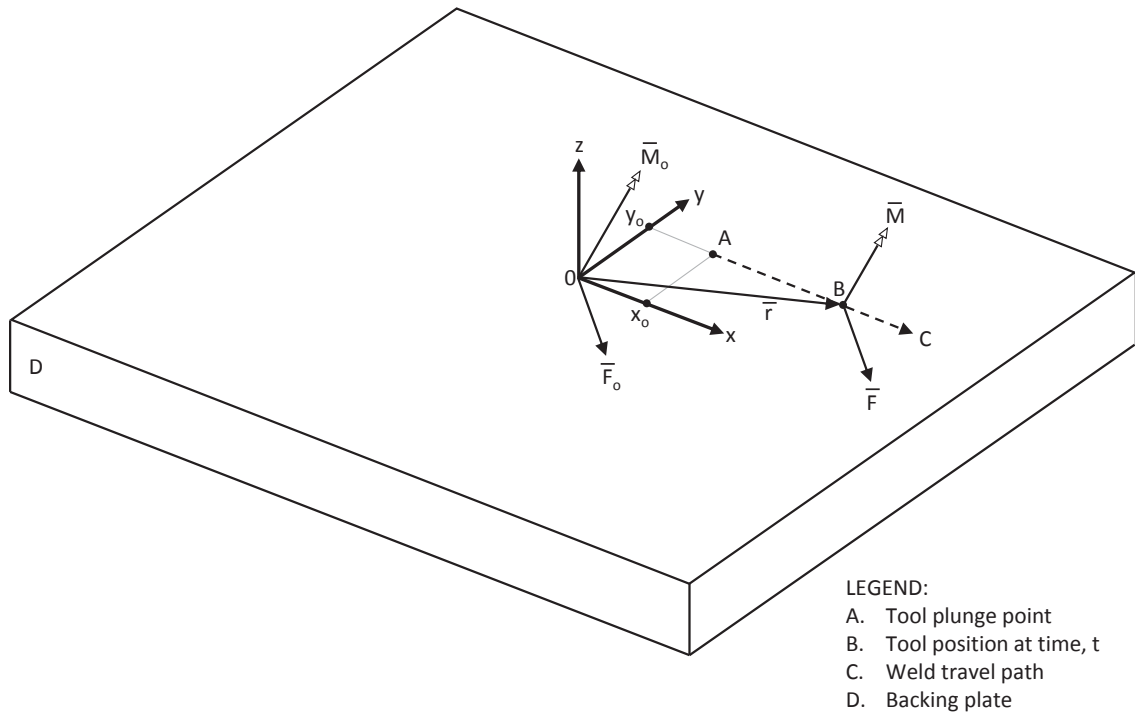
Figure 3.14: JR3 load cell free body diagram 1
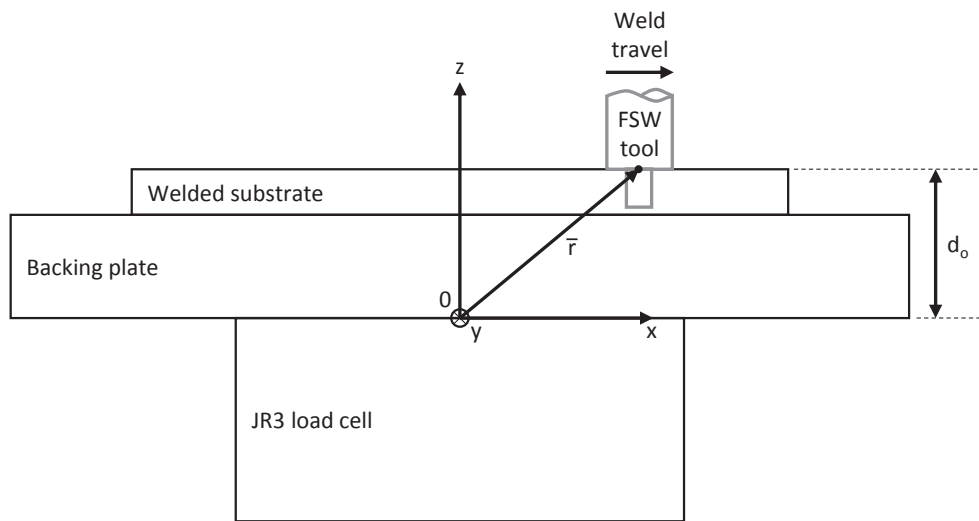
Figure 3.15: JR3 load cell free body diagram 2

ance:

$$\Sigma \overline{F} = 0 \tag{3.3}$$

$$\Sigma \overline{M} = 0 \tag{3.4}$$

The static balance for Equation 3.3 can be written as:

$$\overline{F} - \overline{F}_o = 0 \tag{3.5}$$

$$\overline{F} = \overline{F}_o \tag{3.6}$$

The static balance for Equation 3.4 can be written as:

$$\overline{M} + \overline{r} \times \overline{F} - \overline{M}_o = 0 \tag{3.7}$$

$$\overline{M} = \overline{M}_o - \overline{r} \times \overline{F}_o \tag{3.8}$$

The cross product, $\overline{r} \times \overline{F}$ can be expanded upon:

$$\overline{r} \times \overline{F} = \begin{vmatrix} \overline{e}_x & \overline{e}_y & \overline{e}_z \\ x & y & z \\ F_{ox} & F_{oy} & F_{oz} \end{vmatrix} \tag{3.9}$$

$$= (yF_{oz} - zF_{oy})\overline{e}_x + (zF_{ox} - xF_{oz})\overline{e}_y + (xF_{oy} - yF_{ox})\overline{e}_z \tag{3.10}$$

In Equation 3.10, x, y, and z are defined as:

$$x = x_o + v_t t \tag{3.11}$$

$$y = y_o \tag{3.12}$$

$$z = -(d_1 + d_2) = -d_o \tag{3.13}$$

where v_t is the travel speed of the FSW tool and is measured experimentally (15.28 mm/min), t is time, and d_o is the combined thickness of the backing plate and welded substrate (30.5 mm). The only unknown variables are x_o and y_o which will be estimated. Substituting Equation 3.10 into Equation 3.8 results in three equations to calculate torque for the FSW tool pin in the x-y-z direction based on measurements taken from the JR3 load cell.

$$M_x = M_{ox} - y_o F_{oz} - d_o F_{oy} = 0 \qquad (3.14)$$

$$M_y = M_{oy} + d_o F_{ox} + (x_o + v_t t) F_{oz} = 0 \qquad (3.15)$$

$$M_z = M_{oz} - (x_o + v_t t) F_{oy} + y_o F_{ox} \qquad (3.16)$$

The only unknowns in Equation 3.14, Equation 3.15, and Equation 3.16 are x_o and y_o. A simplification is made that torque along the x-axis and y-axis with respect to the FSW tool are zero, because the FSW tool is only spun along the z-axis and is held rigidly in place within the machine spindle. The original data collected from the JR3 load cell is used with Equation 3.14, Equation 3.15, and Equation 3.16, and new torque values are calculated and graphed which are from the perspective of the FSW tool. A moving average trend line is used to make the data easier to read and make measurements.

Starting with Equation 3.14 the value of y_o is adjusted manually until the value of M_x is equal to the zero reading after FSW tool extraction from the substrate (Figure 3.16). Next, the value of x_o is manually adjusted until the value of M_y is equal to the zero reading after FSW tool extraction from the substrate (Figure 3.17). It should be noted that the zero reading of the JR3 load cell after FSW tool extraction is not always exactly at zero. The reason for this may be due to residual stress between the clamped substrate

and backing plate. Once x_o and y_o are found, the value of M_z (tool torque along the z-axis) can be calculated and graphed. The FSW tool torque reading (M_z) can be read off the new graph as shown in Figure 3.18.
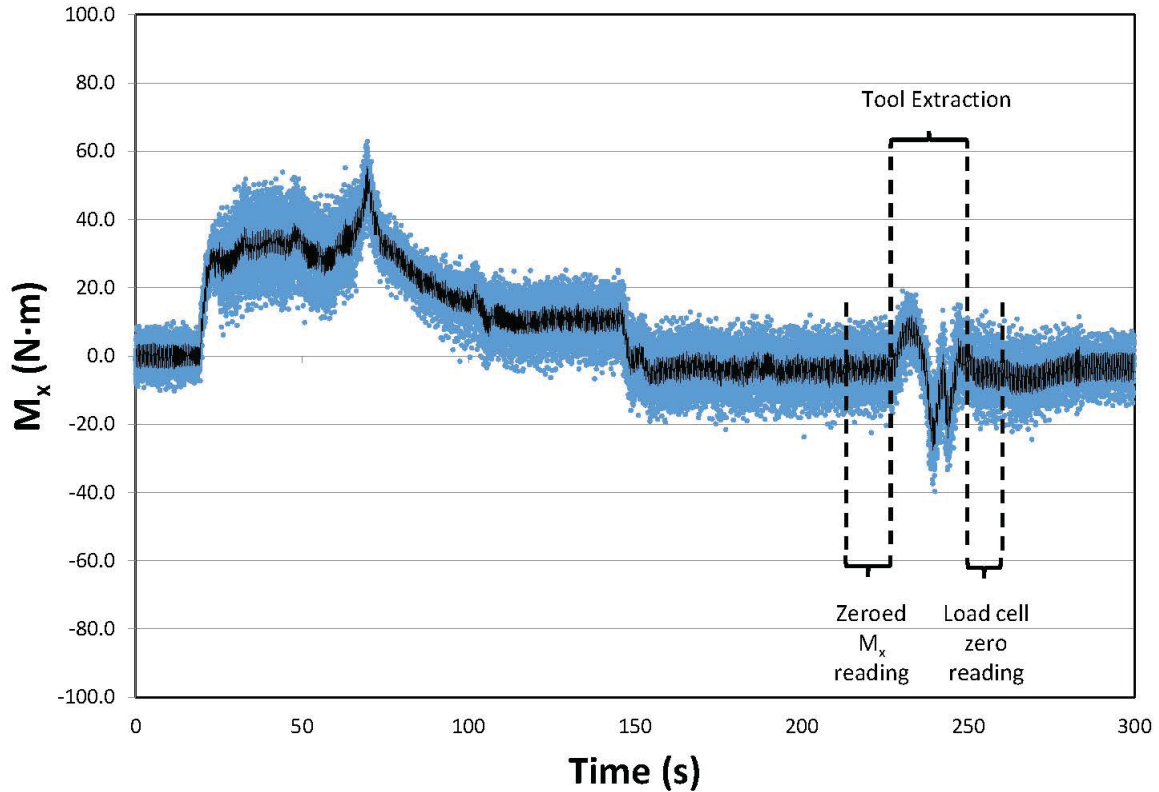
Figure 3.16: Tool G torque measurement zeroed along the x-axis

3.4 Friction stir welding temperature and torque prediction

The maximum temperature at the shear layer can be predicted using Equation 2.6 and Equation 3.18 which only requires the operating parameters, tool pin size, and thermomechanical behaviour and thermophysical properties of the substrate. The predicted
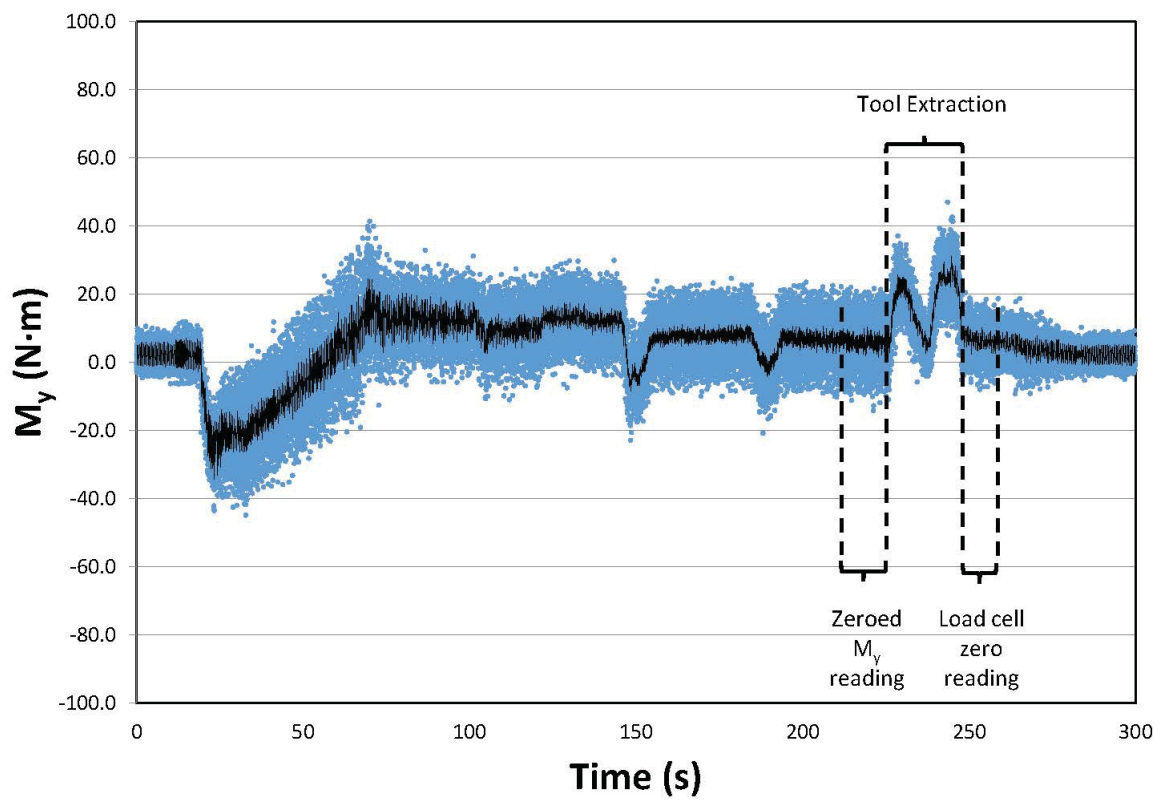
Figure 3.17: Tool G torque measurement zeroed along the y-axis
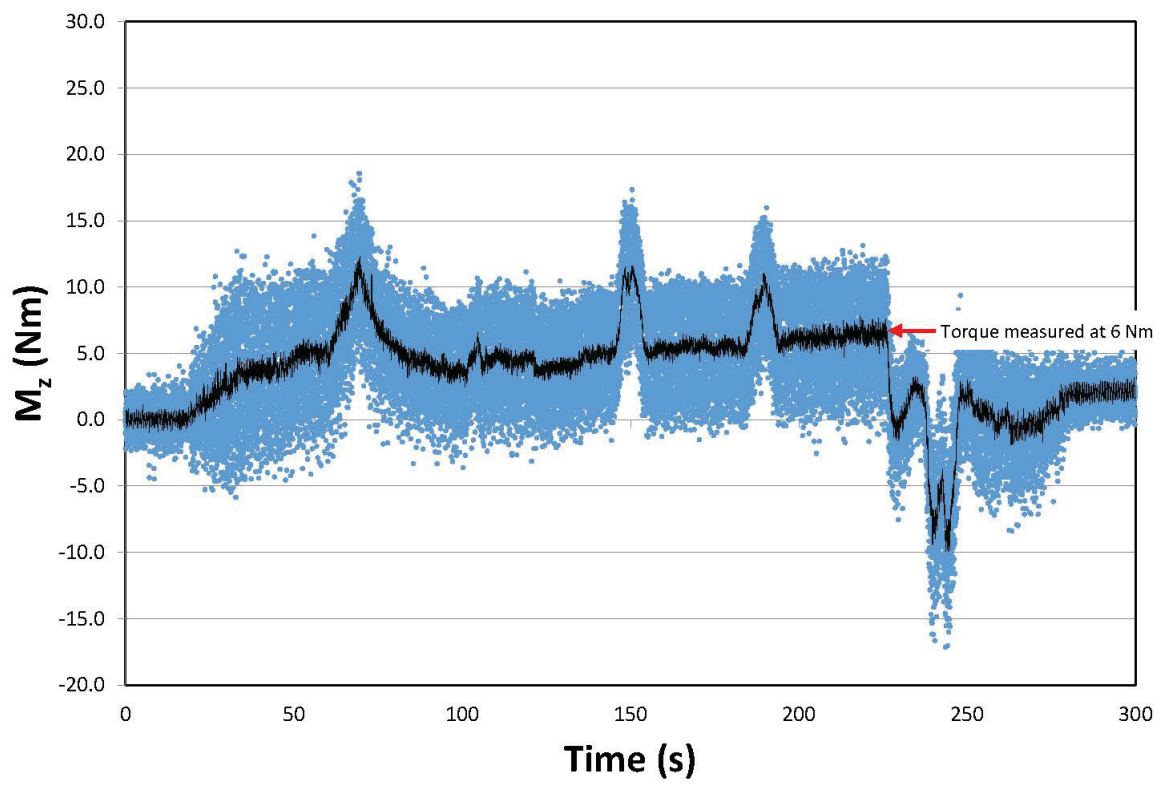
Figure 3.18: Tool G torque measurement along the z-axis

welding temperature was improved by performing minimum least squares regression analysis (Equation 3.17) using MATLAB to determine the coefficients in Equation 2.10. From Equation 2.10 only the $\hat{\delta}/a$ term is initially considered. The improved welding temperature prediction is given by Equation 3.19. The data used for the regression analysis was the experimental temperature data collected at the Canadian Centre for Welding and Joining (CCWJ) as well as FSW temperatures from literature collected by Tello (Tello, 2008). The temperatures from literature were composed of a large collection of different metals and are shown in the appendix.

$$\phi = Min \sum_{i}^{n} \left(\log(X) - \log(\widehat{X}^+) \right)^2 \tag{3.17}$$

$$\widehat{T_s} = \widehat{\Delta T_s} + T_o \tag{3.18}$$

$$\widehat{T_s}^+ = \widehat{T_s} \cdot C_1 \left(1 + C_2 \frac{\hat{\delta}}{a} \right)^{C_3} + T_o \cdot C_4 \tag{3.19}$$

In order to fully study the effects of the pin and shoulder diameter with the proposed tool matrix, the $(b - a)/\hat{\delta}$ term was later included from the correction function (Equation 2.10). The improved temperature prediction that accounts for both $\hat{\delta}/a$ and $(b-a)/\hat{\delta}$ is given by Equation 3.20. The correction coefficients were tabulated using MATLAB

and the results are listed in Table 4.14.

$$\widehat{T_s}^+ = \widehat{T_s} \cdot C_5 \left(1 + C_6 \frac{\hat{\delta}}{a}\right)^{C_7} \left(1 + C_8 \frac{b-a}{\hat{\delta}}\right)^{C_9} + T_o \cdot C_{10} \tag{3.20}$$

The improved estimation of welding temperature was compared to experimental values and the margin of error was calculated between the two values. For the purpose of this study, the margin of error is defined as the percentage difference between the corrected theoretical value of temperature and the experimentally measured value. The margin of error is given by Equation 3.21.

$$m_e = \left| 100 - \frac{\widehat{T_s}^+}{T_s} \times 100 \right| \tag{3.21}$$

Using the known operating parameters, tool size, and substrate material properties from prior experiments, Equation 2.7 was used to predict torque. The tabulated torque values were corrected using Equation 2.14. Similarly to the temperature prediction, the $(b-a)/\hat{\delta}$ term was later accounted for from the correction function (Equation 2.10) and is given by Equation 3.22. The correction coefficients were tabulated using MATLAB and the results are listed in Table 4.24.

$$\widehat{M}^+ = \widehat{M} \cdot C_{11} \left(1 + C_{12} \frac{b-a}{\hat{\delta}}\right)^{C_{13}} \tag{3.22}$$

The predicted torque values were compared directly against torque values measured using the JR3 load cell from experimentation. The margin of error was calculated using a ratio of the tabulated value and measured value of torque (Equation 3.23). The margin

of error is the percentage difference between the corrected theoretical value of torque and the experimentally measured value.

$$m_e = \left| 100 - \frac{\widehat{M}^+}{M} \times 100 \right| \tag{3.23}$$

Chapter 4

Results

The following chapter will present the experimental results and calculations for temperature, force, and torque during friction stir welding. This will cover:

- Pin and shoulder temperature measurements

- Substrate temperature measurements

- Comparison between temperatures measured from the tool versus the substrate

- Theoretical temperature calculations

- Force and torque measurements

- Theoretical torque calculations

4.1 Temperature measurements during friction stir welding

4.1.1 FSW pin and shoulder measurements

Temperature measurements were taken directly from the FSW tool using the methods described in section 3.2. Measuring temperature directly from the tool provides a signifi-

cant amount of information and various portions of the welding process can be identified on the graph collected from the MSR 145B data acquisition system. These portions include the tool plunge, weld travel, steady state, running over thermocouples embedded into the substrate, and tool extraction. These are labeled in Figure 4.1.
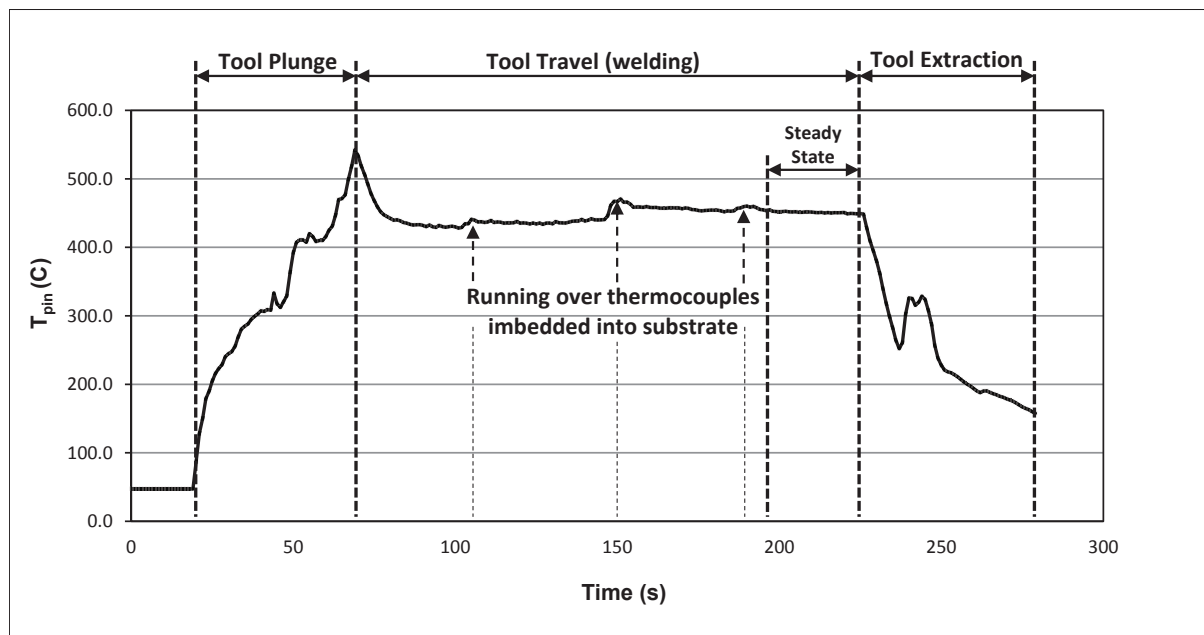
Figure 4.1: Temperature profile of the pin (tool G) during friction stir welding

The complete list of temperature results are in Table 4.1 (smooth surface tool pin) and Table 4.2 (threaded surface tool pin). The measured temperatures for each tool were averaged together, and the difference between the pin and shoulder temperature was calculated. These results are summarized in Table 4.3. The difference in temperature between the pin and shoulder ranges from as low as 12.2 °Cto as high as 68.2 °C. The data for tool pin temperature for tool C was not be measured due to the tool pin breaking off during welding. However, it is a relatively conservative estimate that the tool pin temperature for tool C was at least 488.3 °C(measured shoulder temperature + lowest ΔT between the pin and shoulder; 476.1 + 12.2 °C).

Table 4.1: Temperature measurements during FSW for tools A through E

Tool i.d.	Pin Temperature (°C)	Shoulder Temeprature (°C)
A	399.7	377.9
	396.9	379.8
	387.4	368.4
	389.3	375.1
	399.7	389.3
	397.8	389.3
B	497.6	497.6
	443.7	397.6
	446.6	403.5
C	-	476.6
D	430.0	371.3
	439.5	375.1
	437.6	366.5
	437.6	-
	431.0	-
E	495.4	447.1
	470.8	428.1
	487.9	454.7
	497.3	466.1

Temperature calibration curves were made following the procedure outlined in section 3.2 and the results are in Table 4.4. The calibration curves were used to correct the raw data in Table 4.3 and the corrected temperatures are summarized in Table 4.5. The data used to generate the calibration curves are in the appendix (section 6).

The 95% confidence interval was tabulated for the pin temperature measurements using Equation 3.2. The shoulder temperature measurements were not included, because only maximum welding temperature was being compared which was recorded at the tool pin. The confidence interval results are shown in Table 4.6.

Table 4.2: Temperature measurements during FSW for tools F through J

Tool i.d.	Pin Temperature (°C)	Shoulder Temeprature (°C)
F	422.4	410.4
G	451.8	390.2
	459.4	409.2
	453.7	403.5
	456.6	412.0
	447.1	394.0
H	458.5	420.6
	467.9	424.3
	456.6	392.1
	458.5	412.0
	447.1	379.8
I	446.3	405.7
	353.3	363.6
	439.4	352.9
	447.2	374.4
	429.6	361.7
	436.5	371.5
	435.5	368.5
J	471.7	437.6
	476.5	432.9
	475.5	427.2
	478.4	440.5
	470.8	428.1

Table 4.3: Average temperature measurements during FSW for tools A through J (*conservative estimate for tool C)

Tool i.d.	Average Pin Temperature (°C)	Average Shoulder Temperature (°C)	△T (°C)
A	390.1	374.2	15.9
B	446.5	401.0	45.5
C	488.3*	476.1	-
D	432.3	364.6	67.7
E	488.0	447.0	41.0
F	422.0	409.8	12.2
G	452.0	397.2	54.8
H	456.2	401.4	54.8
I	439.7	371.5	68.2
J	474.0	430.4	43.6

Table 4.4: Temperature calibration curves for tools A through J

Tool i.d.	Temperature Calibration formula	(Calibration no. used)
A	y = 0.9479*x + 25.278	1
B	y = 0.9796*x + 7.7662	2
C	y = 0.9458*x + 27.378	3
D	y = 0.9479*x + 25.278	1
E	y = 0.9479*x + 25.278	1
F	y = 0.9784*x + 9.4939	4
G	y = 0.9479*x + 25.278	1
H	y = 0.9479*x + 25.278	1
I	y = 0.9784*x + 8.9103	5
J	y = 0.9479*x + 25.278	1

Table 4.5: Corrected average temperature measurements during FSW for tools A through J

Tool i.d.	Average Pin Temperature (°C)	Average Shoulder Temperature (°C)
A	395.1	380.0
B	445.2	400.6
C	488.6	476.6
D	435.1	370.9
E	487.9	449.0
F	422.4	410.4
G	453.7	401.8
H	457.7	405.8
I	439.1	372.4
J	474.6	433.3

Table 4.6: Confidence interval (95%) for pin temperature measurements

Tool i.d.	N	$\overline{T}$ (°C)	S (°C)	95% C.I.
A	6	395.1	5.4	5.7
B	2	445.2	2.1	18.7
C	0	-	-	-
D	3	435.1	4.3	10.7
E	4	487.9	12.1	19.2
F	1	422.4	-	-
G	5	453.7	4.7	5.8
H	5	457.7	7.4	9.2
I	6	439.1	6.7	7.0
J	5	474.6	3.2	4.0

4.1.2   Substrate measurements

Between three to five successful temperature measurements were taken from the substrate
for experiments using tools A, B, F, G, H, I and J. Data from the substrate was not
taken for tools C, D, or E due to the FSW tool breaking in previous trials before the NI
USB-6351 was implemented. A complete list of the temperature data collected from the
substrate is in Table 4.7.

Table 4.7: Temperature measurements during FSW for plates i through xiii

Tool i.d.	Plate i.d.	Temperature (°C)
A	i	330.0
		322.0
A	ii	346.0
		338.0
B	iii	442.0
		421.0
B	iv	415.0
B	v	385.0
F	vi	360.0
		370.0
		368.0
F	vii	-
G	viii	391.0
		395.0
		470.0
H	ix	425.0
		450.0
		450.0
I	x	391.4
		426.3
I	xi	-
I	xii	414.0
J	xiii	423.0
		420.0
		449.0

The substrate temperature measurements were also corrected using calibration curves. Calibrations were done for plates i, ii, iv, and v. The resulting equations used for each substrate plate are listed in Table 4.8, and the data used to generate the calibration curves is in the appendix (section 6).

Table 4.8: Temperature calibration curves for substrate temperature measurements

Plate i.d.	Temperature Calibration formula	(Calibration no. used)
i	y = 1.0062*x + 14.83	6
ii	y = 0.9974* x + 22.421	7
iii	y = 1.0062*x + 14.83	6
iv	y = 0.9888*x + 19.031	8
v	y = 0.9889*x + 25.616	9
vi	y = 1.0062*x + 14.83	6
vii	y = 1.0062*x + 14.83	6
viii	y = 1.0062*x + 14.83	6
ix	y = 1.0062*x + 14.83	6
x	y = 1.0062*x + 14.83	6
xi	y = 1.0062*x + 14.83	6
xii	y = 1.0062*x + 14.83	6
xiii	y = 1.0062*x + 14.83	6

The substrate temperatures were adjusted using the calibration curves and averaged together for each tool (Table 4.9). These values represent the average maximum welding temperature measured from the perspective of the substrate with embedded thermocouples. The 95% confidence interval was tabulated for the substrate temperature measurements using Equation 3.2. The confidence interval results are listed in Table 4.10.

Table 4.9: Averaged substrate temperatures during FSW for tools A through J

Tool i.d.	Average substrate temperature (°C)
A	350.9
B	415.8
F	383.1
G	436.1
H	459.2
I	427.9
J	448.2

Table 4.10: Confidence interval (95%) for substrate temperature measurements

Tool i.d.	N	$\overline{T}$ (°C)	S (°C)	95% C.I.
A	4	350.9	10.3	16.4
B	4	415.8	23.5	37.5
F	3	383.1	5.3	13.1
G	3	436.1	44.5	60.6
H	3	459.2	14.4	35.9
I	3	427.9	17.7	44.0
J	3	448.2	15.9	39.6

4.1.3 Comparison between temperatures measured from the tool versus the substrate

To compare the pin and substrate temperatures, a graph was generated plotting the average tool pin temperature against the average substrate temperatures. The 95% confidence intervals calculated previously were used as error bars (Figure 4.2). Beside each major data point is a letter labeling which tool it represents. The dotted 1:1 line is a visual guide to see how closely the tool pin and substrate follow a similar ratio.
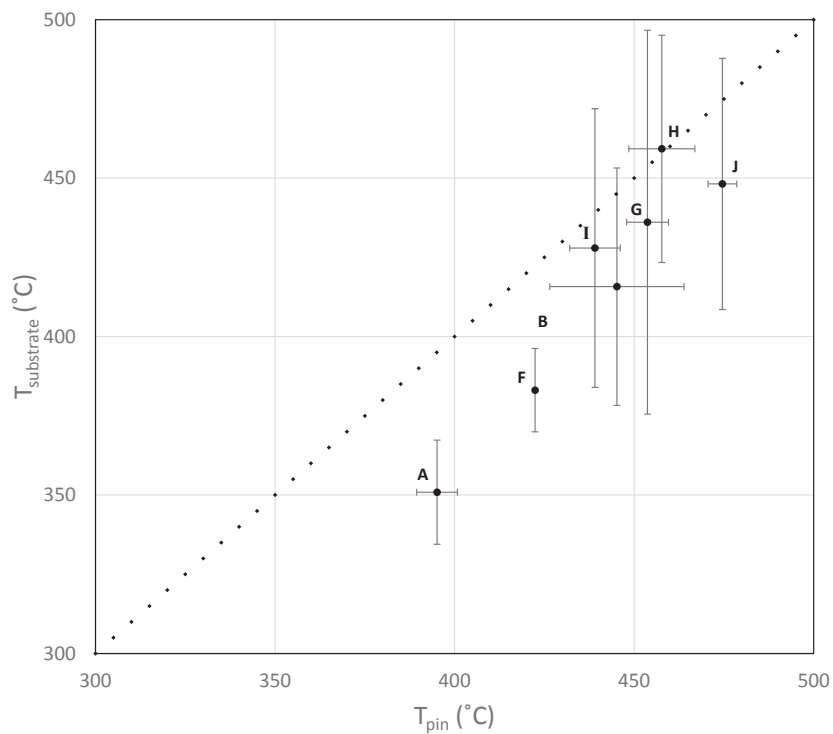
Figure 4.2: Summary comparison of pin temperature against substrate temperature (data used from Table 4.5 and Table 4.9)

The results from Figure 4.2 can be separated based on the tool groups explained in section 3.1 as per the geometry listed in Table 3.2. Tools C, D, and E have no coupled data between the tool pin and substrate due to tool damage. Since data for tool C, D, and E are absent, only the set of threaded pin tools (F through J) will be analyzed. The results can be grouped by tools FGH (Figure 4.3) and IGJ (Figure 4.4). The slope of the line for the tool groups yields information of how sensitive temperature measurements are with respect to geometry changes when measured from the FSW tool or the substrate. A slope greater than 1 indicates that greater temperature changes can be measured from the substrate compared to measurements taken from the FSW tool pin. A slope less than 1 shows that greater temperature changes can be measured from the tool pin compared to the substrate when the tool geometry changes. Further analysis of this is done in the discussion section. The actual value of the slope and equation of line is not considered because the line it forms is simply a visual reference to show sensitivity of temperature measurements.

Regression analysis outlined in section 3.2 using Equation 3.1 was done to find how much influence the pin and shoulder diameter had on welding temperature. The variables used for regression analysis are in Table 4.11, and the results are listed in Table 4.12.

4.1.4 Theoretical friction stir welding temperature calculations

Using Equation 2.6 and Equation 3.18, the maximum welding temperature during FSW was predicted for tools A through J. Note that these results have not been adjusted with the correction function yet Table 4.13. The variables used for calculations are listed in the appendix (section 6).
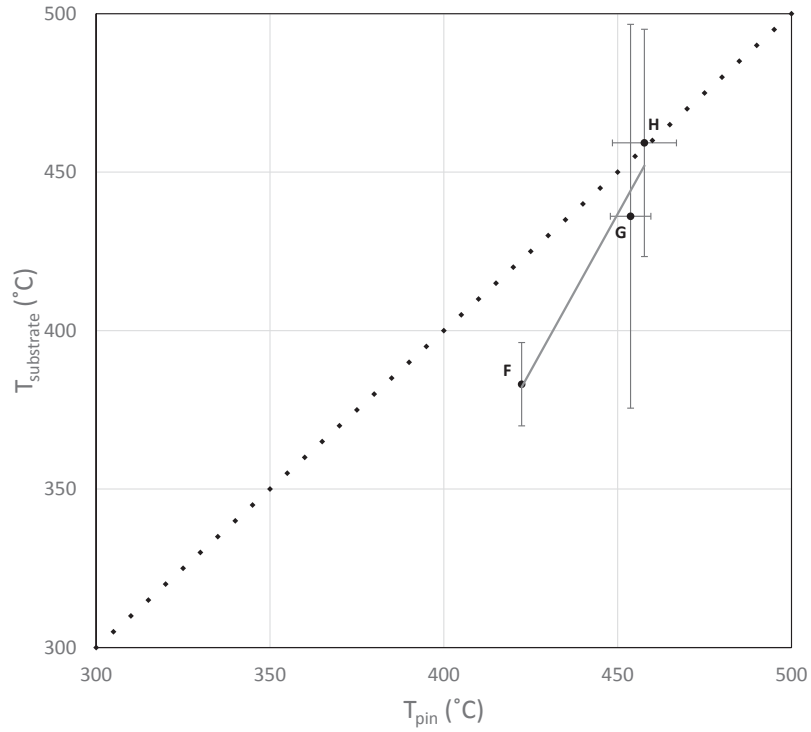
Figure 4.3: Comparison of pin temperature against substrate temperature (tools F, G, and H; Table 3.2)

Table 4.11: Variables used for regression analysis on pin and shoulder diameter

Tool i.d.	a (mm)	b (mm)	a_{centre} (mm)	b_{centre} (mm)	$2(a - a_{centre})$ (mm)	$2[(b - a) - (b - a)_{center}]$ (mm)	$\Delta T_{experimental}$ (°C)
A	1.5	4.5	2	6	-1	-2	44.2
B	2.0	6.0	2	6	0	0	29.5
F	1.5	4.5	2	6	-1	-2	39.3
G	2.0	6.0	2	6	0	0	17.6
H	2.5	7.5	2	6	1	2	-1.5
I	2.0	4.5	2	6	0	-3	11.2
J	2.0	7.5	2	6	0	3	26.4
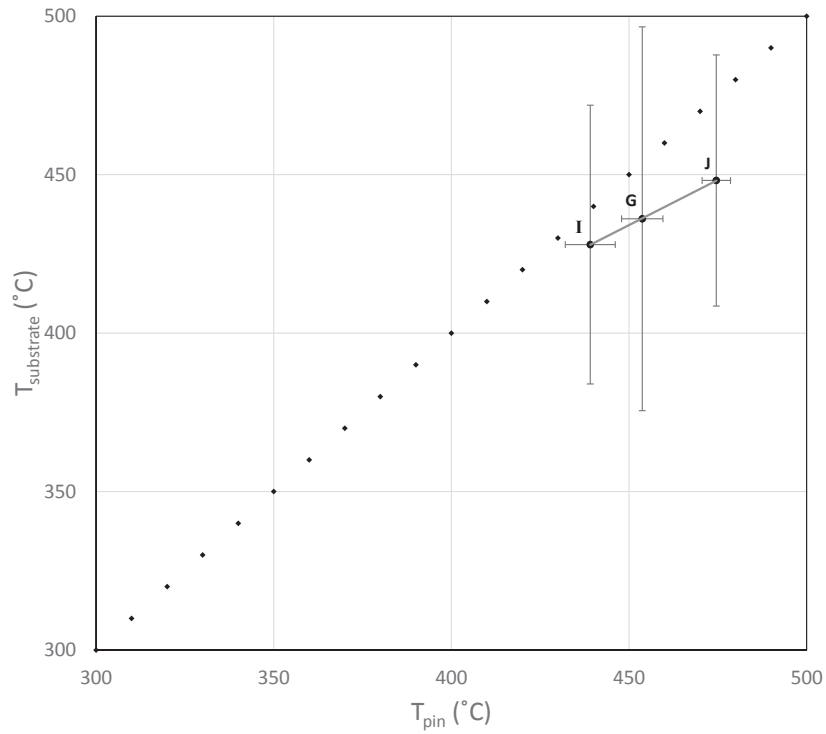
Figure 4.4: Comparison of pin temperature against substrate temperature (tools I, G, and J; Table 3.2)

Table 4.12: Tool pin and shoulder regression analysis results (Equation 3.1)

Coefficient	Regression result
X_1	20.7
X_2	-26.5
X_3	2.5

Table 4.13: Uncorrected theoretical welding temperatures during FSW (Equation 2.6; variables listed in section 6)

Tool i.d.	$\widehat{T}_s$ (K)	$\widehat{T}_s$ (C)
A	903.6	630.4
B	987.1	713.9
C	1762.5	1489.3
D	987.1	713.9
E	987.1	713.9
F	903.6	630.4
G	987.1	713.9
H	1821.9	1548.7
I	987.1	713.9
J	987.1	713.9

The correction coefficients were solved for three different cases. The first case only accounted for $\frac{\widehat{\delta}}{a}$ for all materials that data was available. The second case accounted for shoulder diameter $(\frac{b-a}{\widehat{\delta}})$ as well as $\frac{\widehat{\delta}}{a}$ for all materials that data was available. The third case accounted for $(\frac{b-a}{\widehat{\delta}})$ and $\frac{\widehat{\delta}}{a}$, but only considered the experimental data collected in-house at the Canadian Centre for Welding and Joining (CCWJ). The coefficients were calculated using MATLAB as outlined in section 3.4. All of the correction coefficients are listed in Table 4.14.

The corrected theoretical welding temperatures were compared to temperatures obtained experimentally (Table 4.5) and the margin of error was calculated. The corrected temperature values and margin of error for case 1 are displayed in Table 4.15. The average margin of error for case 1 is 8.2%.

The results for temperature correction under case 2 are shown in Table 4.16. The average margin of error between all the tools for case 2 is 6.4%. The temperature data

Table 4.14: Temperature correction coefficients for cases 1, 2, and 3 (Equation 3.19 and Equation 3.20)

Correction coefficient	Case 1	Case 2	Case 3
C1	0.78388		
C2	0.36710		
C3	-1.5393		
C4	0.85394		
C5		0.46644	551.16
C6		0.00046573	32.300
C7		-446.94	-1.0132
C8		29.224	-46.090
C9		-23.890	-593.16
C10		0.85752	-1.2709
Error	0.54	0.56	0.0013

Table 4.15: Corrected tool pin temperature measurements - Case 1 (Equation 3.19)

Tool i.d.	$\widehat{T}_s^{+}$ (°C)	$\overline{T}$ (°C)	Margin of error (%)
A	485.2	395.1	18.6
B	486.6	445.2	8.5
C	504	488.6	3.1
D	486.6	435.1	10.6
E	486.6	487.9	0.3
F	485.2	422.4	12.9
G	486.6	453.7	6.8
H	502	457.7	8.8
I	486.6	439.1	9.8
J	486.6	474.6	2.5

collected at the CCWJ was added to an existing FSW database of experimental and theoretical temperature results compiled by Tello (Tello, 2008). The experimental and theoretical temperatures were plotted against each other to see how well the values compared against each other (Figure 4.5 and Figure 4.6). Data points near the 1:1 dashed line indicate a better fit between the predicted welding temperature and the experimentally measured one. The data used to generate Figure 4.5 are listed in the appendix (Table A-12, Table A-13, and Table A-14).

Table 4.16: Corrected tool pin temperature measurements - Case 2 (Equation 3.20)

Tool i.d.	$\widehat{T}_s^+$ (°C)	$\overline{T}$ (°C)	Margin of error (%)
A	457.9	395.1	13.7
B	480.5	445.2	7.3
C	498.9	488.6	2.1
D	480.5	435.1	9.4
E	480.4	487.9	1.6
F	457.9	422.4	7.8
G	480.5	453.7	5.6
H	493.1	457.7	7.2
I	480.5	439.1	8.6
J	480.4	474.6	1.2

Case 3 accounts for $(\frac{b-a}{\widehat{\delta}})$ and $\frac{\widehat{\delta}}{a}$, but only for experiments ran in-house at the CCWJ. The results for temperature correction under case 3 are shown in Table 4.17. The average margin of error between all the tools for case 3 is 1.4%.
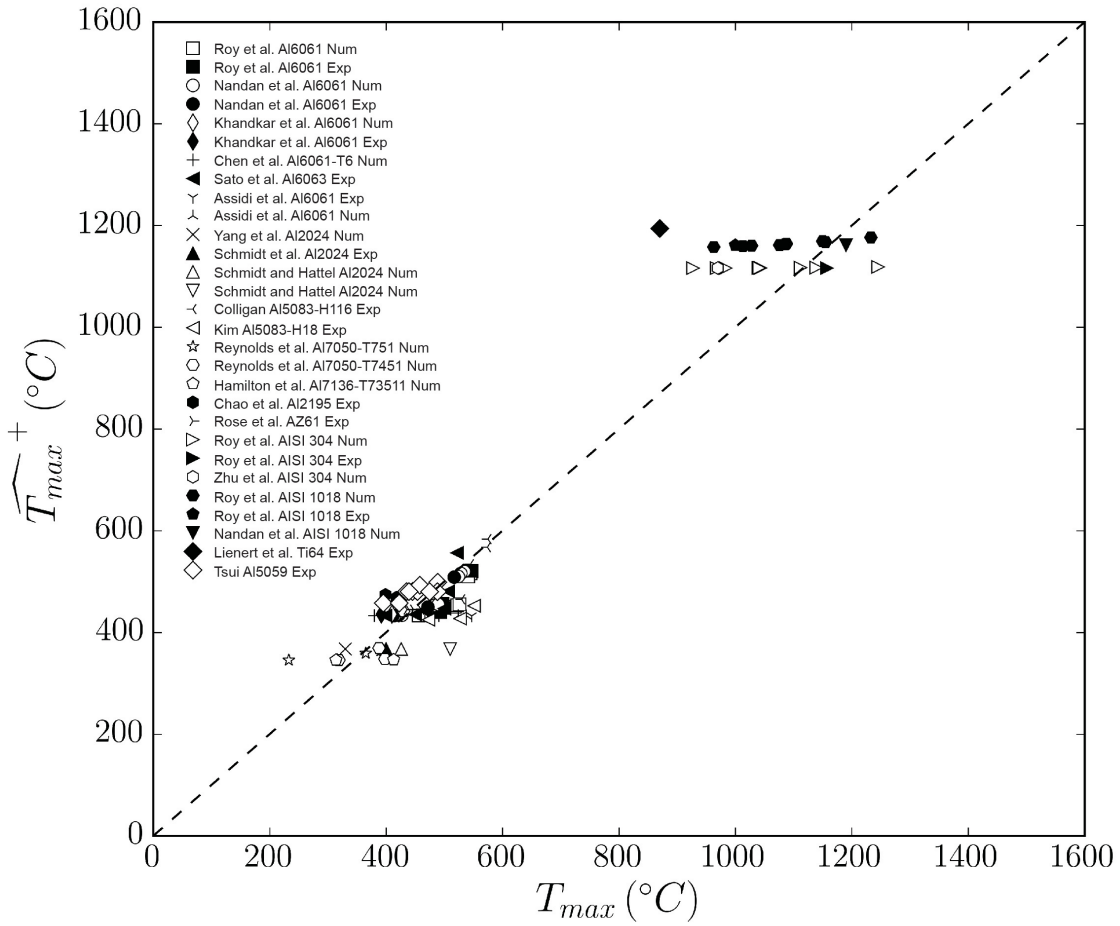
Figure 4.5: Comparison between experimentally measured temperature (T_{max}) and theoretical predictions ($\widehat{T_{max}}^{+}$) during FSW (data used listed in Table A-12, Table A-13, and Table A-14)
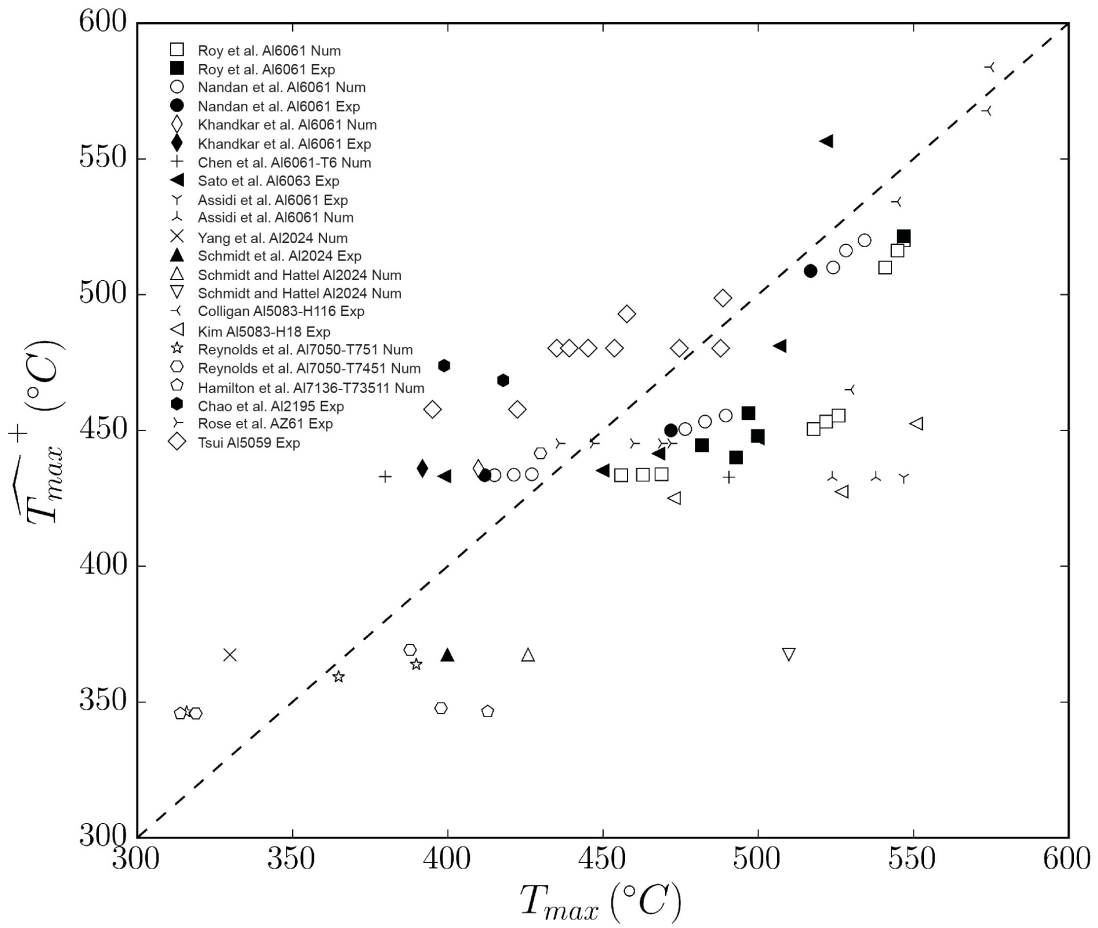
Figure 4.6: Magnified region of aluminum data from Figure 4.5

Table 4.17: Corrected tool pin temperature measurements - Case 3 (Equation 3.20)

Tool i.d.	$\widehat{T}_s^+$ (°C)	$\overline{T}$ (°C)	Margin of error (%)
A	410.3	395.1	3.7
B	456.9	445.2	2.6
C	489.4	488.6	0.2
D	435.4	435.1	0.1
E	478.6	487.9	1.9
F	410.3	422.4	2.9
G	456.9	453.7	0.7
H	458.6	457.7	0.2
I	435.4	439.1	0.8
J	478.6	474.6	0.8

4.2 Force and torque measurements during friction stir welding

4.2.1 Force and torque measurements

Force and torque measurements during FSW were done using a JR3 load cell following the methods described in section 3.3. Similarly to the thermocouple data section, various portions of the welding process can be identified on the force data collected from the JR3 load cell. These portions include the tool plunge, weld travel, steady state, running over thermocouples embedded into the substrate, and tool extraction. These are summarized in Figure 4.7 where each identified portion of the weld process are labeled on each force/torque graph.

Multiple welds were performed with each FSW tool using the JR3 load cell. The forces in the x-y-z direction and the tool pin torque along the z-axis were recorded. The results of each experiment for the FSW tools with smooth pins (A through E) are in Table 4.18, and the results for the FSW tools with threaded pins (F through J) are in
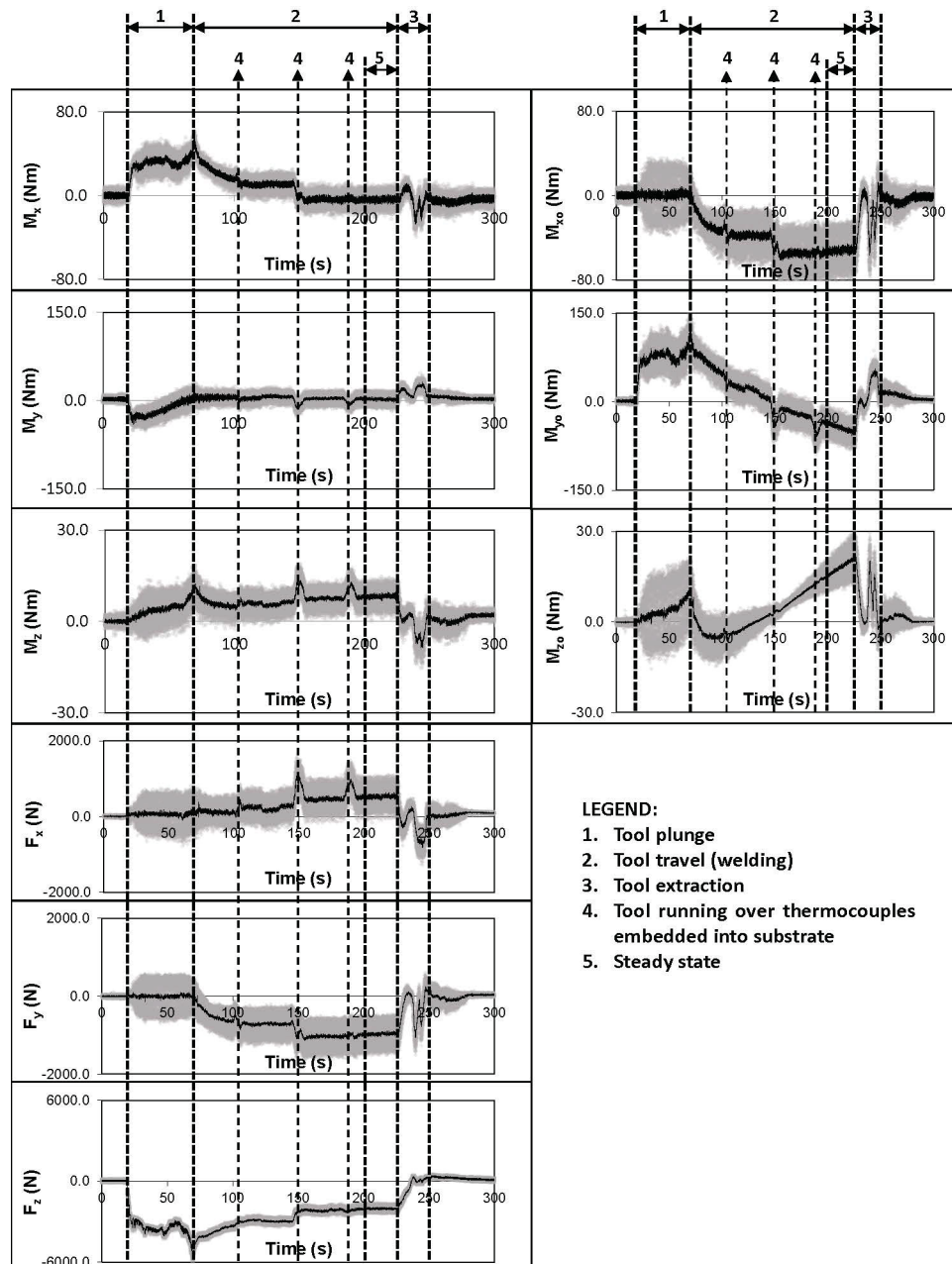
Figure 4.7: Force and torque profile (tool G) during friction stir welding

Table 4.19. The average force and torque values for each tool were calculated and are summarized in Table 4.20. Tools C and F only have one measurement due to tool damage preventing further use. Tool D produced unusually high force and torque readings due to tool insertion depth being too great (human error). The mistakes with tool D were made evident not only from load cell readings but from the visual appearance of the weld itself which had excessive material flashing caused by the tool shoulder gouging the substrate material (Figure 4.8).

Table 4.18: Force and torque measurements during FSW for tools A through E

Tool i.d.	F_x (N)	F_y (N)	F_z (N)	x_o (mm)	y_o (mm)	M_z (N-m)
A	60	540	-600	42	16	5.5
	5	475	-640	39	17	6
	240	650	-775	80	-9	8
	50	600	-750	36	-6	4
	275	675	-700	-4	-9	2
	350	550	-1000	80	13	10
B	250	950	-800	36	15	7
	100	975	-800	24	23	5
C	-	-	-1600	65	-7	10
D	800	1100	-2200	80	-34	11
	650	1200	-1800	31	-35	12
	200	1000	-2200	-10	-39	12
	950	1300	-2100	73	-13	10
	500	1300	-2200	24	-13	8
E	600	1050	-4200	-18	-6	7
	950	1400	-3100	77	12	9
	550	1500	-4200	35	15	5

The 95% confidence interval was tabulated for the torque measurements and the results are shown in Table 4.21. Tools C and F which only have one data points do not have a confidence interval.

Table 4.19: Force and torque measurements during FSW for tools F through J

Tool i.d.	F_x (N)	F_y (N)	F_z (N)	x_o (mm)	y_o (mm)	M_z (N-m)
F	300	80	-1600	-46	0	3.2
G	550	950	-2000	-37	-9	6.5
	950	900	-2900	-47	-5	5
	550	850	-2800	-16	-5	6
	700	1000	-2600	-52	-6	5
	200	875	-2600	-5	-6	6
H	350	1000	-6500	-47.5	-4	13
	550	900	-6400	-50.5	-4	13
	250	800	-5800	-3.5	-3	11
	500	1000	-6000	-47.5	-3	11
	300	800	-5900	-4	-2	14
I	750	700	-2000	-42	-9	8
	550	750	-1200	-30	-14	6
	650	760	-1600	-41	-12	8
	100	400	-1600	-6	-4	5
	600	550	-1400	-41	-9	7
	200	600	-1400	-4	-8	6
J	300	650	-3400	-46	-3	7
	400	700	-4000	-41	-2	6.5
	350	650	-3900	-1.5	-3	8
	400	650	-4000	-42.5	-2	6.5
	400	550	-3800	-1	-2	9

Table 4.20: Average force and torque during FSW for tools A through J

Tool i.d.	F_x average (N)	F_y average (N)	F_z average (N)	M_z average (N-m)
A	195.0	581.7	-744.2	6.7
B	175.0	962.5	-800.0	6.0
C	-	-	-1600.0	10.0
D	620.0	1180.0	-2100.0	10.3
E	700.0	1316.7	-3833.3	8.0
F	300.0	80.0	-1600.0	3.2
G	590.0	915.0	-2580.0	5.7
H	390.0	900.0	-6120.0	12.4
I	475.0	626.7	-1533.3	6.7
J	370.0	640.0	-3820.0	7.4

Figure 4.8: Tool D weld defect - excessive material flashing caused by large tool insertion depth

Table 4.21: Confidence interval (95%) for torque measurements

Tool i.d.	N	$\overline{M}$ (N-m)	S (N-m)	95% C.I.
A	5	6.7	2.3	6.5
B	2	6.0	1.4	18.0
C	1	10.0	0.0	0.0
D	5	10.3	1.7	4.7
E	2	8.0	1.4	18.0
F	1	3.2	0.0	0.0
G	5	5.7	0.7	1.9
H	5	12.4	1.3	3.7
I	6	6.7	1.2	3.1
J	5	7.4	1.1	3.0

4.2.2 Theoretical friction stir welding torque calculations

Using Equation 2.7, the torque during FSW was predicted for tools A through J. The results before applying corrections coefficients are show in Table 4.22, and the variables used for calculations are listed in the appendix (section 6).

Table 4.22: Predicted torque during FSW (Equation 2.7; variables listed in section 6)

Tool i.d.	$\widehat{M}$ (N-m)
A	3.6
B	7.1
C	9.4
D	7.1
E	7.1
F	3.6
G	7.1
H	9.2
I	7.1
J	7.1

Initial adjustment of the predicted torque was done using Equation 2.14 and the results are in Table 4.23. The average margin of error is 31.1%.

Table 4.23: Predicted torque during FSW (Equation 2.14)

Tool i.d.	$\widehat{M}^+$ (N-m)	$\overline{M}$ (N-m)	Margin of error (%)
A	5.7	6.7	17.5
B	11.1	6.0	45.9
C	14.8	10.0	32.4
D	11.1	10.3	7.7
E	11.1	8.0	27.9
F	5.7	3.2	43.9
G	11.1	5.7	48.6
H	14.4	12.4	13.9
I	11.1	6.7	39.9
J	11.1	7.4	33.3

Through experimentation it was found that the shoulder diameter produced a noticeable effect on temperature and torque during welding. The shoulder diameter was accounted for using Equation 3.22, and the correction coefficients were calculated for two different cases. The first case accounted for $\frac{b-a}{\hat{\delta}}$ for all materials that torque data was available, and the second case only considered the experimental data collected in-house at the Canadian Centre for Welding and Joining (CCWJ). The correction coefficients for torque are listed in Table 4.24.

Using the correction coefficients, the torque values from Table 4.22 were adjusted to account for the shoulder diameter. The corrected values and margin of error for case 1 are displayed in Table 4.25. The average margin of error between all ten FSW tools is 24.4%.

The data collected at the CCWJ (corrected from case 1) was added to an existing

Table 4.24: Torque correction coefficients for cases 1 and 2 (Equation 3.22)

Correction coefficient	Case 1	Case 2
C11	1.3393	1.1018
C12	21.748	0.95468
C13	-0.16762	1.0405
Error	2.4	0.63

Table 4.25: Corrected torque measurements - Case 1 (Equation 3.22)

Tool i.d.	$\widehat{M}^+$ (N-m)	$\overline{M}$ (N-m)	Margin of error (%)
A	4.8	6.7	38.5
B	9.4	6.0	36.5
C	12.6	10.0	20.5
D	9.4	10.3	8.5
E	9.4	8.0	15.3
F	4.8	3.2	33.8
G	9.4	5.7	39.7
H	12.4	12.4	0.2
I	9.4	6.7	29.4
J	9.4	7.4	21.7

FSW database of experimental and theoretical torque results compiled by Tello (Tello, 2008). The experimental and theoretical temperatures were plotted against each other to see how well the values compared against each other (Figure 4.9). Data points near the 1:1 dashed line indicate a better fit between the predicted torque and the experimentally measured one. The data used to generate Figure 4.9 are listed in the appendix (Table A-16 and Table A-17).
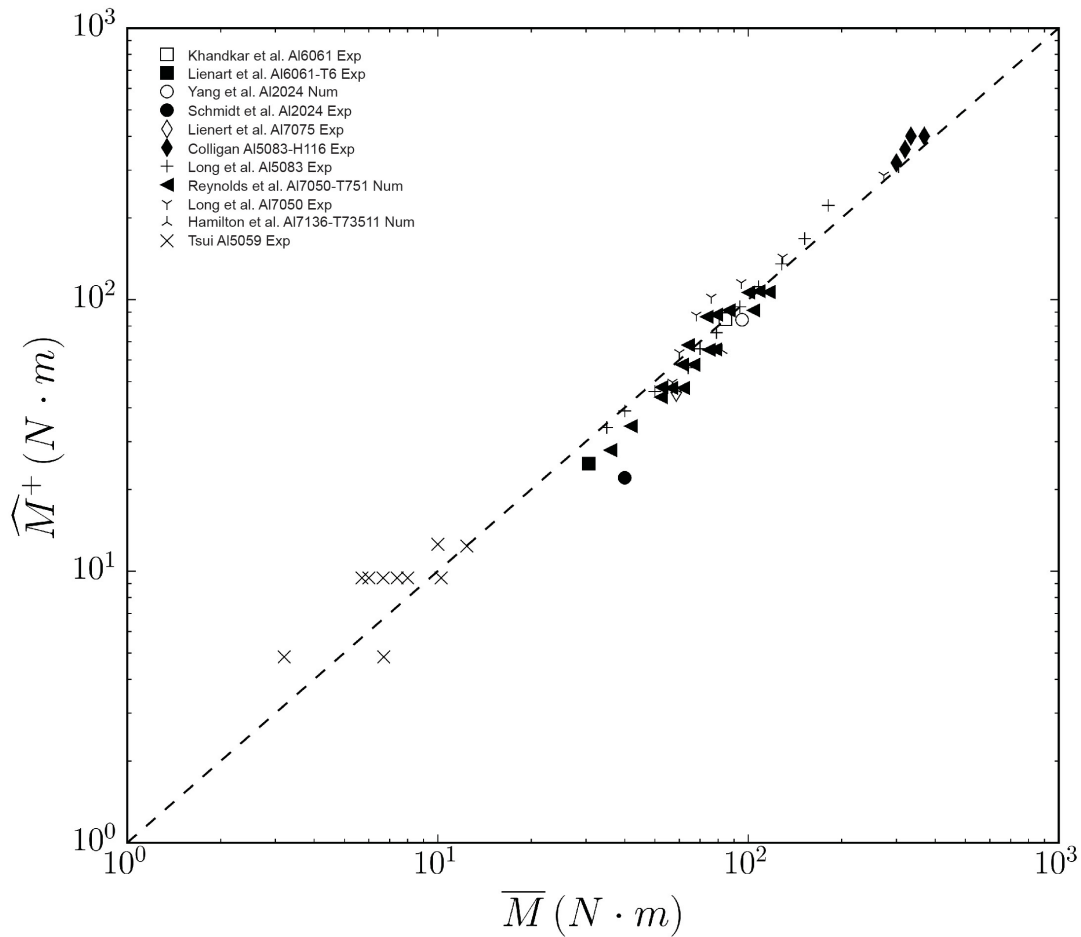
Figure 4.9: Comparison between experimentally measured torque ($\overline{M}$) and theoretical predictions ($\widehat{M}^+$) during FSW (data used listed in Table A-16 and Table A-17)

Case 2 only used the data collected at the CCWJ, and the adjusted values and margin of error are shown in Table 4.26. The average margin of error between all ten FSW tools is 21.6%. Excluding tool A and D whose measured torque was higher due to low welding temperature and excessive tool insertion depth, the average margin of error drops to 14.5%.

Table 4.26: Corrected torque measurements - Case 2 (Equation 3.22)

Tool i.d.	$\widehat{M}^+$ (N-m)	$\overline{M}$ (N-m)	Margin of error (%)
A	4.0	6.7	68.4
B	7.8	6.0	22.8
C	10.3	10.0	3.4
D	7.8	10.3	31.9
E	7.8	8.0	2.9
F	4.0	3.2	19.6
G	7.8	5.7	26.7
H	10.2	12.4	21.8
I	7.8	6.7	14.2
J	7.8	7.4	4.8

Chapter 5

Discussion

The following chapter will analyze the results for temperature, force, and torque measured during welding. Trends observed from the data will be discussed and reasons for the trends will be presented. This will cover:

- Effects of tool geometry on welding temperature

- Comparison of methods for measuring temperature (tool versus substrate)

- Welding temperatures predicted from scaling laws

- Effects of tool geometry on welding force and torque

- Welding torque predicted from scaling laws

5.1   Effects of FSW tool geometry on welding temperature

The calibrated average welding temperatures for the tool pin, tool shoulder, and substrate are summarized in Table 5.1. Analyzing each data point in Table 5.1 is made easier by first looking at how the FSW tools are grouped by geometry. The geometry of

each tool is shown in Table 3.1, and Table 3.2 shows how they are grouped accordingly. Tool groups ABC and FGH are proportionally increasing in size for both the pin and shoulder. Tool groups DBE and IGJ all have the same sized pin with only the shoulder increasing in diameter. Hence, data for tools ABC and FGH will yield information on the effects of increasing overall tool size with regards to welding temperature, and tools DBE and IGJ will yield information on how increasing shoulder diameter will affect welding temperature. Substrate data points for tools C, D, and E are missing because they broke before experiments with the NI USB-6351 data acquisition system was introduced. In the previous section on tool pin and shoulder measurements it was assumed that the maximum welding temperature of tool C would be at least 488.6°C; this value is a conservative estimate and will be referenced when discussing the effects of geometry. The most complete set of temperature data (tool and substrate) is with the threaded tools.

Table 5.1: Corrected pin, shoulder, and substrate temperature measurements during FSW for tools A through J

Tool i.d.	Average pin temperature (°C)	Average shoulder temperature (°C)	Average substrate temperature (°C)
A	395.1	380.0	350.9
B	445.2	400.6	415.8
C	488.6	476.6	-
D	435.1	370.9	-
E	487.9	449.0	-
F	422.4	410.4	383.1
G	453.7	401.8	436.1
H	457.7	405.8	459.2
I	439.1	372.4	427.9
J	474.6	433.3	448.2

5.1.1 Proportionally increasing FSW tool size

The data for tools A, B, and C indicate that as the pin increases in size (length and diameter) the welding temperature will also increase. Tool A, B and C's average pin temperatures were 395.1, 445.2, and 488.6 °C, respectively. The same trend is noted when looking at threaded tools F, G, and H whose average pin temperatures were measured at 422.4, 453.7, and 457.7 °C, respectively. The tools in sets ABC and FGH start small and increase in size proportionally as shown in table Table 3.2. As the tool pin size is increased, it will deform more material during travel and create more frictional heating while it rotates since the contact surface area between the tool and substrate is increased. The overall effect is an increase in welding temperature as the pin size (length and diameter) is increased.

The tool shoulder also generates a significant amount of frictional heating. As the shoulder diameter is increased there is a larger contact surface area between the shoulder and substrate to generate heat, and maximum welding temperature should increase as the heat from the shoulder conducts through the substrate. The average shoulder temperature measurements for tools A, B, and C were 380.0, 400.6, and 476.6 °C, respectively. The interpretation that a larger shoulder will generate more frictional heat is consistent with these results. However, tools F, G, and H do not seem to follow this trend with the smallest shoulder (tool F) measuring at the highest temperature between these three tools. The average shoulder temperature measurements for tools F, G, and H were 410.4, 401.8, and 405.8 °C, respectively. The deviation from expected results may be caused by thermocouple position within the FSW tool, the additional rotation speed used for tool F, or by experimental error from the plunge depth of the tool during welding. The plunge depth of the tool is directly related to the downward force exerted between the FSW tool

and substrate. A deeper plunge depth means greater downward force which will generate more frictional heating. While the heat produced at the shoulder is likely to affect the steady state welding temperature at the pin, its effect is of small enough magnitude that the pin geometry is more relevant on changing the actual welding temperature as evident by the results.

It should be noted that for tools A and F, the rotational speed of the spindle was increased from 1225 to 1723 RPM. This was done to increase overall welding temperature to reduce tool stress. In previous trials, welds performed at 1225 RPM caused tools A and F to break immediately after weld travel was initiated. Despite using a higher rotational speed, the temperature data collected still lies within a valid and comparable range between the other FSW tools.

5.1.2   Increasing tool shoulder diameter

Tool sets DBE and IGJ all have a 4 mm diameter pin and a 5.3 mm pin length. The only changes between each tool is the shoulder diameter (Table 3.2), all welding parameters were kept constant between each tool. As stated previously, a larger tool shoulder should generate more frictional heating during welding which should increase the steady state welding temperature at the tool pin. The average shoulder temperatures for tools D, B, and E were 370.9, 400.6, and 449.0 °C, respectively. The average shoulder temperatures for tools I, G, and J were 372.4, 401.8, and 433.3 °C, respectively. The results for tool sets DBE and IGJ are consistent with the idea that larger shoulders produce more heat.

The average pin temperatures for tools D, B, and E were 435.1, 430.5, and 487.9 °C,

respectively. It was expected that tool D would have a lower welding temperature than tool B because shoulder diameter and temperature were lower. Analyzing the force data for tool D indicated excessive tool insertion resulting in higher welding temperatures which overshadowed temperature changes caused by geometry changes. The average pin temperature for the threaded tools I, G, and J were 406.5, 453.7, and 474.6 °C, respectively. Excluding tool D whose result is an outlier caused by excessive tool plunge, tools B, E, I, G, and J show that the increase in shoulder diameter produces more frictional heating which resulted in an increase in steady state welding temperature.

5.1.3   Tool pin surface (smooth vs. threaded)

The type of pin surface also had bearing on the steady state welding temperature. It should be noted that the FSW tools with threaded pins (tools F, G, H, I, and J) generally produced higher welding temperatures than their smooth cylindrical counterpart (tools A, B, C, D, and E). This was due to the additional material flow caused by the threads which will push material downwards and produce more heat from mechanical deformation of the substrate (Gerlich et al., 2006; Gordon, 2010).

The effects of pin surface on steady state welding temperature are best shown by tool pairs BG and DI. The measured shoulder temperature of these pairs are very close in value, so the only variable between the two tools that would further influence welding temperature would be the pin threading. The geometry and welding parameters for tools B and G were the same, and the average shoulder temperatures were 400.6 and 401.8 °C, respectively. The average pin temperature of tool B and G were 445.2 and 453.7 °C, respectively, meaning the additional 8.5 °Cof tool G was likely caused by the pin thread-

ing. The geometry and welding parameters for tools D and I were also the same, and their average shoulder temperatures were 370.9 and 372.4 °C, respectively. The average pin temperatures of tool D and I were 435.1 and 439.1 °C, respectively; the addition of threading to the pin surface of tool I resulted in a small increase (4 °C) in measured welding temperature.

Comparing tools E and J, the trend that pin threading causes an increase in steady state welding temperature is not observed. This is due to the influence of the shoulder overshadowing the effects of threads. The average shoulder temperature of tool E and J are 449.0 and 433.3 °C, respectively. This difference of 15.7 °Ccaused the tool E pin temperature to be 13.3 degrees higher than tool J, despite tool J having a threaded pin. Something similar is observed when analyzing tools A and F. Tool F exhibited a measured shoulder temperature 30.4 degrees higher than tool A's average shoulder temperature. This difference caused tool F's measured pin temperature to be 27.3 degrees higher than tool A's pin temperature which is far greater than what would have been caused by pin threading alone. The effect of pin threading on tool F is likely to have added a few degrees Celsius compared to tool A, but was not noticeable because of the large heat difference at the shoulder.

5.2   Temperature measured from the FSW tool compared to measuring from the substrate

The intention of adapting a temperature data acquisition system (MSR 145B) to spin with the FSW tool was to be able to accurately take temperature readings directly from

the surface of the pin and shoulder throughout the entire weld. The advantage of thermocouples embedded into the tool is that a steady state temperature can be recorded and measured. Due to the process of friction stir welding, it is typically much easier to embed thermocouples into the substrate and weld over top of them to measure maximum welding temperature. The position of the thermocouple bead inside the substrate is only as accurate as the size and position of the hole that is drilled into it. The aluminum plates used at the CCWJ had holes drilled with a 1 mm drill bit, so the thermocouple's final position could vary up to ± 0.5 mm from side to side once cemented in.

By running data acquisition systems at the FSW tool and the substrate simultaneously, the data can be compared directly and more definitive conclusions can be drawn about the accuracy and trends. It was assumed that tool pin measurements would be equal to substrate measurements (i.e. tool and substrate measurements would follow an approximate 1:1 ratio). However, the majority of the data points do not lie near the 1:1 line (Figure 4.2). The position of the data points relative to being above or below the dotted line give some information of the ability of the data acquisition system. Since the majority of the recorded data lies below the dotted line, this means that the MSR 145B data acquisition system was recording higher welding temperatures than the substrate with embedded thermocouples. This would indicate that the thermocouples embedded into the FSW tool provide a more accurate representation of the true welding temperature during friction stir welding, and that substrate thermocouples were measuring low. A possible reason the substrate thermocouples recorded lower temperatures may be that the position of the thermocouple shifted slightly as the approaching FSW tool deformed adjacent material. The deformed material would push the thermocouple out of position and direct contact between the FSW tool and substrate thermocouple would be missed resulting in a low measurement (Lienert et al., 2003). The duration of the traveling tool

pin contacting the embedded substrate thermocouple is very short, and the low temperature measurements may have also been caused by insufficient contact time between the tool and the substrate thermocouples.

Interpreting the data from Figure 4.2 based on the tool groups also yields information by looking at the angle of the slopes they form. A slope greater than 1 would indicate that the changes in FSW tool geometry cause a greater temperature change when measured at the substrate. A slope that is close to parallel to the 1:1 dotted line would indicate that the change in geometry has equal effects on the temperatures measured from the tool pin and substrate. A slope less than 1 indicates that the temperature measured at the tool pin is more sensitive to changes in FSW tool geometry. The actual value of the slope and equation of line is not considered because the line it forms is simply a visual reference to show sensitivity of temperature measurements.

The first set of tools, tools FGH, are the threaded counterparts to tools ABC (Figure 4.3). The slope that points F, G, and H form are also greater than 1 which means that the changes in geometry were felt more when measured from the substrate. The trend that follows is that as the FSW tool pin gets larger, the substrate temperature measurements begin to better match with temperatures measured directly from the tool pin. A larger pin is likely to make proper contact with thermocouples embedded into the substrate. Hence, the low temperature measurements observed for the smaller FSW tools is caused by deformed material adjacent to the pin pushing the substrate's thermocouples out of position during welding.

The second set, tools IGJ, are the threaded counterpart to tools DBE (Figure 4.4). The slope that is formed by points I, G, and J is less than 1 indicating that changes in

welding temperature caused by shoulder geometry are more noticeable when measured from the tool as opposed to the substrate. Reasons for substrate temperature measurements being unable to capture the effects of shoulder geometry are: shifting thermocouple positions during welding (lowering the accuracy of the measured welding temperature), and contact time between the tool and substrate thermocouple being too short to reach steady state welding temperature.

Regression analysis was performed to find the relative influence of pin and shoulder diameter on $\Delta T_{experimental}$, and the results are shown in Table 4.12. The coefficient X_1 is the intercept and represents the difference between temperature measured from the pin and substrate for tools whose geometry falls on the median within the tool matrix (tools B and G). The second coefficient, X_2, has a value of -26.5 and is the relative weight of pin diameter. For tools whose pin diameter is smaller than the median size (tools A and F), X_2 becomes positive and $\Delta T_{experimental}$ will become larger; Tools C and H whose pin diameter is larger than the median size will cause X_2 to remain negative and $\Delta T_{experimental}$ will decrease. The results for X_2 highlight the problem with measuring temperature from the substrate, because thermocouples will often shift as material is deformed around them causing inaccuracies with measurements. Tools with small pin diameter likely did not make proper contact with substrate thermocouples which resulted in a larger $\Delta T_{experimental}$.

The magnitude of X_3 is one less than X_2 so shoulder diameter does not have as much influence as the pin. Tools whose shoulder diameter is smaller than the median size (tools A, D, F, and I) cause X_3 to be negative which decreases the value of $\Delta T_{experimental}$. Tools with larger shoulder diameter (tools C, E, H, and J) will cause X_3 to have a positive value and make $\Delta T_{experimental}$ larger. The results for X_3 come to the same conclusion as

analysis of slope in Figure 4.4 where it was found that measuring temperature from the substrate did not capture the full effects of tool shoulder diameter.

In previous work done by Tello, it was determined that the size of the tool shoulder had no influence on calculating the maximum temperature during FSW. This was based on a graph comparing a ratio of experimental and theoretical welding temperatures against $(b-a)/\hat{\delta}$. The value of $(b-a)/\hat{\delta}$ did not visibly affect the ratio of experimental to theoretical welding temperature, and a conclusion was made that predicted welding temperatures were independent of shoulder diameter (Tello, 2008). However, in the previous section discussing effects of geometry on the welding temperature it was shown that the size of the shoulder does in fact have a measurable effect on the maximum welding temperature. This contradiction in findings might be explained from what was found analyzing Figure 4.4, where the effects of the shoulder were less noticeable when measuring temperature from the substrate compared to taking temperature directly from the FSW tool. The welding temperature data compiled by Tello were measured almost exclusively from the substrate, so when comparisons were made between the temperatures predicted from scaling equations and experimental values the shoulder geometry was deemed non-relevant.

5.3   Welding temperatures predicted from scaling laws

In early iterations of using Equation 2.13 to predict the maximum welding temperature during FSW, the correction function only considered the $\hat{\delta}/a$ term. As such, the tool shoulder diameter, b, was not factored into the calculations of theoretical welding temperature at all. However, recent experiments using thermocouples embedded into the FSW

tool pin and shoulder gave indication that the shoulder has a relevant effect on maximum welding temperature. Subsequent use of the correction function was changed to include the $(b - a)/\hat{\delta}$ term (Equation 3.20), and the correction coefficients were tabulated for three different cases Table 4.14.

Case 1 (Table 4.15) was calculated using the data compiled by Tello and the data collected at the CCWJ. Introducing experimental results collected at the CCWJ into the database compiled by Tello causes slight bias because correction coefficients are being tabulated based on the data that is used to test the model (i.e. the model is being fit to the experimental data). However, this is done to help refine the model by providing more data as a whole. The correction coefficients are already calculated using published temperature data from numerous authors for various metals. Adding the data for Al5059 into the database used to calculate the correction coefficients helps produce a more robust model by refining it further with more experimental data. Case 1 accounts for instances where Equation 2.3 is not satisfied by accounting for the $\hat{\delta}/a$ term in the correction function. Among the three cases, case 1 had the largest average margin of error at 8.2%. The 'margin of error' refers to the percentage difference between experimentally measured temperature and the theoretical welding temperature predicted by scaling laws. The individual tools with the largest margins of error were also the tools with the smallest shoulder diameters (9 mm). Tools A, F, D, and I had margins of error of 18.6%, 12.9%, 10.6%, and 9.8%, respectively. Looking at the tool group ABC, the margin of error decreases as the tool size increases. Similarly, with tool group DBE the margin of error decreases as the shoulder diameter increases. Tools with threaded pin surfaces (tools F through J) follow the same trend; as the shoulder diameter increases, the margin of error lowers meaning the predicted welding temperatures better match experimental values. Without accounting for the shoulder diameter in the correction

function there appears to be an ideal tool shoulder size which yields the best match with predicted welding temperature.

Case 2 (Table 4.16) was calculated using the data compiled by Tello and the data collected at the CCWJ. Introducing experimental results collected at the CCWJ into the database compiled by Tello causes slight bias because correction coefficients are being tabulated based on the data that is used to test the model (i.e. the model is being fit to the experimental data). However, this is done to help refine the model by providing more data as a whole. The correction coefficients are already calculated using published temperature data from numerous authors for various metals. Adding the data for Al5059 into the database used to calculate the correction coefficients helps produce a more robust model by refining it further with more experimental data. Case 2 accounts for instances where Equation 2.3 and Equation 2.4 are not satisfied by including $\hat{\delta}/a$ and $(b-a)/\hat{\delta}$ in the correction function. The inclusion of b within the correction function also means that the effects of the shoulder diameter on welding temperature will be captured. The average margin of error for case 2 is 6.4% which is an improvement from case 1. The results of the theoretical temperature calibrations are not perfect though, and despite accounting for the shoulder with the $(b-a)/\hat{\delta}$ term the trends between tool geometry and the predicted welding temperature remain exactly the same as case 1. For tool groups ABC and DBE, the margin of error decreases as the shoulder diameter increases. The tool groups with threaded pins, FGH and IGJ, also continue to have lower margins of error as tool shoulder increases. Including the $(b-a)/\hat{\delta}$ term in the correction function has a noticeable improvement, but the predicted welding temperatures are still the least accurate when shoulder diameter is small. It should be noted that $\hat{\delta}/a$ is the dominant factor compared to $(b-a)/\hat{\delta}$ (i.e. a small change in $\hat{\delta}/a$ will affect the predicted welding temperature more than a small change in $(b-a)/\hat{\delta}$). The majority of the data used

to tabulate the correction coefficients were temperatures measured from the substrate, which fails to capture the full effect of the shoulder diameter on welding temperature. It is possible that the $(b-a)/\hat{\delta}$ term is less dominant because of this.

Case 3 (Table 4.17) was calculated using only the data collected at the CCWJ. Case 3 accounts for instances where Equation 2.3 and Equation 2.4 are not satisfied by including $\hat{\delta}/a$ and $(b-a)/\hat{\delta}$ in the correction function. The inclusion of b within the correction function also means that the effects of the shoulder diameter on welding temperature will be captured. The average margin of error is the lowest at 1.4% compared to cases 1 and 2. However, case 3 contains significant bias because the correction coefficients are being fitted to a small subset of data, and they only apply for a single material (Al5059). The purpose of fitting a smaller set of data is to demonstrate that correction coefficients can be tabulated for a single material to be used as an engineering tool for preliminary weld design. The results of case 3 show a very good fit between theoretical temperature and experimental values, and it is likely that correction coefficients can be tabulated for other single materials as well.

5.4 Effects of FSW tool geometry on welding force and torque

Force required for friction stir welding is largely dependent on the overall size of the FSW tool (pin length, pin diameter, and shoulder diameter). As the FSW tool pin and shoulder increases in diameter, the area of contact between the pin/shoulder and substrate increases and more torque is required to spin the tool at the desired rotation speed

during welding. The greater area of contact between tool and substrate also means more downward force (F_z) is required to plunge into the substrate material, and the more lateral force (F_x and F_y) is needed to move through it. The insertion depth of the pin (tool plunge depth) will also influence the forces applied during welding. If the plunge depth is too shallow, the shoulder will have improper contact with the substrate and less force will be measured during welding. If the insertion depth is too deep, the shoulder will begin to gouge excess substrate resulting in additional force being required to push the tool.

Forces along the x-axis and y-axis will also vary based on welding parameters such as travel speed and how fast the FSW tool is rotating. The faster the tool travels during welding the more force in the x-direction is required to push through the substrate. Rotation direction will dictate whether the force along the y-axis is positive or negative; the direction of the force perpendicular to the travel direction on the advancing side of the FSW tool was the force measured on the y-axis from the load cell. Rotation speed will also have an effect on the force in the y-direction. The faster the tool rotation, the higher the welding temperature will be due to friction. As the welding temperature increases the substrate will become softer and measured force along the y-axis decreases.

5.4.1   Force along the x-axis

The welding parameters were kept constant between all the FSW tool (15 mm/min travel and 1225 RPM) with the exception of tools A and F where the rotational speed was increased to 1723 RPM. Although it was expected that as the overall tool geometry increased (pin length/diameter and shoulder diameter) the force required to move the tool through the substrate would also increase, this was not observed. Tools A, B and

C (ABC) increase in size proportional to each other (Table 3.2); force along the x-axis should be smallest for tool A, increase for tool B, and tool C should have the highest F_x. However, experimental F_x for tool A (195.0 N) is larger than tool B (175.0 N). The reason why tool A experiences higher force along the x-axis is because of its low welding temperature. A lower welding temperature makes the material around the tool pin difficult to deform which results in additional force being needed to push through it. Tool C was damaged before proper force measurements could be collected for it. Tools D, B, and E (DBE) share the same pin geometry, but the shoulder increases in diameter from tool B to D to E (Table 3.2). As the shoulder diameter increases the force along the x-axis should also increase due to the added contact surface area between the tool shoulder and substrate. Hence, F_x for tool D should be the smallest, followed by tool B which should be higher, and then tool E having the highest value of F_x. This trend was not observed, with tool B having the lowest F_x (175.0 N), followed by tool D (620.0 N), and then tool E (700.0 N). The cause for tool D having a much larger F_x value is due to excessive downward force, F_z, caused by too much tool plunge. Tool insertion depth that goes too far into the substrate will begin to gouge extra material with the shoulder causing force along the travel direction (x-axis) to be greater.

Tools A through E each have smooth cylindrical pins; The threaded pin counterparts are tools F though J. Tools F, G, and H (FGH) mirror the geometry of tools ABC. Force along the x-axis should be smallest for tool F, followed by a higher value for tool G, and highest F_x for tool H. From experiments, tool F had the smallest F_x (300.0 N) followed by tool G (590.0 N), but then the F_x decreases for tool H (390.0 N). Tools I, G, and J (IGJ) mirror the geometry of tools DBE so the force along the x-axis should increase from tool I to G to J. The measured F_x for tool I (475.0 N) and tool G (590.0 N) follow the expected trend, but tool J had the lowest F_x value with 370.0 N. The low F_x results

for tool H and J were initially thought to have been due to insufficient tool insertion depth, but F_z values were adequate in comparison to the other tools. The likely cause for a reduction in F_x is related to welding temperature and the threading along the pin surface. Tool H and J both yielded higher welding temperatures which means material deformation at the shear layer becomes easier resulting in a reduction in F_x during welding.

5.4.2 Force along the y-axis

A relation between FSW tool geometry and force along the y-axis should also exist, similar to the x-axis. As tool geometry increases, the force along the y-axis should also increase due to a larger contact area between the tool and the substrate. Tools A and B follow the expected trend with tool A measuring at 581.7 N and tool B measuring at 962.5 N. Within tool group DBE, tool B (962.5 N) and tool E (1316.7 N) follow the trend that a larger shoulder diameter produces more force along the y-axis. However, tool D's F_y result (1180 N) is larger than tool B's F_y (962.5 N) despite being smaller in size. This is likely caused by too much tool insertion as observed from tool D's large F_z value. Tool insertion depth that goes too far into the substrate will cause measured torque to increase due to the additional pressure between the tool and substrate. Since force along the y-axis is caused by the rotation of the tool pushing in a direction perpendicular to travel direction, an increase in torque will cause force along the y-axis to increase as well.

For tool group FGH, tools F and G follow the expected trend with tool F having the smaller F_y (80 N) and tool G having a larger F_y (915 N). Tool H, the largest tool from set FGH, has an F_y (900 N) that is less than tool G which does not follow the trend. The reduction in F_y for tool H is likely due to its higher welding temperature. Tool F's F_y

value is also quite low compared to tool G. Only a single experiment was managed with tool F before the tool was damaged beyond use so its low F_y measurement may just be an outlier. For tool set IGJ, tool J's F_y (640 N) is almost as low as tool I (626.7 N) and is lower than tool G's F_y (915 N) which does not follow the expected trend from geometry. Similar to tool H, tool J's low F_y is likely due to its higher welding temperature. The increased welding temperature softened material around the pin and caused a reduction in force along the y-axis.

5.4.3   Force and torque along the z-axis

Tool plunge depth is directly related to the downward force applied along the z-axis during welding (F_z). The deeper the plunge depth, the higher the measured F_z should be. The size of the FSW tool will also affect the value of F_z. The larger the tool pin and shoulder diameter are the more downward force is required to plunge into the substrate, because there is an increase in contact surface area between the tool and the substrate. Torque along the z-axis is directly related to F_z since the FSW tool is being pressed into the substrate as it rotates (i.e. a larger F_z will result in a larger value of torque). During experiments, rotation speed was kept constant for all of the different FSW tools (with the exception of tool A and F), so the only factors affecting torque would be F_z and tool geometry. Hence, the tool sets ABC, DBE, FGH, and IGJ can be analyzed to observe if the measured force and torque along the z-axis follows the trends expected from geometry.

Looking at tool set ABC, the measured values of F_z follow the expected trend with tool A measuring at -744 N, tool B measuring -800 N, and tool C requiring the most force at -1600 N. However, torque measurements do not quite follow the same trend with tool

B's M_z (6.0 N-m) measuring slightly lower than tool A (6.7 N-m). A possible reason for the increased torque for the smaller FSW tool is a lower steady state welding temperature. Tool A's average welding temperature was 395 °Cwhereas the welding temperature for tool B was 445 °C. A colder weld will put more stress on the FSW tool as the substrate is more difficult to deform and an increase in torque will be observed.

Within tool group DBE, tool D should have the lowest F_z and M_z, tool B should be in the middle, and tool E should have the highest F_z and M_z. This trend was not observed from the experimental results. Tool D's F_z (-2100 N) and M_z (10.3 N-m) were much greater than tool B's F_z (-800 N) and M_z (6 N-m). These unusual results may be attributed to human error since plunge depth needed to be manually adjusted during welding. In the previous section, instances where F_x and F_y for tool D were inconsistent with what was expected from tool geometry may also be explained by improper tool insertion into the substrate. For example, tool D's large F_z (-2100 N) resulted in larger than expected values of F_x (620 N) and F_y (1180 N). This demonstrates that the effects of a large F_z can overshadow the results caused by different tool geometry.

For the threaded tool set FGH, the results were as expected from geometry. Tool F had the smallest F_z (-1600 N) and M_z (3.2 N-m), tool G was in the middle (F_z of -2580 N and M_z of 5.7 N-m), and tool H has the largest F_z (-6120 N) and M_z (12.4 N-m). The previous observation of the smaller FSW tools experiencing more torque due to having a lower welding temperature was not seen for tool F because welding temperature was sufficient enough to overcome this. For threaded tool set IGJ, the F_z values are as expected due to geometry. Tool I with the smallest shoulder of the group also has the smallest F_z at -1533 N, tool G with medium shoulder has an F_z of -2580 N, and tool J with the largest shoulder has the highest F_z with -3820 N. Tool I has a slightly higher

M_z (6.7 N-m) than tool G (M_z of 5.7 N-m). The cause of tool I's higher torque value may be related to lower welding temperature; Tool I's average welding temperature was 439 °Ccompared to tool G's temperature of 454 °C.

5.5   Welding torque predicted from scaling laws

Using Equation 2.14 brings the calculated values of torque closer to the measured values, but the margin of error is still quite large for some of the tools and ranges from 7.7% up to 48.6%. The average margin of error for all ten FSW tools using Equation 2.14 is 31.1%. The correction coefficient, C_1, does not take into account the size of the shoulder, because it was concluded that torque had no dependence on it (Tello, 2008). Having used Equation 2.14 first, analyzing the results based on tool groups ABC, DBE, FGH, and IGJ did not present any obvious correlations. However, comparing the tools individually established possible trends between the predicted torque values and pin length, pin diameter, and shoulder diameter.

Looking first at the effect of overall FSW tool size, it was observed that the margin of error decreases from tool B to C and from tool G to H. That is, the predicted value of torque for tools C and H were more accurate. The margin of error for tool C improves by 13.5% over tool B, and tool H improves by 34.7% compared to tool G. There is also a decrease in margin of error within tool set DBE and IGJ as shoulder diameter increases. Tool E's error decreases by 18% compared to tool B, and tool J's error decreases by 15.3% compared to tool G. Tools with either larger pin size (length and diameter) or larger shoulder diameter were more accurately predicted for torque than the smaller tools revealing a slight bias using Equation 2.14.

The threaded tools with small shoulder diameter (tools F and I) were among the tools with the highest margin of error. By contrast, the non-threaded tools (A and D) with small shoulder diameter were among the tools with the lowest margin of error. These results are conflicting as tools A and F are expected to match, and tools D and I are expected to match, because they share the same geometry. Tool A's high torque was caused by low welding temperature, and tool D's high torque was caused by excessive tool insertion during welding. This excessive torque matched better with the predicted values resulting in a lower margin of error. The results from tool A and D suggests that the correction coefficient, C_1, in Equation 2.14 is too large, because it over predicts the value of torque with small shoulder diameter.

Results of experiments performed at the CCWJ demonstrate that the shoulder diameter will have noticeable effects on welding temperature and subsequently torque as well. Using Equation 3.22 to account for the shoulder diameter, the torque was calculated based on two different cases. Case 1 for torque (Table 4.25) combines the data compiled by Tello and the data collected at the CCWJ. Introducing experimental results collected at the CCWJ into the database compiled by Tello causes slight bias because correction coefficients are being tabulated based on the data that is used to test the model (i.e. the model is being fit to the experimental data). However, this is done to help refine the model by providing more data as a whole. The correction coefficients are already calculated using published torque data from numerous authors for various metals. Adding the data for Al5059 into the database used to calculate the correction coefficients helps produce a more robust model by refining it further with more experimental data. Case 1 accounts for instances where Equation 2.4 is not satisfied, and the inclusion of b within the correction function also means that the effects of the shoulder diameter on welding

torque will be captured when predicting torque. The average margin of error for torque case 1 is 24.4% which is an improvement over the use of Equation 2.14. Threaded tools F and I which have the smallest shoulder diameter (9 mm) see a significant improvement with their margin of error decreasing by about 10%. Tools A and D end up with a higher margin of error, but this is because their experimental results were abnormal due to low welding temperature (tool A) and excessive tool insertion (tool D). The lowest margin of error continues to be the tools (C, E, H, and J) with the largest shoulder diameter (15 mm) which indicates a slight bias. It is unclear whether this bias is a coincidence from experimental standard deviation or if it comes from the method of measuring with the load cell.

Case 2 for torque (Table 4.26) only uses the data collected at the CCWJ, and similarly to case 1 takes into account the shoulder diameter by including the $(b-a)/\hat{\delta}$ term in the correction function. The average margin of error is 21.6%. The use of a smaller data set for a single material appears to highlight outliers caused by experimental error. Tool A and D have unusual experimental results due to low welding temperature and excessive tool insertion, and subsequently have the highest margin of error. Excluding tool A and D, the average margin of error drops to 14.6%. Predicted torque for tools with small shoulder diameter (F and I) improve significantly. The results for case 2 show a good fit between experimental and theoretical torque. However, it should be noted that case 2 contains significant bias because the correction coefficients are being fitted to a small subset of data, and they only apply for a single material (Al5059). The purpose of fitting a smaller set of data is to demonstrate that correction coefficients can be tabulated for a single material to be used as an instrument for preliminary weld design considerations. The process used to predict torque for Al5059 can be extrapolated to other individual materials provided there is sufficient experimental data to tabulate the correction coeffi-

cients.

Chapter 6

Conclusions

Based on experimental results, the pin diameter has the most dominant effect on steady state welding temperature. A small increase in size (length and diameter) will cause a significant increase in welding temperature, and vice versa. The shoulder has the second largest influence on welding temperature. A larger shoulder will generate more frictional heating and cause the welding temperature to increase. However, a change in pin geometry will likely overshadow the effects of the shoulder. Within the experimental tool matrix, the least dominant factor of geometry is the pin surface type (smooth or threaded). Threading on the pin will deform more material than its smooth counterpart and increase the steady state welding temperature by a few degrees, but both pin and shoulder geometry will greatly eclipse the effects of pin surface type. These results are conclusive for cylindrical shaped tool pins and may not necessarily apply to other novel geometries such as truncated cone pins, whorl pins, MX triflute pins, etc.

When comparing temperatures taken from the FSW tool versus the substrate, the thermocouples embedded into the substrate tend to measure low. The inaccuracy of the substrate thermocouples is caused by two major factors: material deformation during welding pushes the thermocouples away from their initial position, and contact between the FSW tool and substrate thermocouples is sometimes too short for the thermocou-

ples to reach and measure steady state welding temperature. Additionally, the effects of tool shoulder diameter on steady state welding temperature are not fully captured when measuring temperature from the substrate. Hence, the most accurate method of studying and measuring welding temperature during FSW is using thermocouples embedded directly into the tool.

Use of the correction function (Equation 2.10) on predicted FSW welding temperature needs to account for the FSW tool shoulder diameter by including the $(b - a)/\hat{\delta}$ term in addition to $\hat{\delta}/a$. When accounting for both terms (Equation 3.20), the average accuracy of predicted welding temperature increases to 94%. The $\hat{\delta}/a$ term is dominant over $(b - a)/\hat{\delta}$, but there may be some bias to this because the majority of data used to determine the weight of the coefficients was temperature measured from the substrate instead of the FSW tool. The coefficients in the correction function can be tabulated for a single material and yield very good results for predicting welding temperature. However, the quality of the coefficients is highly dependent on having good experimental data to work with.

The FSW tool undergoes a significant amount of force along the x, y, and z-axis during welding. For smooth surface tool pins, a larger pin diameter, a longer pin length, and a larger shoulder diameter all resulted in an increase in force along all three axes. Tools with threaded pins follow the same trend with the exception that once the pin becomes large enough, the presence of threading will reduce forces along the x and y-axis. The reduction of force is from a combination of increased welding temperature and softening of the immediate material near the pin as the threading stirs the metal downwards. Measured torque along the z-axis is strongly correlated with the measured F_z. However, it was observed that FSW tools with small pin and shoulder diameter could not gener-

ate enough heat and tended to experience more torque due to lower welding temperatures.

Early calculations of theoretical welding torque which only considered a single correction coefficient had a tendency to over estimate torque. By accounting for the shoulder diameter in a correction function, the predicted torque (shown by Equation 3.22) improved by 6% on average. Correction coefficients were also tabulated for a single material (Al5059) and predicted values of torque improved by 16% on average. As long as there is sufficient experimental data with which to calculate the correction coefficients focusing on a single material provides the best results.

Comparisons between the experimental results collected at the CCWJ and those predicted by the coupled scaling model show a good fit. The model is a valuable tool that can be used for preliminary weld design only requiring knowledge of the base material properties and welding parameters. The welding temperature can be predicted to ensure a suitable temperature is reached to produce a sound joint. Welding torque can also be predicted and used when considering if a support frame or motor is sufficient for a specific weld.

Bibliography

Amini, S., Amiri, M.R., 2015. Pin axis effects on forces in friction stir welding process. The International Journal of Advanced Manufacturing Technology 78, 1795–1801.

Assidi, M., Fourment, L., Guerdoux, S., Nelson, T., 2010. Friction model for friction stir welding process simulation: Calibrations from welding experiments. International Journal of Machine Tools and Manufacture 50, 143–155. `9809069v1`.

Astarita, A., Squillace, A., Carrino, L., 2014. Experimental Study of the Forces Acting on the Tool in the Friction-Stir Welding of AA 2024 T3 Sheets. Journal of Materials Engineering and Performance 23, 3754–3761.

AZO, 2013. Aluminum 5059 Alloy (UNS A95059). http://www.azom.com/article.aspx?ArticleID=8651.

Bahemmat, P., Haghpanahi, M., Pour Aminaie, I., Papahn, H., 2015. Effect of friction stir welding tool on temperature, applied forces and weld quality. IET Science, Measurement & Technology .

Balasubramanian, N., Gattu, B., Mishra, R.S., 2009. Process forces during friction stir welding of aluminium alloys. Science and Technology of Welding and Joining 14, 141–145.

Buck, G., Langerman, M., 2004. Non-Dimensional Characterization of the friction stir/spot welding process using a simple couette flow model Part I: Constant property Bingham Plastic solution, in: Ghosh, S., Castro, J., Lee, J. (Eds.), American Institute of Physics Conference Series, pp. 1283–1288.

Chao, Y.J., Qi, X., Tang, W., 2003. Heat transfer in friction stir welding - Experimental and numerical studies. Journal Of Manufacturing Science And Engineering-Transactions Of The ASME 125, 138–145.

Chen, C., Kovacevic, R., 2003. Finite element modeling of friction stir welding - thermal and thermomechanical analysis. International Journal of Machine Tools And Manufacture 43, 1319–1326.

Chen, Z.W., Pasang, T., Qi, Y., 2008. Shear flow and formation of Nugget zone during friction stir welding of aluminium alloy 5083-{O}. Material Science and Engineering A 474, 312–316.

Cho, J.H., Boyce, D.E., Dawson, P.R., 2005. Modeling strain hardening and texture evolution in friction stir welding of stainless steel. Materials Science And Engineering A-Structural Materials Properties Microstructure And Processing 398, 146–163.

Colegrove, P.A., Shercliff, H.R., 2003. Experimental and numerical analysis of aluminium alloy 7075-{T}7351 friction stir welds. Science And Technology Of Welding And Joining 8, 360–368.

Colegrove, P.A., Shercliff, H.R., 2004a. Development of Trivex friction stir welding tool Part 1 - two-dimensional flow modelling and experimental validation. Science And Technology Of Welding And Joining 9, 345–351.

Colegrove, P.A., Shercliff, H.R., 2004b. Development of Trivex friction stir welding tool Part 2 - three-dimensional flow modelling. Science And Technology Of Welding And Joining 9, 352–361.

Colligan, K.J., 2007. Relationships Between Process Variables Related to Heat Generation in Friction Stir Welding of Aluminium, in: Mishra, R.S., Mahoney, M.W., Lienert, T.J., Jata, K.V. (Eds.), Friction Stir Welding Processing IV, TMS. pp. 39–54.

De Backer, J., Bolmsjö, G., 2013. Thermoelectric method for temperature measurement in friction stir welding. Science and Technology of Welding and Joining 18, 558–565.

Dong, P., Lu, F., Hong, J.K., Cao, Z., 2001. Coupled thermomechanical analysis of friction stir welding process using simplified models. Science And Technology Of Welding And Joining 6, 281–287.

Fonda, R.W., Bingert, J.F., 2007. Texture variations in an aluminum friction stir weld. Scripta Materialia 57, 1052–1055.

Frigaard, O., Grong, O., Midling, O.T., 2001. A process model for friction stir welding of age hardening aluminum alloys. Metallurgical And Materials Transactions A-Physical Metallurgy And Materials Science 32, 1189–1200.

Gerlich, A., Su, P., North, T.H., 2005. Peak temperatures and microstructures in aluminium and magnesium alloy friction stir spot welds. Science and Technology of Welding and Joining 10, 647–652.

Gerlich, A., Su, P., North, T.H., Bendzsak, G.J., 2006. Energy Generation and Stir Zone Dimensions in Friction Stir Spot Welds. SAE International .

Gordon, S., 2010. Friction stir welding. volume 80.

Guerra, M., Schmidt, C., McClure, J.C., Murr, L.E., Nunes, A.C., 2003. Flow patterns during friction stir welding. Materials Characterization 49, 95–101.

Hamilton, C., Dymek, S., Kalemba, I., Blicharski, M., 2008. Friction stir welding of aluminium 7136-T76511 extrusions. Science and Technology of Welding and Joining 13, 714–720.

Heurtier, P., Jones, M., Desrayaud, C., Driver, J., Montheillet, F., Allehaux, D., 2006. Mechanical and thermal modelling of Friction Stir Welding. Journal of Materials Processing Technology 171, 348–357.

Hussein, S.A., Tahir, A.S.M., Izamshah, R., 2015. Generated forces and heat during the critical stages of friction stir welding and processing. Journal of Mechanical Science and Technology 29, 4319–4328.

Investopedia, 2005. Investopedia - Moving averages. http://www.investopedia.com/terms/m/movingaverage.asp.

Khandkar, M.Z.H., Khan, J.A., Reynolds, A.P., 2003. Prediction of temperature distribution and thermal history during friction stir welding: input torque based model. Science And Technology Of Welding And Joining 8, 165–174.

Kim, D., Badarinarayan, H., Kim, J.H., Kim, C., Okamoto, K., Wagoner, R.H., Chung, K., 2010. Numerical simulation of friction stir butt welding process for AA5083-H18 sheets. European Journal of Mechanics, A/Solids 29, 204–215.

Krantz, W.B., 2007. Scaling Analysis in Modeling Transport and Reaction Processes. A Systematic Approach to Model Building and the Art of Approximation. John Wiley & Sons, INC.

Lienert, T.J., 2007. Microstructures and Mechanical Properties of Friction Stir Welds in Titanium Alloys, in: Mishra, R., Mahoney, M. (Eds.), Friction Stir Welding and Processing. ASM International. chapter 7, pp. 123–154.

Lienert, T.J., Stellwag, W.E., Shao, H., 2000. Determination of load, torque, and tool temperatures during friction stir welding of aluminum alloys. Summary Report SR0019. EWI.

Lienert, T.J., W. L. Stell, J., Grimmett, B.B., Warke, R.W., 2003. Friction Stir Welding Studies on Mild Steel. Welding Journal , 1–9.

Liu, X., Lan, S., Ni, J., 2014. Analysis of process parameters effects on friction stir welding of dissimilar aluminum alloy to advanced high strength steel. Materials & Design 59, 50–62.

Long, T., Tang, W., Reynolds, A.P., 2007. Process response parameter relationships in aluminium friction stir welds. Science and Technology of Welding and Joining 12, 311–317.

McClure, J.C., Tang, W., Murr, L.E., Guo, X., Feng, Z., Gould, J.E., 1998. A Thermal Model of Friction Stir Welding, in: Trends in Welding Research, Pine Mountain, GA. pp. 590–595.

Mehta, K.P., Badheka, V.J., 2015. A Review on Dissimilar Friction Stir Welding of Copper to Aluminum: Process, Properties, and Variants. Materials and Manufacturing Processes 31, 233–254.

Melendez, M., Schmidt, C., Mcclure, J.C., Nunes, a.C., Murr, E., 2005. Tool forces developed during friction stir welding. Technical Report. University of Texas.

Mendez, P.F., 2006. Advanced scaling techniques for the modeling of materials processing, in: Komgoli, F., Reddy, R.G. (Eds.), Sohn International Symposium Advanced Processing of Metals and Materials, TMS. pp. 393–404.

Mendez, P.F., Tello, K.E., Lienert, T.J., 2010. Scaling of coupled heat transfer and plastic deformation around the pin in friction stir welding. Acta Materialia 58, 6012–6026.

Milan Vukčević, Sreten Savićević, Mileta Janjić, N.Š., 2011. Measurement in Friction Stir Welding Process. 15th International Research/Expert Conference , 133–136.

Mishra, R., Ma, Z., 2005. Friction stir welding and processing. Materials Science and Engineering: R: Reports 50, 1–78.

Mohammadi, J., Behnamian, Y., Mostafaei, A., Izadi, H., Saeid, T., Kokabi, A.H., Gerlich, A.P., 2015. Materials Characterization Friction stir welding joint of dissimilar materials between AZ31B magnesium and 6061 aluminum alloys : Microstructure studies and mechanical characterizations. Materials Characterization 101, 189–207.

Nandan, R., Roy, G.G., Debroy, T., 2006a. Numerical simulation of three-dimensional heat transfer and plastic flow during friction stir welding. Metallurgical and Materials Transactions A 37A, 1247–1259.

Nandan, R., Roy, G.G., Lienert, T.J., DebRoy, T., 2006b. Numerical modelling of 3D plastic flow and heat transfer during friction stir welding of stainless steel. Science And Technology Of Welding And Joining 11, 526–537.

Nandan, R., Roy, G.G., Lienert, T.J., Debroy, T., 2007. Three-dimensional heat and material flow during friction stir welding of mild steel. Acta Materialia 55, 883–895.

Reynolds, A.P., Khandkar, Z., Long, T., Tang, W., Khan, J., 2003. Utility of relatively simple models for understanding process parameter effects on {FSW}. Materials Science Forum 426-432, 2959–2964.

Reynolds, A.P., Tang, W., Khandkar, Z., Khan, J.A., Lindner, K., 2005. Relationships between weld parameters, hardness distribution and temperature history in alloy 7050 friction stir welds. Science and Technology of Welding and Joining VOL NO 2 190 10, 190–199.

Rose, A.R., Manisekar, K., Balasubramanian, V., 2012. Influences of welding speed on tensile properties of friction stir welded AZ61A magnesium alloy. Journal of Materials Engineering and Performance 21, 257–265.

Rosenthal, D., 1946. The Theory of Moving Sources of Heat and Its Application to Metal Treatments. Transactions of the A.S.M.E. , 849–866.

Roy, G.G., Nandan, R., DebRoy, T., 2006. Dimensionless correlation to estimate peak temperature during friction stir welding. Science and Technology of Welding and Joining 11, 606–608.

Sato, Y.S., Urata, M., Kokawa, H., 2002. Parameters controlling microstructure and hardness during friction-stir welding of precipitation-hardenable aluminum alloy 6063. Metallurgical and Materials Transactions A 33, 625–635.

Schmidt, H., Hattel, J., 2005a. A local model for the thermomechanical conditions in friction stir welding. Modelling And Simulation In Materials Science And Engineering 13, 77–93.

Schmidt, H., Hattel, J., 2005b. Modelling heat flow around tool probe in friction stir welding. Science And Technology Of Welding And Joining 10, 176–186.

Schmidt, H., Hattel, J., Wert, J., 2004. An analytical model for the heat generation in friction stir welding. Modelling And Simulation In Materials Science And Engineering 12, 143–157.

Schmidt, H.N.B., Dickerson, T.L., Hattel, J.H., 2006. Material flow in butt friction stir welds in {AA}2024-{T}3. Acta Materialia 54, 1199–1209.

Schneider, J., Beshears, R., Jr., A.C.N., 2006. Interfacial sticking and slipping in the friction stir welding process. Materials Science Engineering A 435-436, 297–304.

Seidel, T.U., Reynolds, A.P., 2003. Two-dimensional friction stir welding process model based on fluid mechanics. Science And Technology Of Welding And Joining 8, 175–183.

Shercliff, H.R., Colegrove, P.A., 2002. Modelling of Friction Stir Welding, in: Cerjak, H. (Ed.), Mathematical Modelling of Weld Phenomena 6. Maney, London, UK, pp. 927–974.

Tello, K., 2008. Coupled model of heat transfer and plastic deformation in friction stir welding using scaling analysis. Ph.D. thesis. Colorado School of Mines.

Thomas, W.M., Nicholas, E.D., Needham, J.C., Murch, M.G., Temple-Smith, P., Dawes, C.J., 1991. Friction stir butt welding.

Trimble, D., Monaghan, J., ODonnell, G., 2012. Force generation during friction stir welding of AA2024-T3. CIRP Annals - Manufacturing Technology 61, 9–12.

TWI The Welding Institute, . Materials Joining Technology Home Page. Friction Stir Welding. www.twi.co.uk/j32k/unprotected/band_1/fswmat.html.

Ulysse, P., 2002. Three-dimensional modeling of the friction stir-welding process. International Journal Of Machine Tools & Manufacture 42, 1549–1557.

Xu, S., Deng, X., Reynolds, A.P., Seidel, T.U., 2001. Finite element simulation of material flow in friction stir welding. Science And Technology Of Welding And Joining 6, 191–193.

Yang, B., Yan, J., Sutton, M.A., Reynolds, A.P., 2004. Banded microstructure in AA2024-T351 and AA2524-T351 aluminum friction stir welds Part I. Metallurgical studies. Materials Science and Engineering A364 364, 55–65.

Zhao, Y., Lu, Z., Yan, K., Huang, L., 2015. Microstructural characterizations and mechanical properties in underwater friction stir welding of aluminum and magnesium dissimilar alloys. Materials & Design 65, 675–681.

Zhu, X.K., Chao, Y.J., 2004. Numerical simulation of transient temperature and residual stresses in friction stir welding of 304{L} stainless steel. Journal Of Materials Processing Technology 146, 263–272.

Appendix

FSW Tool Design
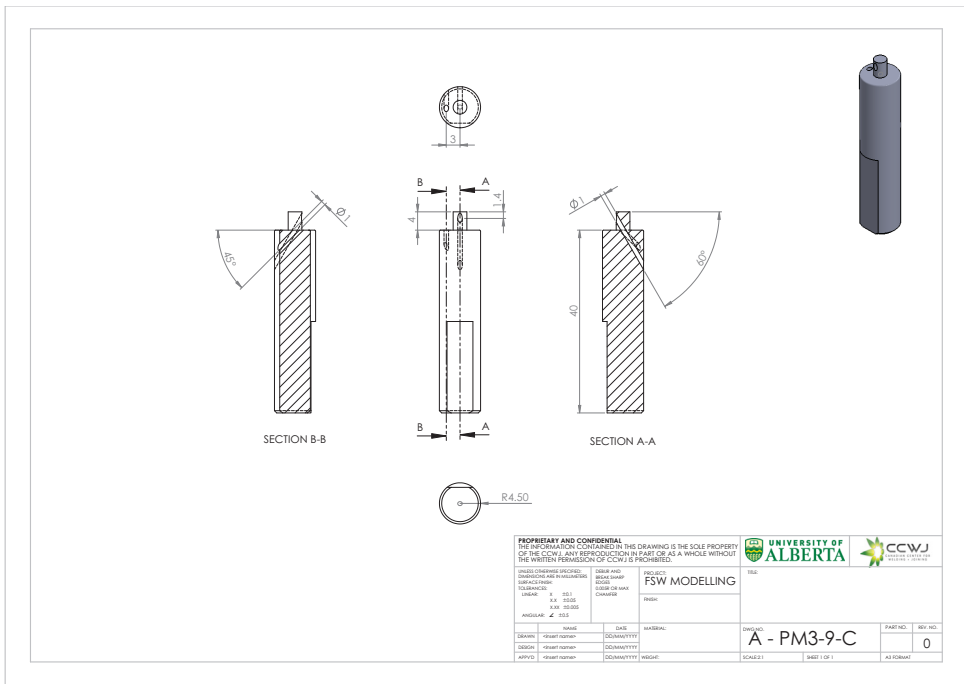
Figure A-1: Tool A engineering drawing
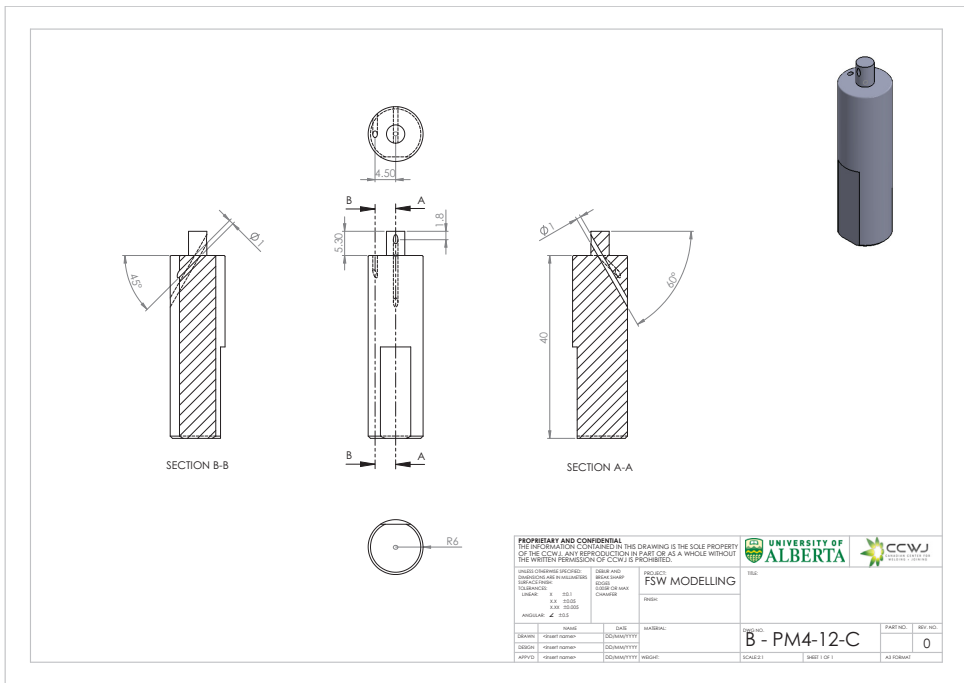
Figure A-2: Tool B engineering drawing
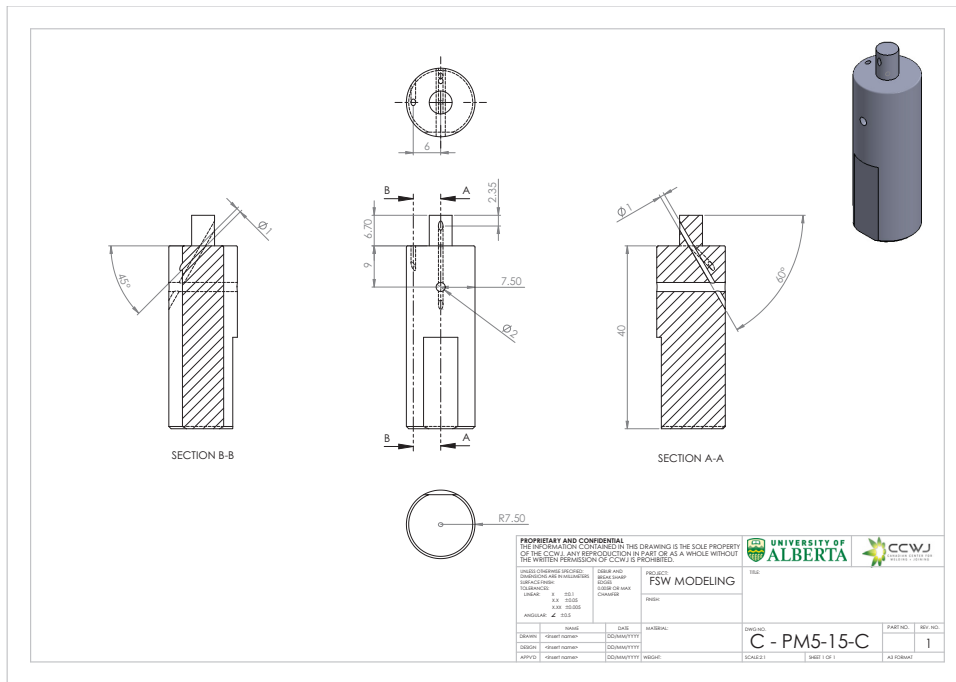
Figure A-3: Tool C engineering drawing
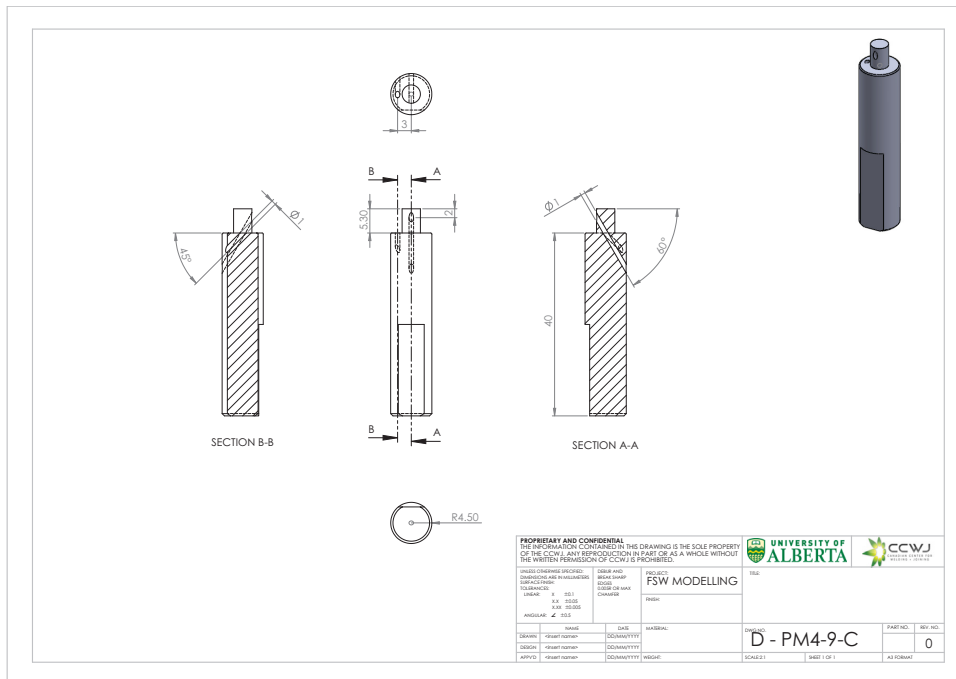
Figure A-4: Tool D engineering drawing
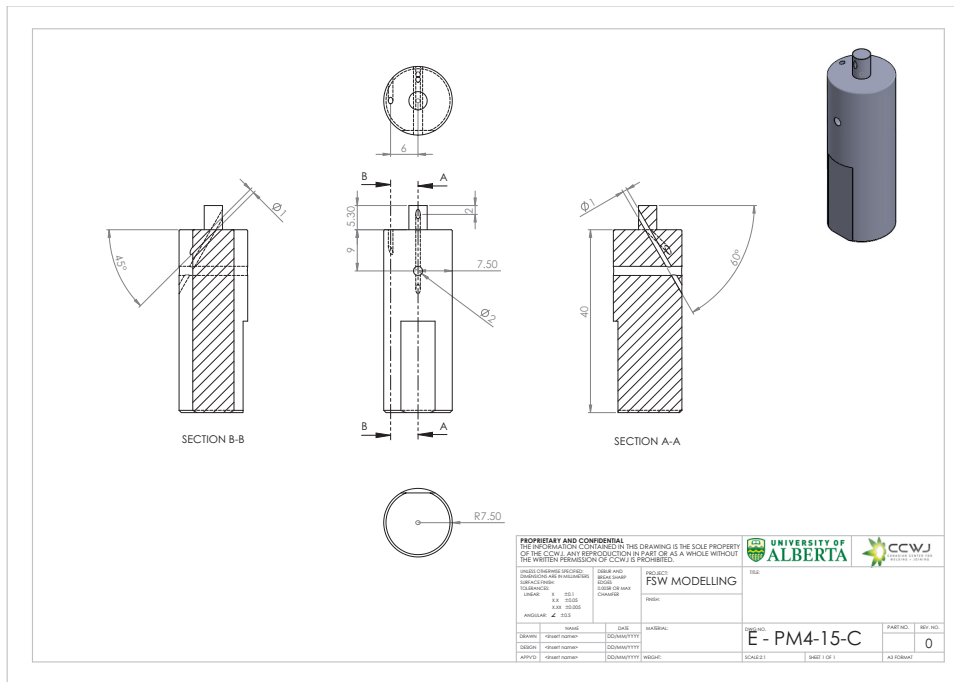
Figure A-5: Tool E engineering drawing
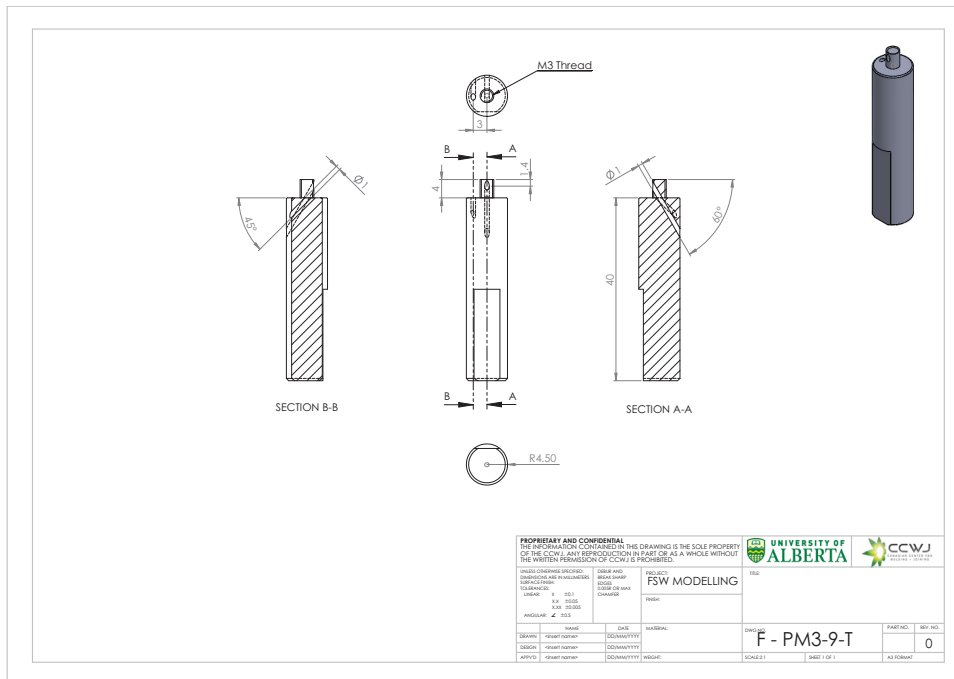
Figure A-6: Tool F engineering drawing
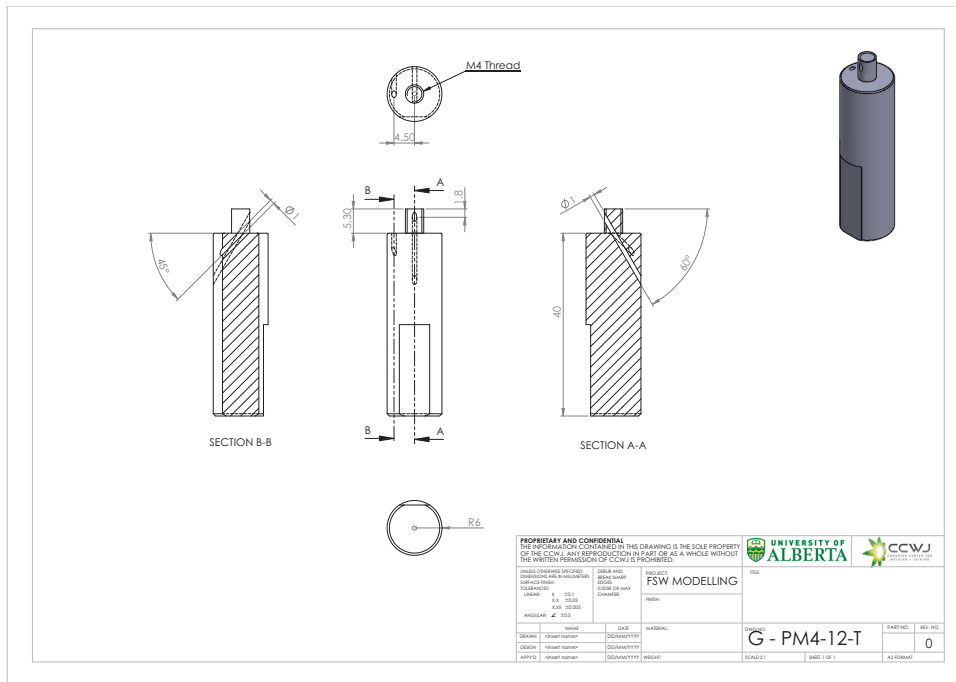
Figure A-7: Tool G engineering drawing
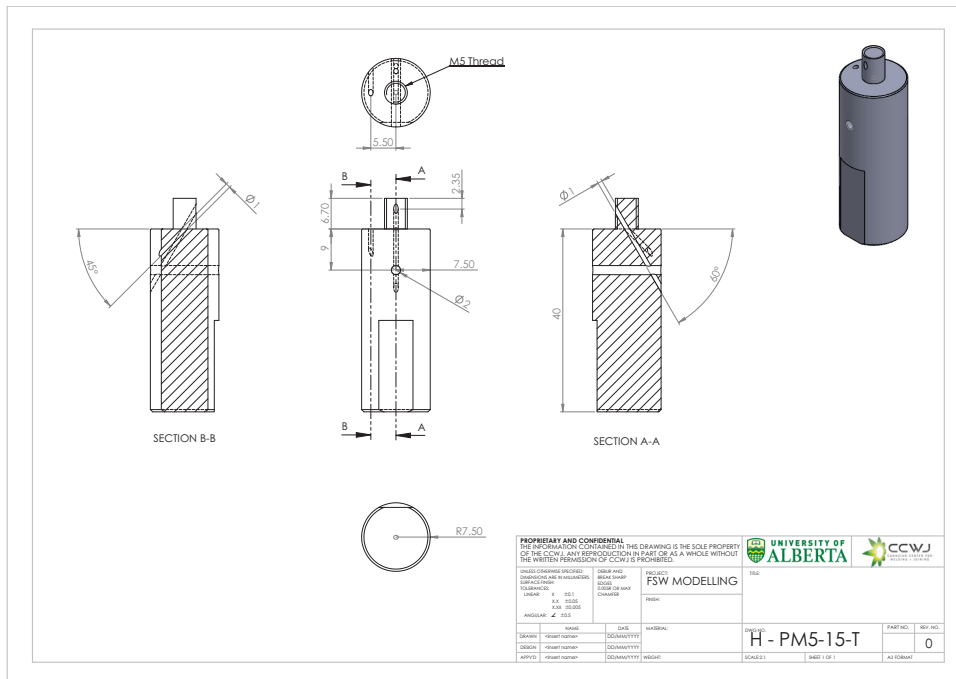
Figure A-8: Tool H engineering drawing
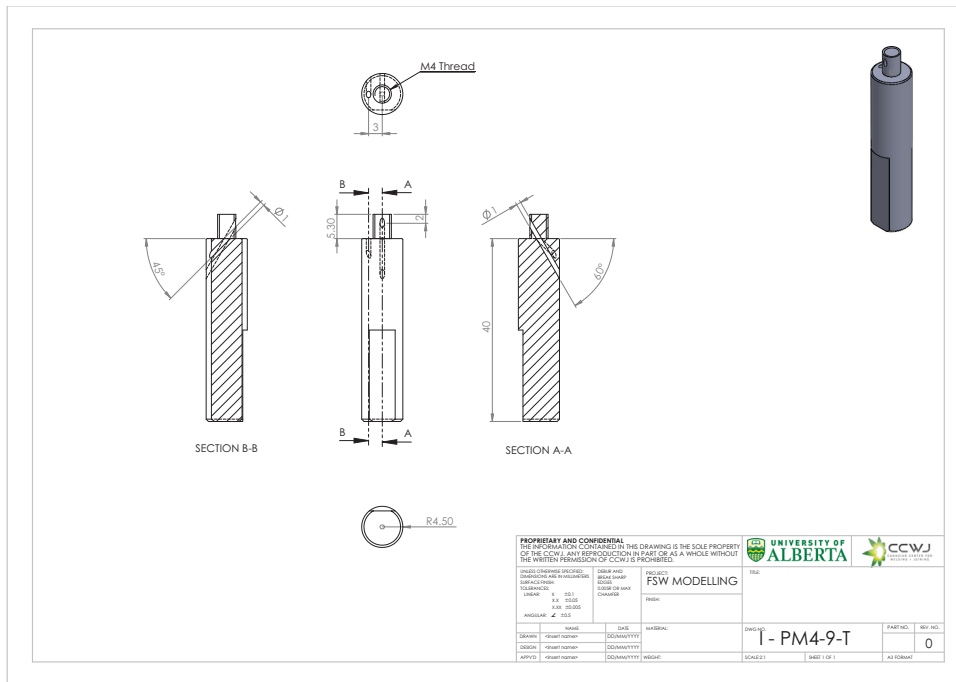
Figure A-9: Tool I engineering drawing
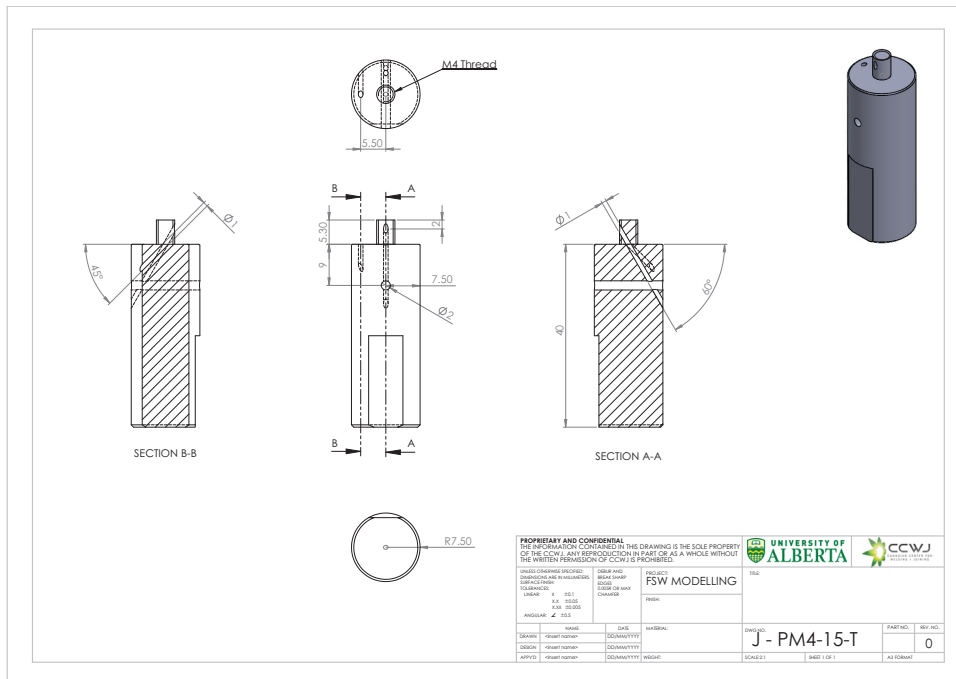
Figure A-10: Tool J engineering drawing

FSW Tool Temperature Calibration data

Table A-1: Temperature calibration curve 1 (tool E)

Furnace Temperature (°C)	Tool Temperature (°C)
97.8	83.5
195.4	174.5
294.1	278.5
397.7	391.5
499.4	504.6

Table A-2: Temperature calibration curve 2 (tool B)

Furnace Temperature (°C)	Tool Temperature (°C)
148.1	147
248.7	241.5
347.4	345.25
473.7	477.75

Table A-3: Temperature calibration curve 3 (tool C)

Furnace Temperature (°C)	Tool Temperature (°C)
97.8	82
195.4	172
294.1	277
397.7	390
499.4	503.7

Table A-4: Temperature calibration curve 4 (tool F)

Furnace Temperature (°C)	Tool Temperature (°C)
147.1	142.5
245.8	240.25
346.4	342
473.7	476.25

Table A-5: Temperature calibration curve 5 (tool I)

Furnace Temperature (°C)	Tool Temperature (°C)
147.1	143
245.8	240.9
346.4	342.75
473.7	476.75

Table A-6: Temperature calibration curve 6 (plate i)

Furnace Temperature (°C)	Substrate Temperature (°C)
148.1	135.5
248.7	228
345.4	328.5
447.6	431.5

Table A-7: Temperature calibration curve 7 (plate ii)

Furnace Temperature (°C)	Substrate Temperature (°C)
148.1	131.5
248.7	219
345.4	324
447.6	428.5

Table A-8: Temperature calibration curve 8 (plate iv)

Furnace Temperature (°C)	Substrate Temperature (°C)
149.1	136.25
247.7	226.25
346.4	328.5
473.7	462.75

Table A-9: Temperature calibration curve 9 (plate v)

Furnace Temperature (°C)	Substrate Temperature (°C)
149.1	130.25
247.7	219
346.4	321.25
473.7	456.5

FSW temperature calculation variables

Table A-10: Variables used to calculate theoretical maximum welding temperature (Equation 2.6) during FSW (1/2)

Tool i.d.	T_m (K)	ΔT_m (K)	T_o (K)	ΔT_o (K)	η (%)	η_s (%)	A (1/s)	B	K_o
A	847	36.44	810.56	512.56	90	100	3.5E+14	8.1E-11	3.23
B	847	36.44	810.56	512.56	90	100	3.5E+14	8.1E-11	3.08
C	847	36.44	810.56	512.56	90	100	3.5E+14	8.1E-11	2.92
D	847	36.44	810.56	512.56	90	100	3.5E+14	8.1E-11	3.08
E	847	36.44	810.56	512.56	90	100	3.5E+14	8.1E-11	3.08
F	847	36.44	810.56	512.56	90	100	3.5E+14	8.1E-11	3.23
G	847	36.44	810.56	512.56	90	100	3.5E+14	8.1E-11	3.08
H	847	36.44	810.56	512.56	90	100	3.5E+14	8.1E-11	2.97
I	847	36.44	810.56	512.56	90	100	3.5E+14	8.1E-11	3.08
J	847	36.44	810.56	512.56	90	100	3.5E+14	8.1E-11	3.08

Table A-11: Variables used to calculate theoretical maximum welding temperature (Equation 2.6) during FSW (2/2)

Tool i.d.	k_o $(Wm^{-1}K^{-1})$	n	τ_r (Pa)	a (m)	w (1/s)	$\frac{\widehat{\delta}}{a}$	$\frac{b-a}{\widehat{\delta}}$
A	146.9	8.41	1.23E+08	0.0015	180.4	0.91	2.20E-06
B	146.9	8.41	1.23E+08	0.002	128.3	1.65	1.21E-06
C	146.9	8.41	1.23E+08	0.0025	128.3	8.44	2.37E-07
D	146.9	8.41	1.23E+08	0.002	128.3	1.65	7.58E-07
E	146.9	8.41	1.23E+08	0.002	128.3	1.65	1.67E-06
F	146.9	8.41	1.23E+08	0.0015	180.4	0.91	2.20E-06
G	146.9	8.41	1.23E+08	0.002	128.3	1.65	1.21E-06
H	146.9	8.41	1.23E+08	0.0025	128.3	9.12	2.19E-07
I	146.9	8.41	1.23E+08	0.002	128.3	1.65	7.58E-07
J	146.9	8.41	1.23E+08	0.002	128.3	1.65	1.67E-06

FSW torque calculation variables

Table A-12: Experimental and predicted temperatures during FSW, Figure 4.5 (1/3)

Authors	T_{max} (°C)	$\widehat{T}^+_{max}$ (°C)
6061 Roy et al. Num (Roy et al., 2006)	469	434
	463	434
	456	434
	518	451
	522	453
	526	456
	547	520
	545	516
	541	510
6061 Roy et al. Exp (Roy et al., 2006)	547	521
	497	456
	500	448
	493	440
	482	445
6061 Nandan et al. Num (Nandan et al., 2006a)	427	434
	421	434
	415	434
	476	451
	483	453
	490	456
	534	520
	528	516
	524	510
6061 Nandan et al. exp (Nandan et al., 2006a)	412	434
	472	450
	517	509
6061 Khandkar et al. Num (Khandkar et al., 2003)	410	436
6061 Khandkar et al. Exp (Khandkar et al., 2003)	392	436
6061 Chen and Kovacevic Num (Chen and Kovacevic, 2003)	380	433
	491	433
6063 Sato et al. Exp (Sato et al., 2002)	399	433
	450	435
	468	441
	500	447
	507	481
	522	557
6061 Assidi et al. Exp (Assidi et al., 2010)	547	433
6061 Assidi et al. Num (Assidi et al., 2010)	524	433
	538	433
2024 Yang et al. Num (Yang et al., 2004)	330	367

Table A-13: Experimental and predicted temperatures during FSW, Figure 4.5 (2/3)

Authors	T_{max} (°C)	$\widehat{T}^+_{max}$ (°C)
2024 Schmidt et al. 2004 Exp (Schmidt et al., 2004)	400	367
2024 Schmidt and Hattel 2005 Num (Schmidt and Hattel, 2005a)	426	367
2024 Schmidt and Hattel 2005 Num (Schmidt and Hattel, 2005b)	510	367
5083 Colligan Exp (Colligan, 2007)	574	568
	530	465
	545	534
	575	584
5083 Kim at el. Num (Kim et al., 2010)	527	427
	473	425
	551	453
7050 Reynold et al. 2003 Num (Reynolds et al., 2003)	233	346
	316	346
	365	359
	390	364
7050 Reynold et al. 2005 Num (Reynolds et al., 2005)	319	346
	398	348
	388	369
	430	442
7136 Hamilton et al. Num (Hamilton et al., 2008)	314	346
	413	347
2195 Chao et al. Exp (Chao et al., 2003)	399	474
	418	468
AZ61 Razal Rose et al. Exp (Rose et al., 2012)	436	445
	447	445
	472	445
	469	445
	460	445
304 Roy et al. Num 2006 (Roy et al., 2006)	1139	1117
	1245	1119
	1043	1117
	1112	1117
	1040	1117
	968	1116
	927	1116
	983	1116
	1041	1117
304 Roy et al. Exp 2006 (Roy et al., 2006)	1157	1116
304 Zhu et al. Num (Zhu and Chao, 2004)	970	1116

Table A-14: Experimental and predicted temperatures during FSW, Figure 4.5 (3/3)

Authors	T_{max} (°C)	$\widehat{T}^+_{max}$ (°C)
1018 Roy et al. 2006 Num (Roy et al., 2006)	1155	1167
	1233	1177
	1076	1161
	1013	1159
	963	1158
	1086	1163
	1028	1160
	1150	1169
	1088	1164
1018 Roy et al. 2006 Exp (Roy et al., 2006)	1000	1161
1018 Nandan et al. 2006 Num (Nandan et al., 2007)	1190	1161
Ti64 Lienert et al. Exp (Lienert, 2007)	870	1194
5059 Tsui Exp	395	458
	445	480
	489	499
	435	480
	488	480
	422	458
	454	480
	458	493
	439	480
	475	480

Table A-15: Variables used to calculate theoretical torque during FSW (Equation 2.7)

Tool i.d.	τ_c (Pa)	a (m)	t (m)
A	6.39E+07	0.0015	0.0040
B	5.30E+07	0.0020	0.0053
C	3.57E+07	0.0025	0.0067
D	5.30E+07	0.0020	0.0053
E	5.30E+07	0.0020	0.0053
F	6.39E+07	0.0015	0.0040
G	5.30E+07	0.0020	0.0053
H	3.51E+07	0.0025	0.0067
I	5.30E+07	0.0020	0.0053
J	5.30E+07	0.0020	0.0053

Material properties and constants

Table A-16: Experimental and predicted torque during FSW, Figure 4.9 (1/2)

Authors	$M_{experimental}$ (N-m)	$\widehat{M}^{+}$ (N-m)
6061 Khandkar et al. Exp (Khandkar et al., 2003)	84.4	84.9
6061 Lienert et al. (Lienert et al., 2000)	30.6	24.9
2024 Yang et al. Num (Yang et al., 2004)	95.5	84.3
2024 Schmidt et al. 2004 Exp (Schmidt et al., 2004)	40.0	22.1
7075 Lienert et al. (Lienert et al., 2000)	58.6	45.6
5083 Colligan Exp (Colligan, 2007)	369.0	400.2
	300.0	319.1
	320.0	358.0
	334.0	400.2
5083 Long et al. (Long et al., 2007)	181.0	222.4
	152.0	167.9
	128.0	135.5
	108.0	111.8
	94.0	94.1
	79.0	75.6
	70.0	66.0
	64.0	56.2
	50.0	45.9
	40.0	38.9
	35.0	33.8
7050 Reynold et al. 2003 Num (Reynolds et al., 2003)	108.2	107.5
	100.1	106.4
	86.5	91.4
	116.3	106.8
	103.9	91.3
	78.8	88.1
	74.8	65.4
	78.3	65.6
	61.2	57.7
	64.0	68.1
	73.5	86.5
	66.7	57.7
	56.5	47.3
	52.5	47.6
	61.7	47.3
	52.3	43.8
	41.9	34.2
	35.9	27.9

Table A-17: Experimental and predicted torque during FSW, Figure 4.9 (2/2)

Authors	$M_{experimental}$ (N-m)	$\widehat{M}^+$ (N-m)
7050 Long et al. (Long et al., 2007)	305.0	308.6
	273.0	287.5
	129.0	143.4
	95.0	115.6
	76.0	102.2
	68.0	87.8
	60.0	63.9
	57.0	49.7
	54.0	46.4
7136 Hamilton et al. Num (Hamilton et al., 2008)	82.5	65.0
	58.9	46.6
5059 Tsui Exp	6.7	4.8
	6.0	9.4
	10.0	12.6
	10.3	9.4
	8.0	9.4
	3.2	4.8
	5.7	9.4
	12.4	12.4
	6.7	9.4
	7.4	9.4

Table A-18: Material properties of aluminum (Tello, 2008)

		Al2024	Al2195	Al5083	Al6061	Al7050	Al7075
T_m	(°C)	502	540	574	582	488	532
	(°K)	775	813	847	855	761	805
T_∞	(°C)	25	25	25	25	25	25
	(°K)	298	298	298	298	298	298
τ_y	(Pa)	5.97E+07	4.00E+08	1.23E+08	3.18E+07	2.63E+08	5.97E+07
A	$(1/s)$	6.52E+14	2.37E+13	3.5E+14	1.72E+13	2.88E+19	2.05E+09
n		11.47	3.54	8.41	7.68	13.20	12.85
Q	(J/mol)	178176.4	161777.2	163672.4	191289.7	122698.0	123126.9
T_o	(°K)	747.0	779.0	810.6	823.2	721.8	761.2
ΔT_o	(°K)	449.0	481.0	512.6	525.2	423.8	463.2
ΔT_m	(°K)	28.0	34.0	36.4	31.8	39.2	43.8
η		0.9	0.9	0.9	0.9	0.9	0.9
η_s		1	1	1	1	1	1
k	$(Wm^{-1}K^{-1})$	185.0	196.0	146.9	200.0	180.0	192.0
C_p	$(Jkg^{-1}K^{-1})$	1100.0	1338.0	1261.4	1160.0	861.0	1109.0
r	(kg/m^3)	2670.0	2770.0	2552.8	2590.0	2827.0	2693.0
α	(m^2/s)	6.30E-05	5.29E-05	4.56E-05	6.66E-05	7.40E-05	6.43E-05
B		9.78E-13	4.03E-11	8.05E-11	2.06E-12	3.78E-09	1.02E-08

Table A-19: Material properties of non-aluminum (Tello, 2008)

		AISI 1080	AISI 304	Ti-6Al-4V	AZ31	AZ61
T_m	(°C)	1460	1400	1604	566	610
	(°K)	1733	1673	1877	839	883
T_∞	(°C)	25	25	25	25	25
	(°K)	298	298	298	298	298
τ_y	(Pa)	1.18E+08	1.67E+08	5.05E+08	1.5E+08	2.17E+08
A	$(1/s)$	6.95E+16	6.37E+18	4.18E+13	6.26E+12	1.82E+13
n		5.67	5.89	5.36	7.57	9.00
Q	(J/mol)	371349.5	441226.7	175844.0	129407.4	143090.9
T_o	(°K)	1665.8	1620.3	1710.4	793.8	837.7
ΔT_o	(°K)	1367.8	1322.3	1412.4	495.8	539.7
ΔT_m	(°K)	67.2	52.7	166.6	45.2	45.3
η		0.75	0.5	0.47	0.9	0.9
η_s		1	1	1	1	1
k	$(Wm^{-1}K^{-1})$	33.1	33.5	27.0	114.3	80.0
C_p	$(Jkg^{-1}K^{-1})$	699.0	720.0	750.0	1446.3	1050.0
r	(kg/m^3)	7314.0	7350.0	4198.0	1696.2	1800.0
α	(m^2/s)	6.48E-06	6.33E-06	8.58E-06	4.66E-05	4.23E-05
B		6.41E-12	1.67E-14	1.28E-05	8.77E-09	3.43E-09